SPENT NUCLEAR FUEL SELF-INDUCED XRF TO PREDICT PU TO U CONTENT

A Thesis

by

ALISSA SARAH STAFFORD

Submitted to the Office of Graduate Studies of
Texas A&M University
in partial fulfillment of the requirements for the degree of

MASTER OF SCIENCE

August 2010

Major Subject: Nuclear Engineering

SPENT NUCLEAR FUEL SELF-INDUCED XRF TO PREDICT PU TO U CONTENT

A Thesis

by

ALISSA SARAH STAFFORD

Submitted to the Office of Graduate Studies of
Texas A&M University
in partial fulfillment of the requirements for the degree of

MASTER OF SCIENCE

Approved by:

Chair of Committee,	William Charlton
Committee Members,	Sean McDeavitt
	Sara Daly
Head of Department,	Raymond Juazitis

August 2010

Major Subject: Nuclear Engineering

ABSTRACT

Spent Nuclear Fuel Self-Induced XRF to Predict Pu to U Content. (August 2010)

Alissa Sarah Stafford, B.S., Texas A&M University

Chair of Advisory Committee: Dr. William Charlton

The quantification of plutonium (Pu) in spent nuclear fuel is an increasingly important safeguards issue. There exists an estimated worldwide 980 metric tons of Pu in the nuclear fuel cycle and the majority is in spent nuclear fuel waiting for long term storage or fuel reprocessing. This study investigates utilizing the measurement of x-ray fluorescence (XRF) from the spent fuel for the quantification of its uranium (U) to Pu ratio. Pu quantification measurements at the front end of the reprocessing plant, the fuel cycle area of interest, would improve input accountability and shipper/receiver differences.

XRF measurements were made on individual PWR fuel rods with varying fuel ages and final burn-ups at Oak Ridge National Laboratory (ORNL) in July 2008 and January 2009. These measurements successfully showed that it is possible to measure the Pu x-ray peak at 103.7 keV in PWR spent fuel (~1% Pu) using a planar HPGe detector. Prior to these measurement campaigns, the Pu peak has only been measured for fast breeder reactor fuel (~40% Pu). To understand the physics of the measurements, several modern physics simulations were conducted to determine the fuel isotopics, the sources of XRF in the spent fuel, and the sources of Compton continuum. Fuel transformation and decay

simulations demonstrated the Pu/U measured peak ratio is directly proportional to the Pu/U content and increases linearly as burn-up increases. Spent fuel source simulations showed for 4 to 13 year old PWR fuel with burn-up ranges from 50 to 67 GWd/MTU, initial photon sources and resulting Compton and XRF interactions adequately model the spent fuel measured spectrum and background. The detector simulations also showed the contributions to the Compton continuum from strongest to weakest are as follows: the fuel, the shipping tube, the cladding, the detector can, the detector crystal and the collimator end. The detector simulations showed the relationship between the Pu/U peak ratio and fuel burn-up over predict the measured Pu/U peak but the trend is the same. In conclusion, the spent fuel simulations using modern radiation transport physics codes can model the actual spent fuel measurements but need to be benchmarked.

DEDICATION

I dedicate this thesis to my parents, for all their love and encouragement during my scholastic career. They have taught me the values of integrity, exploration, and ethics, and have encouraged my scientific curiosity from a young age. From their positive influence, I have become the person I want to be and have chosen a fulfilling education.

ACKNOWLEDGEMENTS

I would like to thank my committee chair, Dr. William Charlton, and my committee members, Dr. Sean McDeavitt and Prof. Sara Daly, for their guidance and support throughout the course of this research. I would also like to thank Dr. Andrew Hoover, Steve Saavedra, Cliff Rudy, Dr. Steve Tobin, Daniel Strohmeyer and Jessica Feener for their aid in the spent fuel measurement campaigns.

Thanks also go to Julia White for her work on the North Anna detector system geometry modeling, preliminary simulations and help in creating the photon source inputs for MCNP5 simulations. I would also like to thank Dr. Sunil Chirayath for his expertise in Monte Carlo simulations and helping me use MCNP5/MCNPX for my spent fuel simulations.

Finally, thanks to my friends and colleagues and the department faculty and staff for making my time at Texas A&M University a great experience. I also want to extend my gratitude to Oak Ridge National Laboratory and Los Alamos National Laboratory, which were collaborators in the spent fuel measurements.

NOMENCLATURE

ADEPT	Advanced Diagnostics and Evaluation Platform
BWR	Boiling Water Reactor
CETE	Coupled-End-To-End
DOE	Department of Energy
FP	Fission Products
FWHM	Full-Width-Half-Maximum
Ge	Germanium
Ge (Li)	Germanium-Lithium
HPGe	High-Purity Germanium
IDMS	Isotopic Dilution Mass Spectrometry
IAEA	International Atomic Energy Agency
IAT	Input Accountability Tank
LANL	Los Alamos National Laboratory
LEGe	Low Energy Germanium Detector
LWR	Light Water Reactor
MC&A	Material Control and Accountability
MCNP	Monte Carlo N–Particle
NDA	Nondestructive Assay
NRC	Nuclear Regulatory Committee
NRF	Nuclear Resonance Fluorescence

ORNL	Oak Ridge National Laboratory
Pu	Plutonium
PUREX	Plutonium and Uranium Recovery by Extraction
PWR	Pressurized Water Reactor
RPP	Reprocessing Plant
SNM	Special Nuclear Material
TAMU	Texas A&M University
TMI	Three Mile Island Unit 1
U	Uranium
W	Tungsten
XRF	X-Ray Fluorescence

TABLE OF CONTENTS

Page

Page

LIST OF FIGURES

Page

Page

Page

Page

LIST OF TABLES

Page

1. INTRODUCTION

The ability to accurately measure the quantity of plutonium (Pu) in spent nuclear fuel would improve material control and accountability (MC&A) capabilities at reprocessing facilities, in particular improving shipper/receiver differences and Pu input accountability at the front end of the reprocessing cycle. The front end refers to the beginning of the reprocessing cycle, which is the back end of the fuel cycle. One means of directly measuring the Pu content of spent fuel is the measurement of x-ray fluorescence (XRF) from the spent fuel. XRF is a nondestructive assay technique that passively measures the self-induced XRF from uranium (U) and Pu. Detection of XRF from spent nuclear fuel is possible because this radiation occurs at lower energies compared to the actinide and fission product gamma emissions.

The research presented in this thesis demonstrates the ability to measure XRF from spent nuclear fuel and how XRF can be used as a quantitative measure of bulk Pu content. The following sections provide a background for understanding previous XRF experiments, how XRF works, why verification of spent nuclear fuel is important, and what are the modern radiation transport codes used for analysis. Section 2 describes the North Anna and TMI spent fuel measurement campaigns and the gamma spectrum results. Section 3 describes the spent fuel measurement data analysis; this includes determining fuel burn-up, 2D fuel pin simulations, and correlating Pu/U photopeak ratios to Pu/U content. Section 4 describes the Monte Carlo simulations of the detector system

---

This thesis follows the style of *Nuclear Science and Engineering.*

for understanding the sources of the Compton continuum and the spectrum. Section 5 provides conclusions of this research and recommendations for the continuing XRF research.

1.1 Objective

The objective of this research is to demonstrate that XRF of the U and Pu in solid spent nuclear fuel can be used as a quantitative measure of bulk Pu content. Demonstrating this principle will require precise measurements of spectra from solid spent fuel rods and detailed simulations to understand the relationship between the measured spectra and the bulk Pu content in the spent nuclear fuel. Measurements were performed on North Anna and Three Mile Island Unit 1 (TMI) fuel rod segments at the Coupled-End-To-End (CETE) demonstration facility at Oak Ridge National Laboratory (ORNL). These measurements were simulated using Monte Carlo to replicate the XRF spectra and used modern lattice physics codes to determine isotopic inventory of the spent nuclear fuel. These simulations demonstrate modern physics code capabilities when using operator-declared power history data and provide a starting point for future XRF detector system optimization using computer simulations.

1.2 Previous Work

Previous work on verification of operator declared data including burn-up, cooling times, and Pu and U content are described in the following sections. This collection of previous work only describes a few passive methods using gamma spectroscopy for verification of spent nuclear fuel. First the investigation of XRF for determining Pu content in a fuel element by A.V. Bushuev et al is presented, followed by a method

determining Pu content of spent nuclear fuel assemblies using XRF by C. Rudy et al.. These methods were some of the first examples of the uses of XRF for verification of spent nuclear fuel. Next the Fork detector, originally patented in 1985, is presented. The Fork detector and its advancements currently provide verification of some parameters of operator declared data for spent nuclear fuel. Then the work of C. Willman et al. on nondestructive assay of spent nuclear fuel with gamma spectroscopy is presented to explain how fission product measurements can be used for verification of burn-up and cooling times. Finally the work of S. Tobin et al. on the idea of integration of several verification methods is presented to explain how XRF measurements could possibly be integrated into a multi-measurement method system.

1.2.1 Determining Pu to U Content for Fast Reactor Fuel Elements Using X-Ray Fluorescence - Bushuev

Bushuev was one of the first to suggest using Pu and U XRF measurements to determine the U to Pu content ratio. In Bushuev's paper the Pu to U ratio in fast reactor spent fuel elements are considered through the investigation of x-ray radiation excited by fission product radiation[1]. From previous analysis, he concluded that the K-shell x-ray lines from U and Pu were the most valuable, and a detector to measure this XRF would need an energy resolution of 600–700 eV or better. He proposed using a Ge (Li) detector for measurements[1].

Spent fuel gamma spectroscopy measurements were performed by placing the fuel elements on an apparatus which moved the fuel across the detector field of view using an automated system. A Ge (Li) detector was used for measurements and only the 90-140 keV energy range was considered[2]. The fuel prior to exposure was a uranium dioxide

fuel with a stainless steel cladding. The measurements performed established that the characteristic x-rays lines from Pu and U were distinguishable from the total gamma-ray spectrum[1].

His proposed method was tested by measuring several fast reactor fuel elements, obtaining the Pu to U ratios, and averaging over the height of the fuel elements. The results were then compared to gravimetric measurements. Bushuev concluded a procedure for the non-destructive determination of Pu in fast reactor spent fuel elements had been developed and tested.

Bushuev also concluded there are several factors that could affect the measurement results, mainly the non-uniform radial distribution of Pu and U along the fuel element and the different absorption coefficients of the K-shell x-ray for U and Pu and thus the detection efficiencies. In the fast reactor, the U and Pu radial distributions would be the same due to the low effective cross section of the U-238 n-gamma reaction[1]. This is not the case for thermal reactor spent fuel; therefore, the gravimetric measurements would not reflect the Pu to U ratio measured results. Also, for LWR fuel the Pu content is ~1% whereas for fast reactor fuel the Pu content may be 40%.

Bushuev's work showed that distinguishing Pu x-rays in the spent fuel gamma spectrum is possible using a Ge detector. His work also brought to attention the need to understand the radial and axial distribution of U and Pu inside the spent fuel rod.

1.2.2 Spent Fuel Assembly Pu Content Estimation Using X-Ray Fluorescence – Rudy

In 1998 during a spent fuel verification campaign for the BN-350 fast breeder reactor an XRF Pu signature radiation was observed for verification of the Pu content[2]. In order

to verify the Pu content of the fast breeder spent fuel, a series of gamma-ray measurements were conducted on the spent fuel assemblies in an air-filled hot cell using a 25% efficient coaxial high-purity germanium (HPGe) detector[2]. The spent fuel samples had experienced cooling times from five to ten years[2]. Figure 1 (from Reference 2) shows an expanded view of the K-shell x-ray region in the measured gamma-ray spectrum for a 120 second live time count[2]. The Pu $K_{\alpha 1}$ at 103.734 keV and Eu-155 at 105.312 keV are between the U K_{α} and K_{β} peaks[2].

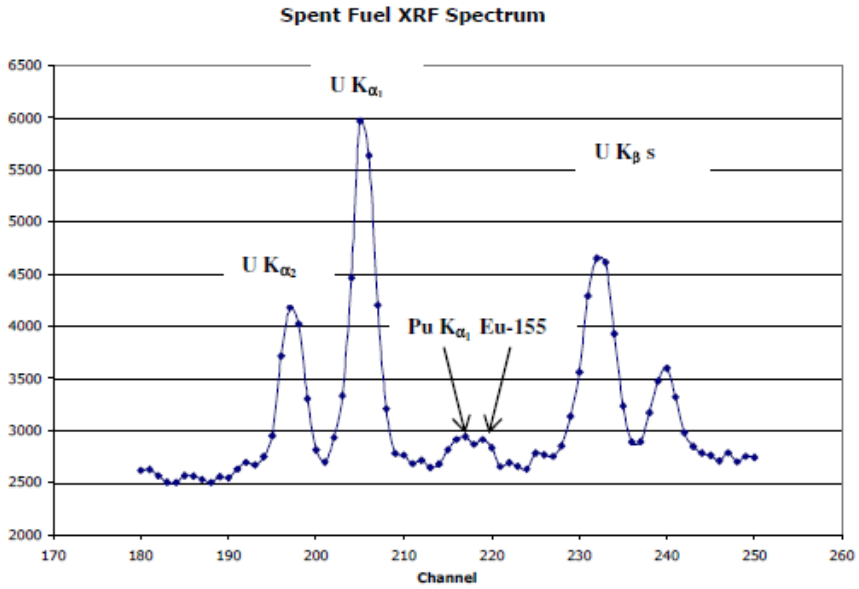

Figure 1. BN-350 fast breeder reactor fuel gamma-ray spectrum focusing on XRF region, figure from Reference 2

Rudy's gamma measurement analysis considered the relationship between the Pu x-ray flux and the U x-ray flux emitted from the assembly to correlate to the U/Pu mass ratio. The flux ratio was approximated using the ratio of the appropriate measured peaks

x-ray peaks and multiplying by the relative efficiency[2]. The relative efficiency was calculated using peak areas of the five U K-shell x-rays. This approximation had many assumptions including that the Pu spatial distribution follows the U distribution, the attenuation of the Pu $K_{\alpha 1}$ x-ray is identical to a U x-ray at the same energy, and the Pu and U are excited identically by the radiation flux[2].

The undesirable features of this method are that in a thermal reactor spent fuel assembly the U and Pu spatial distributions are very different and the creation of U and Pu x-rays are different for the same excitation radiation. Rudy states the relative excitation probabilities for stimulating U and Pu x-rays by fission product activity must also be determined to correlate the flux ratios to mass ratios. Rudy concludes that the fast breeder spent fuel measurements showed the fluorescent U and Pu x-rays from spent fuel assemblies are observable.

1.2.3 Fork Detector

The purpose of the fork detector is to safeguard spent fuel assemblies through passive measurement of neutron and gamma radiation. For example the fork detector can be used for verification of fuel irradiation history, cooling times, detecting partial defects, and much more. The fork detector cannot measure the U and Pu content of spent fuel assemblies directly, because the fission product gamma-rays make it impossible to detect gamma-rays from fuel isotopes, and the neutrons are dominated by transuranic isotopes (specifically, Cm-242 and Cm-244). One capability of the fork detector is to verify that the spent fuel assemblies have not been modified and they are actual spent fuel assemblies[3]. In 1988 the fork detector consisted of a u-shaped piece of polyethylene

with two fission chambers and one ionization chamber embedded in each arm[3]. Polyethylene is used to slow down the incoming neutrons to increase the probability of interaction in the detector. The fork detector detected total neutrons and gamma-rays[3]. Figure 2 provides a schematic of the fork detector wrapped around a 15 by 15 spent fuel assembly for measurements and a cross sectional view of one arm[4].

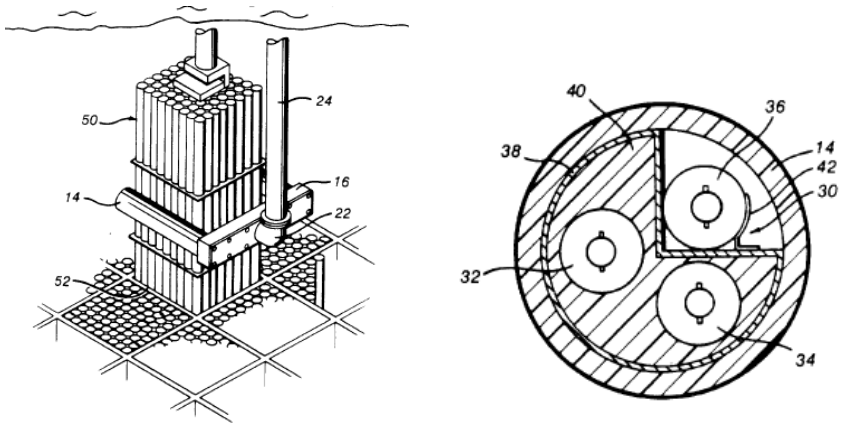

Figure 2. Fork detector and spent fuel assembly[4]

One fission chamber is cadmium wrapped measure epithermal and fast neutrons, and the other fission chamber is left bare to measure the entire neutron spectrum[3]. This detector system enables one to determine the boron content in the spent fuel storage pool. The original design was used to verify fuel burn-up declarations[5].

By 1996 a fork detector technique was developed to use the gamma/neutron ratios to verify the number of irradiation cycles of the fuel assemblies[5], and the fork detector was modified to withstand intense gamma-rays to be able to measure freshly discharged fuel. It is able to measure assemblies from a few days to several years after discharge[5]. This modification also allows for verification measurements during reloading and

maintenance periods[5]. By 2001 the gamma/neutron ratio method to independently verify the number of fuel cycles was successfully tested by measuring PWR, BWR, WWER-440, and WWER-1000 fuel assemblies[6]. The fork detector also has the ability to detect a diversion of 50% of the fuel pins missing from an assembly, but this proves to be an ineffective tool for partial defect detection[7].

The fork detector revolutionized the measurement of spent fuel assemblies by being able to operate underwater in the cooling pool. It has proven to be a good tool for burn-up declaration verification and irradiation history.

1.2.4 Gamma-ray Detection for Verification of Operator-declared Information – Willman

Willman proposed the use of gamma emitting fission product isotopes, Cs-134, Cs-137 and Eu-154, to verify the reactor operator declared information[8,9,10]. As previously mentioned the fork detector can provide spent fuel burn-up verification and cooling times; however, the same discharge burn-up results can be achieved through various irradiation histories. In this research, Willman specifically investigated the extent to which irradiation histories can be verified.

Willman's gamma spectroscopy verification technique is based on a functional relationship involving the gamma-ray intensity, the cooling time, and the isotopic content of the fuel at discharge which depends on various parameters[8,9,10]. This relationship is given by

$$i_x e^{\lambda_x T} = F_x \quad (1)$$

where i_x is the measured gamma-ray intensity, λ_x is the decay constant of isotope x, T is the cooling time, and F_x is a function of the isotopic content[8]. Using this basic theory,

F_x can be approximated by the calculated isotopic content of the fuel at discharge and an experimental calibration constant[8], given by

$$i_x e^{\lambda_x T} = K_x I_x \quad (2)$$

where K_x is the experimental calibration constant and I_x is the calculated isotopic content for isotope x[8]. K_x is a constant and can be determined by linearly fitting to the experimental intensities, corrected cooling time, and calculated isotopic content for several fuel assemblies[8]; this action can be accomplished by measuring well-known fuel assemblies. Once K_x is established using reference assemblies, these relationships can be used for measuring other assemblies of the same type[8]. K_x depends on the detector and collimator system and the fuel assembly geometry[8]; therefore, a change in any of these properties will result in a new K_x calculation. For this study, Willman considered gamma-rays from Cs-134, Cs-137 and Eu-154 nuclides for measurement and simulations[8,9].

This verification technique was tested by performing simulations and experimental measurements for different informational scenarios such as non-declared rod removal before cycle end and erroneously declared number of cycles[8]. The calibration constant K_x was also determined from the measurements. A spent nuclear fuel code, SNF, simulated the fuel isotopic content. Fuel assembly simulations were conducted with and without irradiation history knowledge to test the method limits. Origen-ARP was also used to investigate the gamma-ray intensities[8]. For the measurements, gamma-ray spectra were taken from 12 PWR assemblies with cooling times of approximately 10 years[8]. Figure 3 displays the typical spent fuel assembly spectrum with a burn-up of 47

GWd/MTU and 12 years cooling time, from Reference 8. The Cs-134, Cs-134, and Eu-154 peaks of interest are clearly visible.

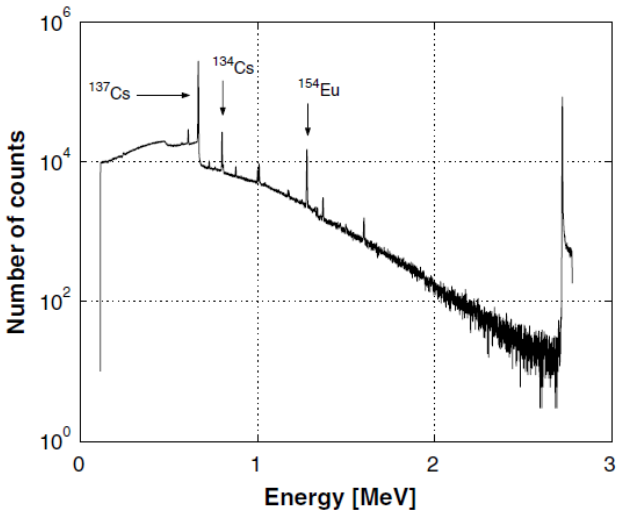

Figure 3. Spent fuel assembly gamma-ray spectrum from Reference 8

In the feasibility study, it was concluded the Cs-134 intensities and content can be used to reveal erroneous declarations of irradiation history[8]. This technique is sensitive to incorrectly declared cooling times with a 1-σ uncertainty of 27 days[8]. In the case where no operator declared information is available, the burn-up and cooling times can be determined using Cs-137 and Cs-134 intensities with relative uncertainties of 1.6% and 1.5%, and they can also be determined using Cs-137 and Eu-154 intensities with relative uncertainties of 4.6% and 15.5%[8]. This technique provides a strong tool for spent fuel information verification that implements passive gamma spectroscopy at high energies. For more information on this technique including theory, experimental apparatus, and results, refer to "Nondestructive Assay of Spent Nuclear Fuel with Gamma-Ray Spectroscopy" by C. Willman.

1.2.5 Integrated NDA Approach for Determination of Pu Content – Tobin

The application of nondestructive assay (NDA) methods has shown promise for determining the Pu content in spent nuclear fuel assemblies. Few NDA methods directly measure elemental Pu [e.g. XRF and nuclear resonance fluorescence (NRF)], and these methods have many weaknesses. Tobin's research suggests combining multiple NDA methods to create an integrated measurement system, playing to different method strengths. His research addresses the 11 NDA techniques being considered for integration, the motivations, and the discussion of combining these techniques.

This thesis discusses the measurement methods involving gamma-rays and the uses of XRF. The NDA methods described are delayed gammas, NRF, passive gamma-rays, and XRF. In the delayed gamma method, spent fuel is interrogated by a neutron source or bremsstrahlung source to induce fission[11]. The resulting fission fragments emit delayed gamma-rays (seconds after induced fission) that are measured using a high resolution detector. If enough delayed gamma-rays were successfully detected, one would be able to determine the relative abundance of Pu-239, Pu-241 and U-235[11]. The relative abundance can then be translated to Pu mass by knowing the fissile content. This method works because these nuclides have unique fission fragment distributions. At this point in time, delayed gammas have not been measured from spent fuel. A weakness of this method implementation would be that gamma-ray shielding by fuel rods will prevent the interrogation source from reaching interior fuel assembly rods[11].

NRF uses a strong active photon interrogation source on the spent nuclear fuel which causes nuclei excitation. These excited nuclei then emit a characteristic gamma-ray for

which the intensity is proportional to the isotope's amount in the fuel. These gamma-rays are measured and provide the relative abundance of the isotopes of the actinides in the spent fuel[11]. This technique has the ability to directly measure Pu content, but little research has been conducted on NRF. The weaknesses of this method are that (1) the incident gamma-ray source will be severely attenuated at the interior of the assembly, and (2) the high gamma-ray background will lead to a low signal-to-noise ratio due to both fission product decay gammas and the interrogation gamma-rays. This method could possibly aid other NDA methods by determining elemental Pu content without the need of burn-up simulations[11].

The passive gamma-ray method involves the measurement of passive gamma-rays from fission products in the fuel and cladding; these include Cs, Rh, Zr, Nb, Co, Eu, and Pr[11]. This method can help verify burn-up and/or cooling times for the spent nuclear fuel[11]. For determination of Pu content, this method may be used to quantify the relative Pu-239 fissions to U-235 fissions with the measured Cs-137 and Eu-154 gamma lines. This method relies on the fact that three times more Eu-154 is produced with Pu-239 as the fissioning isotope than with U-235[11]. It is suggested that the total neutron counts should be used as a burn-up indicator and then combined with the passive gamma method for determination of cooling times[11].

The XRF method measures the x-rays from elemental U and Pu in spent nuclear fuel passively. The low energy x-rays are stimulated by gamma-ray emissions from the fission products, actinides and minor actinides in the fuel such as Cs-137 and Eu-154. Due to self attenuation in the fuel only x-rays from the outer layer (~300 μm) of the

spent fuel is measured[11]. It is possible that x-rays from the outer edge of several rods in an assembly could be measured to determine the Pu/U ratio of those outer rods. If the axial and radial profiles of Pu and U in the rods are known, the measurement ratio can be translated to Pu/U bulk content ratio. The U mass in the spent fuel is easily determined with low uncertainty and can be multiplied by the Pu/U content ratio to obtain the Pu mass[11]. The weakness of this method is that the x-ray signal may be too low to overcome the fission product gamma background, and it cannot detect the diversion of an interior rod. In regards to fuel assemblies, this method may be able to supply the Pu/U ratio on the assembly edge rods that could be used for another NDA method[11]. Tobin's publication suggests XRF be combined with techniques measuring fissile content such as delayed neutron, coincidence counting, differential die-away, and passive neutron albedo reactivity. For more information on these NDA methods refer to Reference 11.

For this thesis, the XRF method is used to measure single spent fuel rods not an assembly. Tobin suggests XRF could be used to quantify the Pu mass of a single rod or baskets of fuel rod pieces at the front end of an electrochemical processing facility. This would improve input accountability and provide independent verification of Pu mass before the spent fuel is dissolved. The spent fuel reprocessing cycle and spent fuel safeguards are addressed further in section 1.3.3.

1.3 Theory

1.3.1 X-Ray Fluorescence

XRF occurs when a tightly bound electron, usually in the K-shell, interacts with radiation whose energy is higher than the electron shell binding energy of the specific

element, causing the bound electron to be ejected from the electron cloud. The vacancy in the tightly bound electron shell is then filled by a loosely bound electron from an outer orbital; the increase in binding energy is then released as XRF. The XRF emission has energy equal to the difference of the electron shell binding energies and is specific to each element. For U and Pu, the x-rays from K-shell vacancies being filled have energies in the 95 to 117 keV range[2]. Figure 4 provides a simple example of how XRF works. An incoming photon knocks out a K-shell electron, the vacancy is filled by an L-shell electron and a characteristic x-ray is emitted. The L-shell vacancy is then filled by an outer shell and another characteristic x-ray is emitted. This process continues until the atom is in a neutral state.

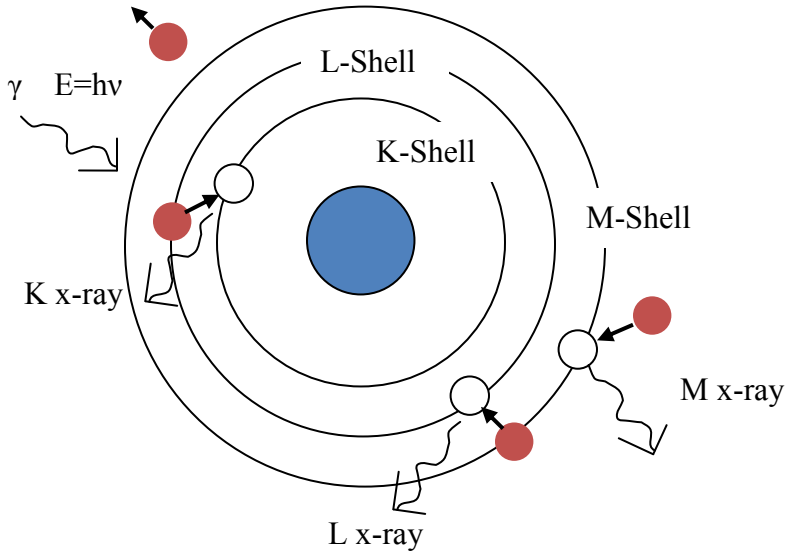

Figure 4. Simplified example of XRF

When a vacancy needs to be filled, an electron from the next closest shell does not necessarily fill the void. This is shown in the energy-level diagram shown in Figure 5[12].

If an M-shell electron fills a vacancy in the K-shell a K_β x-ray is emitted[12]. The major U and Pu K-shell energies are provided in

Table 1[13].

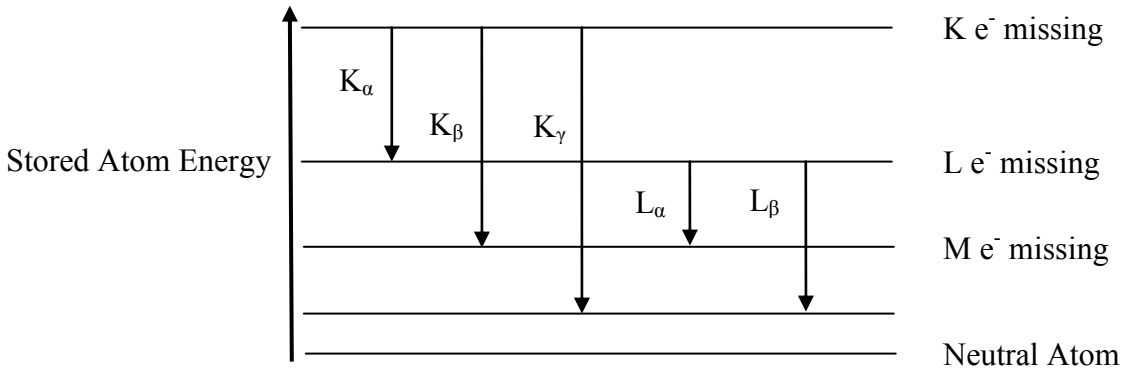

Figure 5. Schematic of electron energy-level diagram[12]

Table 1. Major U and Pu K-shell x-rays[13]

X Ray	Energy (keV)		Relative Intensity	
	Uranium	Plutonium	Uranium	Plutonium
$K_{\alpha 1}$	98.44	103.76	100	100
$K_{\alpha 2}$	94.67	99.55	61.9	62.5
$K_{\beta 1}$	111.30	117.26	22.0	22.2
$K_{\beta 2}$	114.50	120.60	12.3	12.5
$K_{\beta 3}$	110.41	116.27	11.6	11.7

Electron ejection, and thus XRF, can be induced by the photoelectric effect, beta particle interaction, or internal conversion. In U and Pu, most of the XRF is caused by the photoelectric effect due to the relatively large photoelectric absorption cross sections of these elements for gamma-rays from the spent fuel[2]. In the photoelectric effect, an incident photon has an inelastic collision with the atom. The photon raises the atom to an

excited state and the atom de-excites by ejecting one of its orbital electrons. The probability of a photoelectric effect reaction is proportional to the nuclide's atomic number (Z) to the power of 4[12], meaning the likelihood of XRF from U (Z=92) and Pu (Z=94) is drastically higher than the XRF from fission products such as Cs (Z=55). It is important to note that the photoelectric effect is an electromagnetic interaction with atomic electrons and thus elemental. Each element emits a characteristic x-ray spectrum[13]; therefore, the emitted XRF energies are the same for all isotopes of Pu. This fact allows the measurement of the U and Pu x-rays to provide a relative measurement of elemental content.

High Z materials also have high internal conversion factors. Internal conversion, which competes with gamma emission, is when an excited state nucleus transfers its energy directly to an atomic electron, and the electron is emitted[12]. Internal conversion creates a daughter element which contains vacancies in the K-shell or L-shell which leads to XRF characteristic of the daughter atom[13]. In high density material such as spent nuclear fuel, alpha, beta, and gamma radiation from the decay of fission products and actinides have interactions in parent material which leads to the production of x-rays characteristic of the parent atom[13]. In spent fuel, the decay of fission products dominates the XRF of Pu and U.

In theory, the U and Pu XRF peaks on the outer spent fuel edge (~300 μm) can be measured through the cladding using a high resolution gamma detector[11]. X-rays in the inner fuel regions are unable to be measured due to the high attenuation in the fuel. Once the Pu and U XRF photopeaks in the gamma spectrum are distinguishable and measured,

the ratio of the Pu to U x-ray photopeaks can be utilized to determine the Pu to U elemental ratio in the spent fuel[11]. Then the amount of Pu can be calculated using the known U mass and information on the distribution of the Pu in the spent fuel. In this thesis, the spent fuel isotopic distributions were simulated using modern radiation transport physics codes explained later.

1.3.2 Plutonium Production in Spent Fuel

Pu in a PWR is produced mainly by the transmutation of U-238 in the UO_2 fuel. The U-238 isotope absorbs a neutron and undergoes radiative capture, becoming U-239. The nuclear reaction is depicted as U-238(n, γ)U-239, and the microscopic radiative capture cross section is shown in Figure 6[14], from ENDF/B-6.

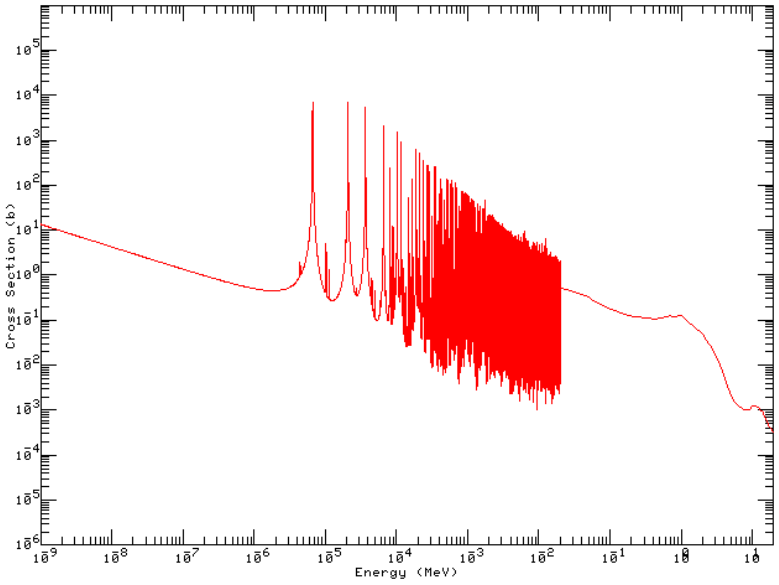

Figure 6. U-238 (n,γ) microscopic cross section[14]

U-239 with a short half-life of 24 minutes then beta decays to Np-239. It then beta decays to Pu-239, a fissile isotope. Figure 7 below displays a section of the U fuel depletion chain, showing the build-up of Pu isotopes[15].

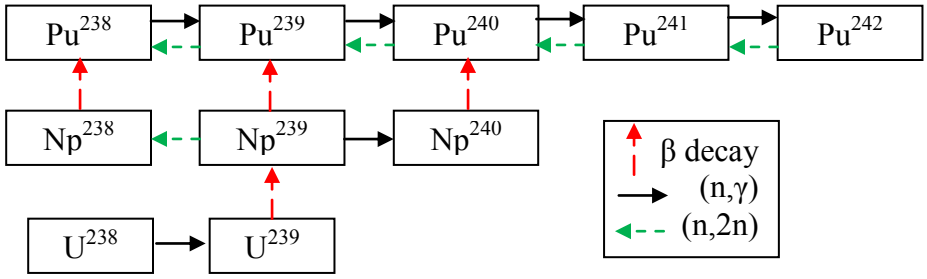

Figure 7. Pu build-up chain from U-238

During the fuel irradiation cycle, the different Pu isotopes build-up and eventually, for high burn-up cases, Pu-239, instead of U-235, becomes the dominating fissioning nuclide. However, not all of the Pu-239 bred in this fashion undergoes fission before fuel discharge, meaning Pu remains in the spent fuel[16]. Figure 8 displays an example of the relative Pu isotope masses as a function of burn-up for a PWR with an initial enrichment of 4%, provided by NEA/OECD[17].

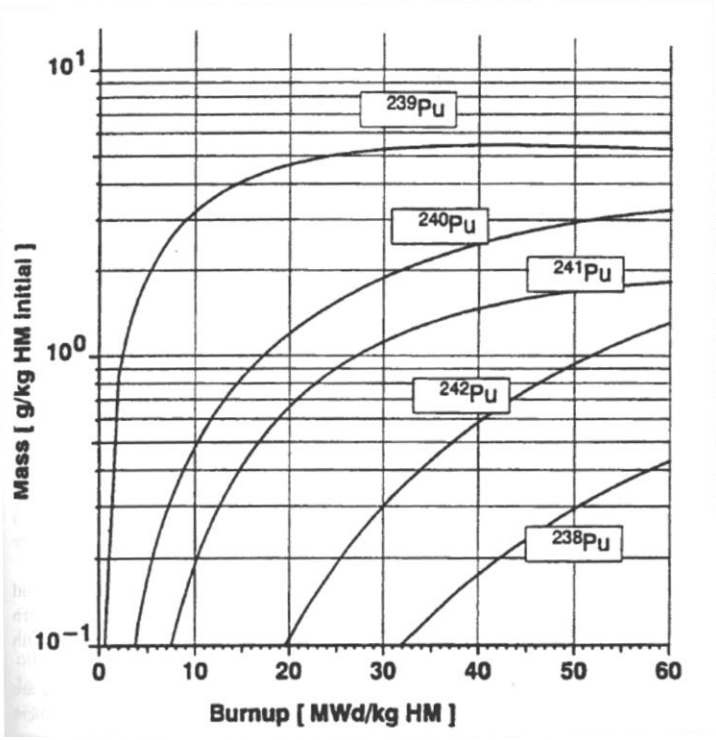

Figure 8. Pu isotope build-up in a PWR[17]

Figure 8 shows that Pu-239 is originally produced rapidly. It then reaches an equilibrium state near 40,000 MWd/ MTU and at very high burn-ups it slowly decreases from fissioning. Similar characteristics are seen for other Pu isotopes; however, it takes longer for the higher mass isotopes to reach an equilibrium state since they generally depend on absorptions from the lower mass Pu isotopes.

Figure 8 also shows relative low levels of Pu-238. This is typical for PWR spent fuel. By IAEA standards Pu containing less than 80% Pu-238 is a direct use material, meaning the material can be used to manufacture a nuclear explosive device without transmutation or further enrichment[18]. Therefore spent fuel from a PWR is considered irradiated direct use material and has an IAEA detection timeliness goal of three

months[18]. The following section covers safeguarding spent nuclear fuel and specifically the motivations for measuring Pu content in spent fuel.

1.3.3 Safeguarding Spent Fuel

The safeguards system for spent nuclear fuel comprises measures by which a regulating body [International Atomic Energy Agency (IAEA), Nuclear Regulatory Committee (NRC), or Department of Energy (DOE)] independently verifies the declarations of a State's nuclear material and activities. For irradiated fuel discharged from a reactor, the regulating body is interested in verifying that a significant quantity of special nuclear material (SNM) and is not diverted for a military purpose. Special nuclear material is defined by Title I of the Atomic Energy Act of 1954 as plutonium, uranium-233, or uranium enriched in the isotopes uranium-233 or uranium-235. For this discussion, only the special nuclear material Pu will be considered. By the IAEA standards, a significant quantity of Pu is 8 kg of Pu which contains less than 80% Pu-238[18].

As mentioned earlier, irradiated fuel is discharged from the reactor before all the fissionable nuclear material has depleted usually due to limits of cladding structural integrity, and the Pu inside the spent fuel contains much less than 80% Pu-238. Right now there is an estimated 980 metric tons of Pu worldwide in the nuclear fuel cycle (spent fuel and separated Pu), and a majority of the Pu resides in spent fuel[19]. Therefore, accountancy and independent verification of the amount of Pu in the spent fuel is of high importance. Tobin suggests there are five motivations for measuring the Pu content in spent fuel: independent verification, shipper/receiver differences, quantify Pu in spent

fuel that is not self-protecting (high dose rates), input accountability, and determining burn-up credit for a high-level waste repository[11].

When spent fuel is shipped from the reactor, the operator will declare a Pu content for each assembly. This declaration is likely produced from a reactor physics simulation using the assembly's known power history. Thus, it does not confirm a direct measurement. The reactor operator does not use this Pu content directly because he can account for spent fuel at his facility using item accounting. Item accounting is a method used by the IAEA to independently verify nuclear material accounting information and involves the counting of items in a batch or stratum for the purpose of verifying the correctness of the operator's records with respect to the number of items present[18]. Material is in item form as long as it consists of individually identifiable units that are kept intact (e.g. fuel assembly, bundle, or pin)[18]. At this point in time there is no NDA technique that can determine the amount of Pu in spent fuel[19]; therefore, the amount of Pu is based on operator declarations and physics codes with high uncertainties. Consider the scenario of the Pu pathway from the reactor spent fuel pool to a PUREX spent fuel reprocessing plant (RPP). A simplified schematic of the PUREX reprocessing cycle is provided in Figure 9 from *The Nuclear Fuel Cycle: Analysis and Management* 2nd Edition. During shipment from the reactor and receipt at the RPP, the assemblies are again accounted for by item accounting. Thus, as long as the integrity of the fuel is not violated, then the assemblies can simply be counted when they arrive at the receiver (RPP). That count can be compared to the shipper's (reactor) value, and there should be no uncertainty in the accountancy. At the RPP, the spent fuel assemblies are chopped

into pieces mechanically, and the fuel is dissolved from the clad hulls. The dissolved fuel and the dissolved fuel is put into the input accountability tank (IAT). In the IAT, a sample of the dissolved fuel is measured, typically using an isotopic dilution mass spectrometry (IDMS), providing the first measurement of bulk Pu content in the spent fuel. Since no previous measurements were performed, a diversion would likely go undetected during the mechanical de-cladding, chopping, and fuel dissolution process. To protect against this weakness, the RPP relies upon a very vigorous containment and surveillance system during mechanical de-cladding, chopping, and fuel dissolution process. However, this method provides an opportunity for diversion during the spent fuel transportation. Historically, when comparing the bulk Pu values at the IAT to the reactor operator declarations, a shipper-receiver difference is observed. This difference is likely due to bias errors in the reactor physics simulations; however, it could also be perceived as a protracted diversion.

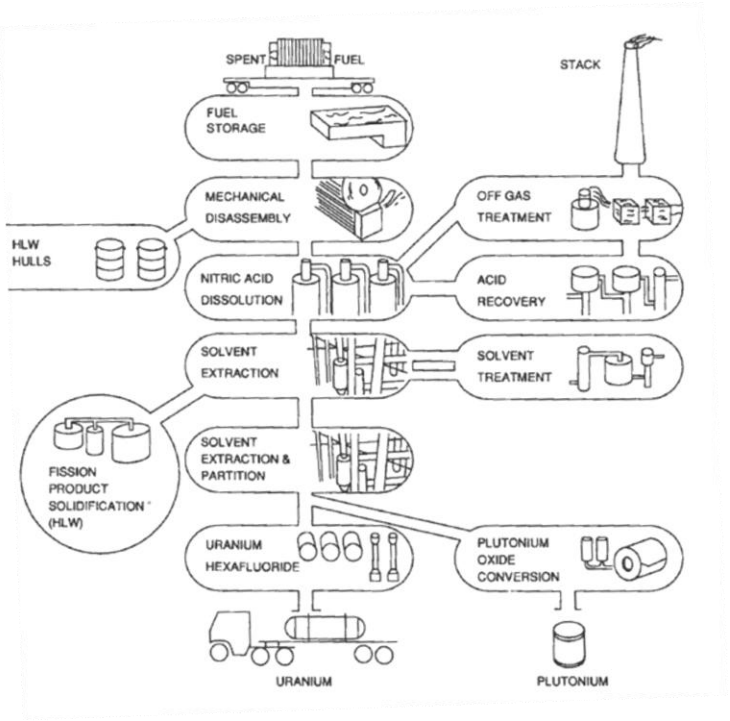

Figure 9. PUREX reprocessing cycle[20]

A Pu content measurement of spent fuel assemblies or individual rods would provide material accounting before the IAT and improve input accountability. This thesis investigates the measurement of individual spent nuclear fuel rods using XRF for Pu/U content. This technology would be implemented on a single fuel rod before chopping or on chopped pieces of fuel in a basket in the reprocessing cycle.

1.3.4 Modern Radiation Transport Physics Codes

Three modern radiation transport physics codes were used in this work for spent fuel measurement analysis and simulations: MCNP, TransLAT and Origen2. The following sections describe the main attributes of the three codes and provides an overview of how they will be utilized for the XRF simulations.

1.3.4.1 MCNP

MCNP is a general-purpose Monte Carlo N–Particle code that can be used for neutron, photon, electron, or coupled neutron-photon-electron transport. MCNP is developed and maintained by Los Alamos National Laboratory (LANL). MCNP solves the transport equation in an arbitrary three-dimensional configuration of materials in geometric cells[21]. For photons, MCNP accounts for coherent and incoherent scattering, fluorescent emission after photoelectric absorption, absorption in pair production, and bremsstrahlung[21]. For electrons, a continuous-slowing-down model is used that includes positrons, K-shell x-rays, and bremsstrahlung[21]. For this research, MCNP was used to model the detector system and the photon radiation transport from the spent fuel pin to the detector for the North Anna and TMI measurement campaigns, explained further in Section 4. For more information on the details of MCNP, visit the LANL website or refer to Reference 21.

1.3.4.2 TransLAT

TransLAT is a one, two, or three-dimensional lattice physics code for Light Water Reactor (LWR) nuclear fuel assembly designs, developed and maintained by TransWare Enterprises Inc. TransLAT is a multi-dimensional, multi-group, deterministic neutron transport code, based on the Method of Collision Probabilities and the Method of Characteristics[22]. TransLAT includes a nuclear data file, based on ENDF/B-VI that contains cross-section data in 97 neutron energy groups and 18 gamma-ray energy groups for over 300 nuclides[22]. For more information on the details of TransLAT, refer to the TransLAT manual on the TransWare Enterprises website (http://www.twe.com).

Two-dimensional TransLAT simulations were used to determine the radial distribution of actinides, minor actinides, and fission product concentrations in the North Anna and TMI spent fuel. The radial distribution of nuclides is needed for the material composition of the fuel and the source strength for the Monte Carlo detector system simulations. Detailed information on the TransLAT simulations is provided in section 3.

1.3.4.3 Origen2

Origen2 is a reactor physics code that calculates the buildup and decay of radioactive nuclides[23]. Origen2 is a zero-dimensional code that uses predefined reactor specific cross-section sets. Origen2 is developed and maintained by ORNL. For more information refer to the Origen users' manual, Reference 23. Origen2 simulations were conducted to simulate the relationship between the concentration of fission product nuclides and burn-up for the North Anna and TMI spent fuel at the specific XRF measurement locations.

2. SPENT FUEL ROD MEASUREMENTS

The following sections provide detailed information on the spent fuel rod measurements, measured data analysis, and detector system simulations.

2.1 May 2008 Spent Fuel Measurement Campaign

2.1.1 Experimental Set-up

In May 2008 Texas A&M University (TAMU) participated in North Anna spent nuclear fuel measurements performed at ORNL. These measurements were the first spent fuel PWR XRF measurements attempted with the collective effort of ORNL, LANL, and TAMU. Fission product gamma scans were also performed on the spent fuel rods to provide information about the axial distribution of the fission products and fuel burn-up. The spent fuel rods were measured inside the hot cell in building 3525 at ORNL.

The North Anna spent fuel was a UO_2 fuel with an initial enrichment of 4.199% U-235, M5 cladding (Zr + 1% Nb), and an operator declared burn-up of 67 GWd/MTU. The spent fuel rods were cut into various lengths before placed into shipping tubes for shipment to ORNL. Therefore, a single shipping tube will possibly carry pieces from different fuel rods, and a single fuel rod will be in several shipping tubes. The North Anna spent fuel rods measured were B16 and D5 that were inside the 651 and 652 shipping tubes, respectively.

The fission product gamma scans and XRF measurements used an ORTEC HPGe detector with ORTEC Maestro software. Both detectors used a lead collimator shield outside the hot cell wall. Both measurements also used a lead collimator in the hot cell

wall with a 1 mm to 3 mm pin hole or 2” slit collimator geometry. Figure 10 shows the experimental set up using the ORTEC detector for fission product gamma scans. The detector is inserted into the lead collimator shield and is aligned with the lead collimator in the hot cell wall. Figure 11 shows the collimator opening at the hot cell wall.

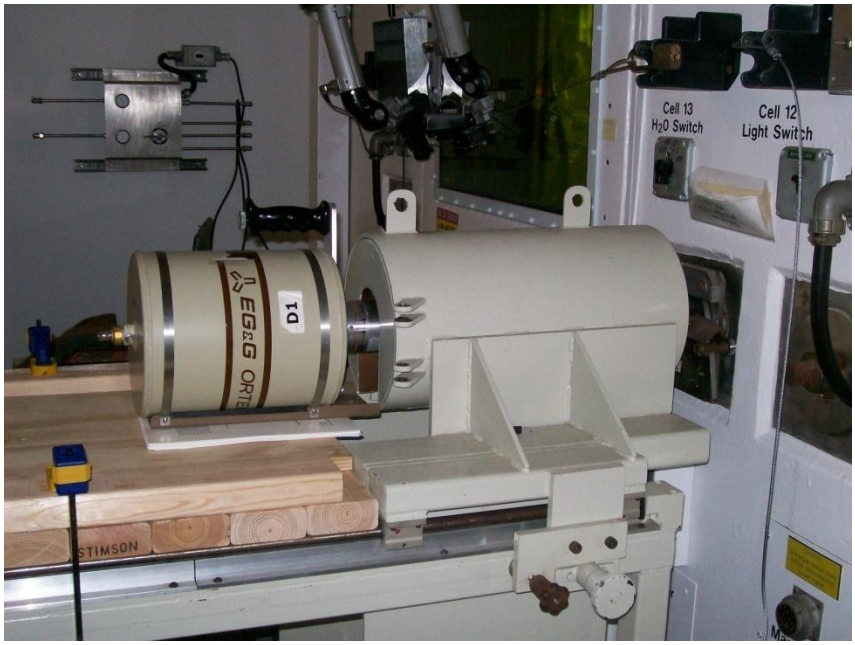

Figure 10. May 2008 measurement set up with ORTEC detector

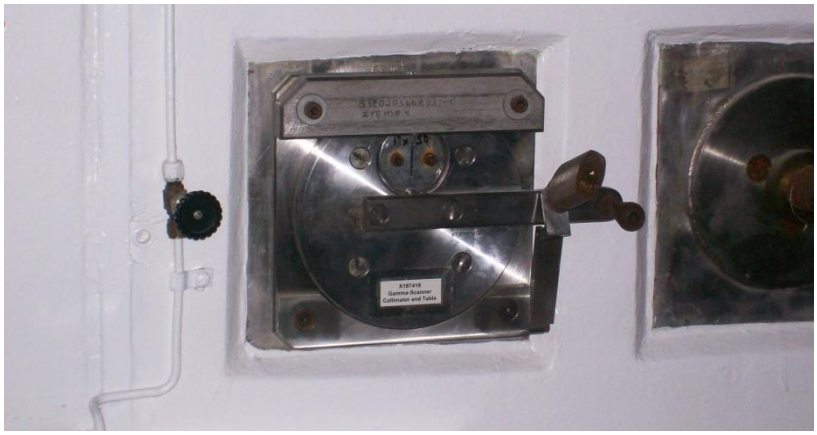

Figure 11. May 2008 end of lead collimator outside hot cell

Figure 12 shows a shipping tube held by the rod holding apparatus inside the hot cell, ready to be measured. The holding apparatus could move the rod laterally as well as vertically. The shipping tubes inside the hot cell were moved on and off the holding apparatus via robotic manipulators. The system for moving the rods laterally was not automatic. This created difficulty in recording the measurement location of the spent fuel rod.

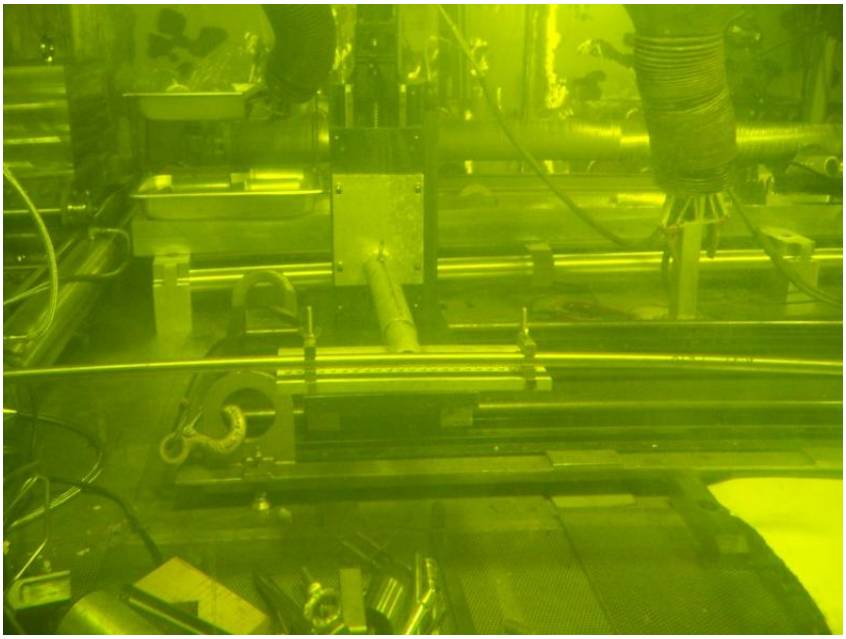

Figure 12. North Anna fuel rod inside the holding apparatus

2.1.2 Assessment of Results

The May 2008 XRF measurement campaign did not show a discernable Pu K-shell x-ray peak at 103.7 keV. Figure 13 shows a gamma spectrum measurement from a North Anna spent fuel rod. The Pu x-ray is not distinguishable due to the low signal-to-noise ratio. The measurements failed due to the large Compton continuum from the gamma-ray interactions in the fuel, detector, shielding, and other materials. Also, slumping of

the lead inside the collimator over time possibly caused a non-symmetrical geometry and additional noise in the detector, and the coaxial HPGe detector was inadequate for the x-ray energy range of interest. After these results were obtained, a simplified detector arrangement was simulated using MCNPX. It was determined that removing the detector shielding and using a planar HPGe would decrease the Compton continuum by a factor of ten[24,25].

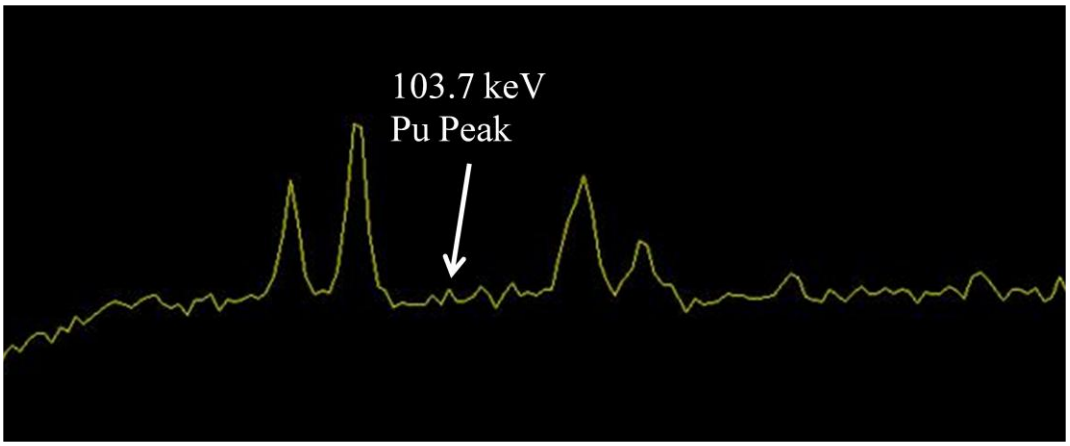

Figure 13. North Anna gamma-ray spectrum from May 2008 measurement campaign

2.2 July 2008 Spent Fuel Measurement Campaign

2.2.1 Experimental Set-up

In July 2008 additional measurements were taken of the North Anna spent fuel rods inside the hot cell in building 3525 at ORNL. The experimental set up was similar to the May 2008 measurements but with distinctive differences: the external lead collimator shield was excluded, a different spent fuel rod was measured, and a planar HPGe detector was used. XRF and fission product gamma measurements were performed on

the North Anna 649 shipping tubes. The North Anna spent fuel rod spanned five regions in the 649 shipping tubes: 649A, 649B, 649CD, 649EF and 649G.

The fission product gamma scans used a full spectrum ORTEC PopTop detector using ORTEC Maestro software and an Areva Canberra Falcon using Genie 2000 software. Both the Falcon and ORTEC PopTop are coaxial HPGe detectors. When using the ORTEC PopTop and Falcon the collimator hole was a 1" by 50 mil slit. Figure 14 shows the ORTEC PopTop detector taking measurements.

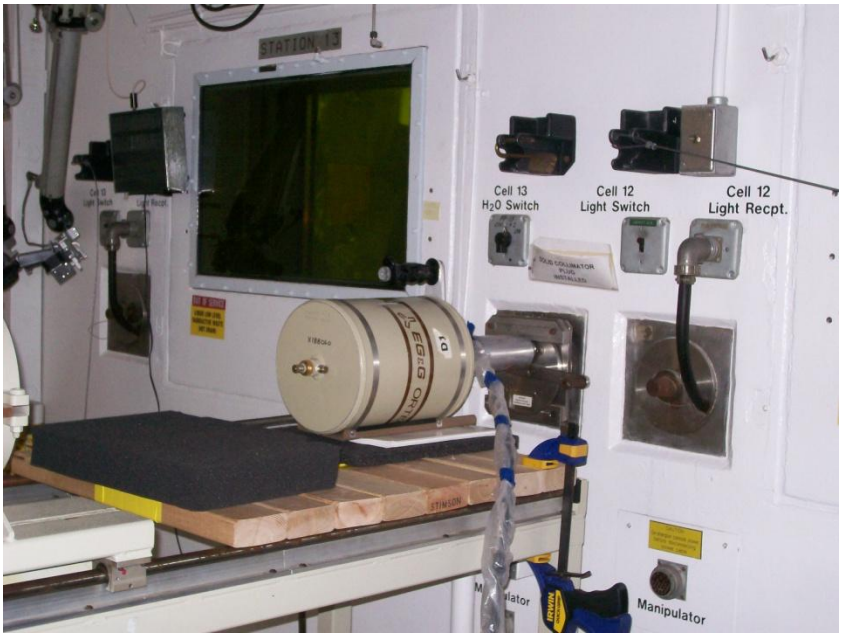

Figure 14. ORTEC PopTop fission product scans

For the XRF measurements a Low Energy Germanium Detector (LEGe) detector by Canberra was utilized, specifically a GL0515R model. This detector is a planar HPGe that is specialized to measure energies above 30 keV and below 300 keV with high resolution[26]. A thin planar HPGe detector configuration was chosen over a coaxial detector to decrease the surface dead layer. The surface dead layer in a detector is a non-

active layer which incident radiation must pass, causing radiation attenuation[27]. Usually the presence of the dead layer does not appreciably affect the detection efficiency, and the attenuation is negligible. However, when measuring lower energy x-rays the dead layer must be avoided to prevent attenuation. Also, the thinner detector crystal decreases the probability that a Compton scatter gamma produced from a Compton reaction in the crystal will interact in the crystal. This decreases the Compton continuum in the low energy region. For more information on planar and coaxial HPGe detectors and the surface dead layer, refer to Reference 27.

The LEGe used for the July 2008 measurements had an HPGe crystal with an active area of 500 mm^2, a thickness of 15 mm, and an active diameter of 25.2 mm[28]. The detector had a thin 0.5 mm aluminum (Al) window and a 3" tungsten (W) end cap[28]. Figure 15 shows the LEGe taking measurements of the North Anna spent fuel. Figure 16 shows a close up the detector.

Figure 15. July 2008 LEGe detector system

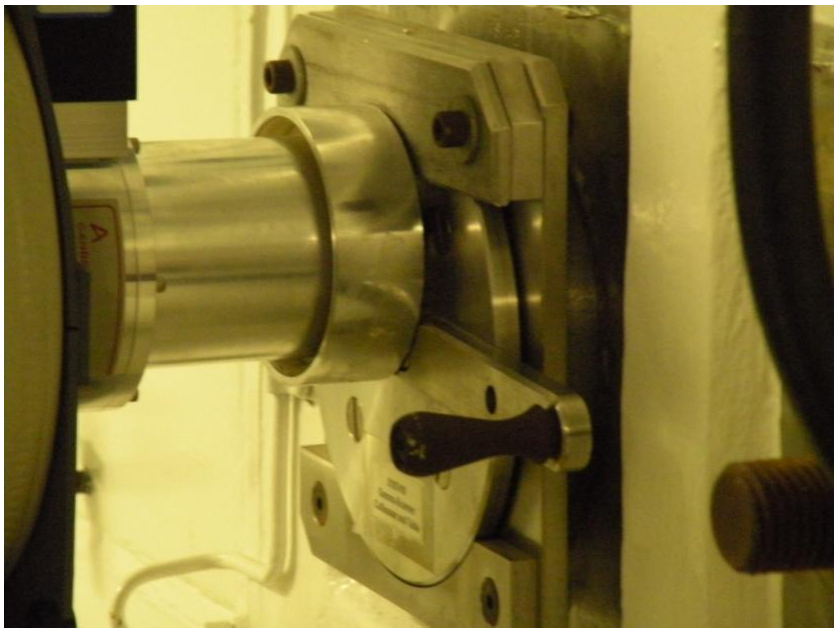

Figure 16. LEGe end cap

The detector was placed directly against the collimator, shown in Figure 16. The collimator pin hole is aligned with the fuel rod and the detector during the spent fuel

measurements. The stainless steel collimator was 36” in length and spanned the thickness of the hot cell wall. The collimator has two sections with different pin hole sizes. The hole starts from a 3 cm hole inside the hot cell and narrows to a pin hole diameter of 0.3 cm. The collimator end was an estimated 35” from the fuel rod inside the hot cell. The total distance between the spent fuel rod and the detector was an estimated 71”.

2.2.2 Measurement Procedures

2.2.2.1 Fission Product Gamma Scans

The general measurement procedure was to conduct fission product gamma scans over the length of the spent fuel rod and to perform an overnight or long XRF measurement at a specific location on the fuel rod. The shipping tubes, containing the North Anna spent fuel rod, were measured in the order 649CD, 649A, 649B, 649EF and 649G. Prior to performing fission product gamma scans, a 2 minute background measurement was taken and the detectors were energy and efficiency calibrated using Ba-133 and Eu-152 point sources.

The fission product gamma scans were measured along the axial length of the 649 shipping tubes using an ORTEC PopTop and Falcon. These scans were performed along the entire fuel rod in 3” increments. Each count was taken for 120 s (live time). The ends of the fuel segments were found by looking for the sharp depression in the count rate when between fuel segments. The relative measurement positions inside each shipping tube were recorded.

2.2.2.2 X-Ray Fluorescence Measurements

XRF measurements were performed using the LEGe detector on July 21-23, 2008. Each XRF measurement had a corresponding 2-3 minute fission product gamma measurement at or near that XRF location. Prior to measurements the detector was internally energy calibrated using a 2988.6 s count of 649CD and its measured U x-ray peaks. (i.e. The U x-ray peaks show a characteristic pattern that is easily recognizable and eliminates the need for a separate calibration source.)

Table 2 below displays the different count times for the XRF measurements. The blue cells show the measurements chosen for further analysis. These specific XRF spectra will be referred to by their shipping tube origin: 649A, 649CD, 649EF, and 649G. XRF measurements 649EF and 649G had corresponding fission product measurements at the same location, while 649CD and 649A XRF measurements had corresponding fission product measurements near the XRF location.

Table 2. North Anna XRF Count Time Data

Rod	Date of Measurement	Count Time (s)
649A	22-Jul	3600
649A	22-Jul	43303.69
649B	23-Jul	3600
649CD	21-Jul	2988.6
649CD	21-Jul	44263.53
649EF	23-Jul	3600
649G	Not Recorded	3600

2.2.3 Spectrum Analysis

2.2.3.1 Fission Product Gamma Scans

The fission product gamma scans provide information about the isotopic composition and burn-up profile of the spent fuel rod. This section provides fission product identification in the fission product gamma-ray measurements, and section 3.1.1 presents the fission product data analysis, including how the isotopic ratios were used as burn-up monitors. Figure 17 displays the fission product gamma-ray measurement at the 649A XRF reference location using Genie 2000 software. Figure 17 shows the presence of Cs-134 (with characteristic photopeaks at 563.2 keV, 569.3 keV, and 604.7 keV), Cs-137 (with a characteristic photopeak at 661.7 keV), and Sb-125 (with a characteristic photopeak at 635.9 keV). Figure 18 displays the same spectrum focused on higher energies. Figure 18 clearly shows a characteristic 1274 keV Eu-154 photopeak, 1168 keV Cs-134 photopeak, and small Co-60 1173 keV and 1332 keV peaks. Eu-154, Cs-134, Cs-137, and Sb-125 are all expected signatures when measuring spent nuclear PWR fuel. The Co-60 peaks originate from an interaction in structural materials. Table 3 summarizes the Cs-137 and Cs-134 measured counts at the energy peaks of interest from the fission product measurements at different locations.

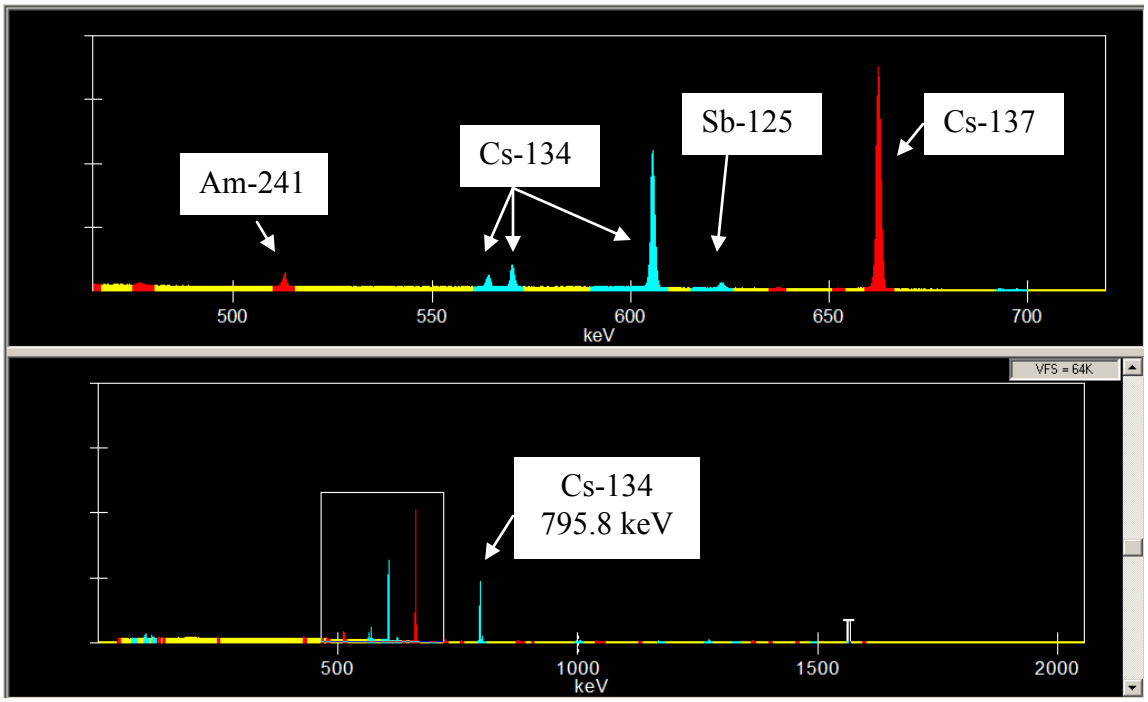

Figure 17. 2 min 649A fission product gamma measurement

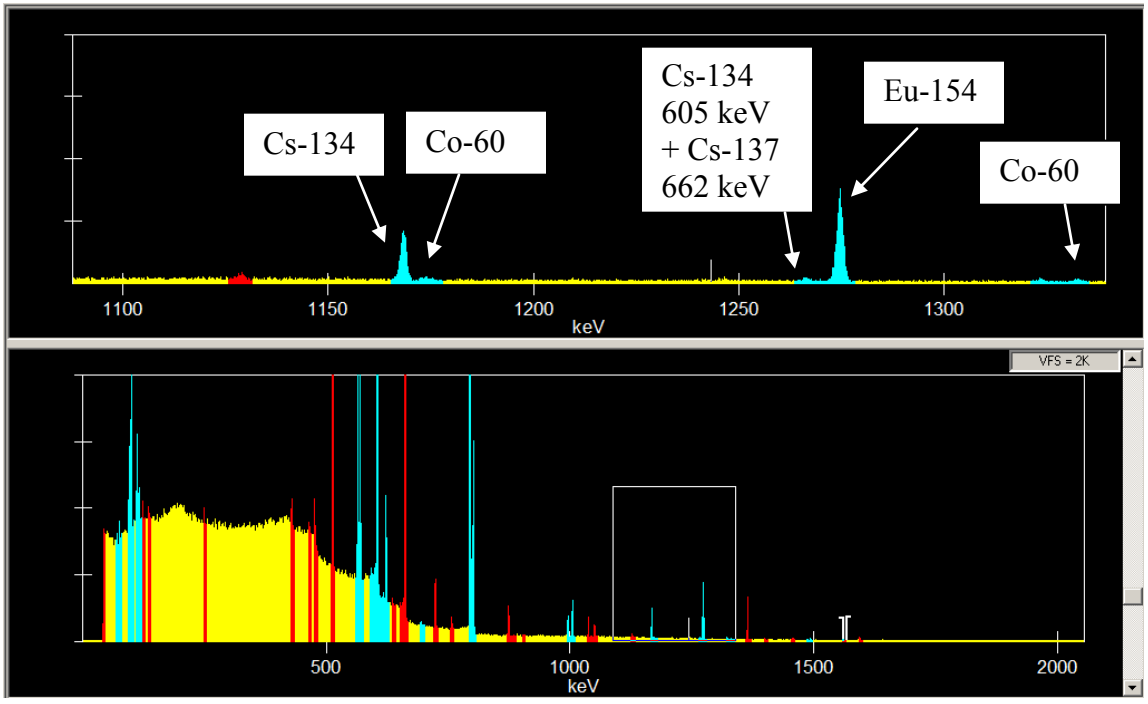

Figure 18. 2 min 649A fission product gamma measurement showing higher energies

Table 3. Summary of North Anna Cs-134 and Cs-137 count data

Rod Number	Relative Horizontal Position (in)	Cs-137 661.2	$\sigma_{(661.2)}$	Cs-134 563.26	$\sigma_{(563.26)}$	Cs-134 569.29	$\sigma_{(569.29)}$	Cs-134 604.66	$\sigma_{(604.66)}$
649 A	-3.000	**1.98E+05**	**466.11**	9.84E+03	122.29	1.84E+04	155.77	1.18E+05	351.05
649 C&D	9.001	**2.00E+05**	**459.64**	1.08E+04	127.32	2.00E+04	161.52	1.24E+05	361.11
649 E&F	34.863	**1.49E+05**	**399.03**	8.26E+03	111.7	1.50E+04	141.19	9.25E+04	312.5
649G	0.000	**1.60E+05**	**411.78**	8.17E+03	110.58	1.50E+04	140.59	9.36E+04	313.66

2.2.3.2 X-Ray Fluorescence Measurements

The July 2008 XRF measurements successfully showed the Pu K-shell x-ray peak at 103.7 keV in the gamma-ray spectra. This was the first instance that the Pu x-ray peak has been measured from PWR spent fuel. The previous Pu XRF measurements were taken of fast breeder reactor fuel which contained ~40% Pu. Typical PWR fuel has only ~1% Pu. The 649A XRF spectrum is shown in Figure 19. It includes the whole spectrum view and a close up of the x-ray region. In Figure 19, the U and Pu x-ray peaks and several other characteristic photopeaks are identified by labels. Eu-155 and Ce-144 are identified by their characteristic 105.3 keV and 133 keV peaks, respectively. The spectrum clearly shows the Pu x-ray peak at 103.7 keV and the U x-ray peaks at 94.6 keV, 98.4 keV, 111.3 keV, and 114.5 keV. The U x-ray peak at 110.4 is embedded in the 111.3 keV peaks with the top peak visible. In each measured XRF spectrum, the Pu 103.7 keV x-ray was clearly visible.

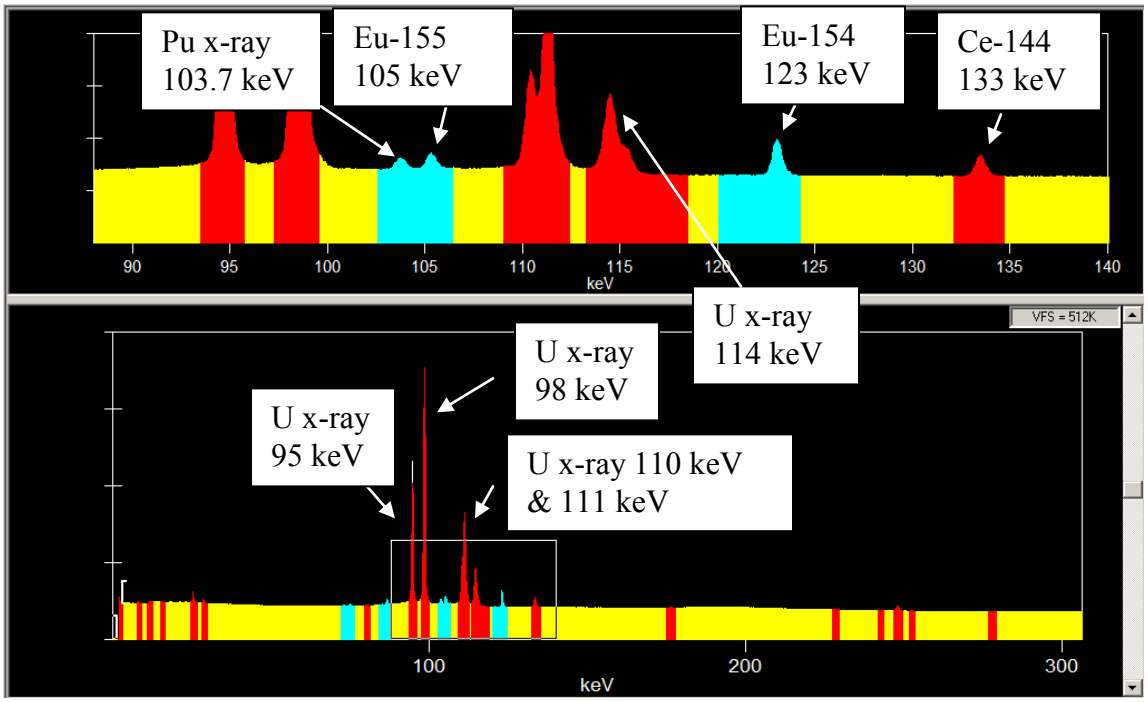

Figure 19. 649A XRF spectrum

2.3 January 2009 Spent Fuel Measurement Campaign

2.3.1 Experimental Set-up

In January 2009 measurements were taken of the D5 TMI spent fuel rod from assembly NJ05YU. The experimental set-up was completely different from the July 2008 set-up, using a more complicated collimator and an automated fuel handling system.

The TMI spent fuel rod was from a LWR with a nominal burn-up of 50 GWd/MTU and an initial enrichment of 4.0% U-235[29]. This rod originated from an assembly with substantial boron crud build-up, which eventually caused fuel failure during operation. As with the North Anna fuel rod, the TMI D5 fuel rod was divided into several shipping tubes: 616A, 616B, 616CD, and 616E.

The January 2009 experimental set-up inside the hot cell contained a rod positioning system called Advanced Diagnostics and Evaluation Platform (ADEPT) (shown in Figure 20) which allowed repeatable lateral positioning of the fuel rod in front of the collimator. The collimator collimates radiation into a thin beam through the hot cell wall to the detector. The collimator was 65.75” in length and was 8”from the fuel rod inside the hot cell. The collimator also had an extension piece outside the hot cell wall 12.25” in length. The detector was placed directly against the collimator extension, shown in Figure 21.

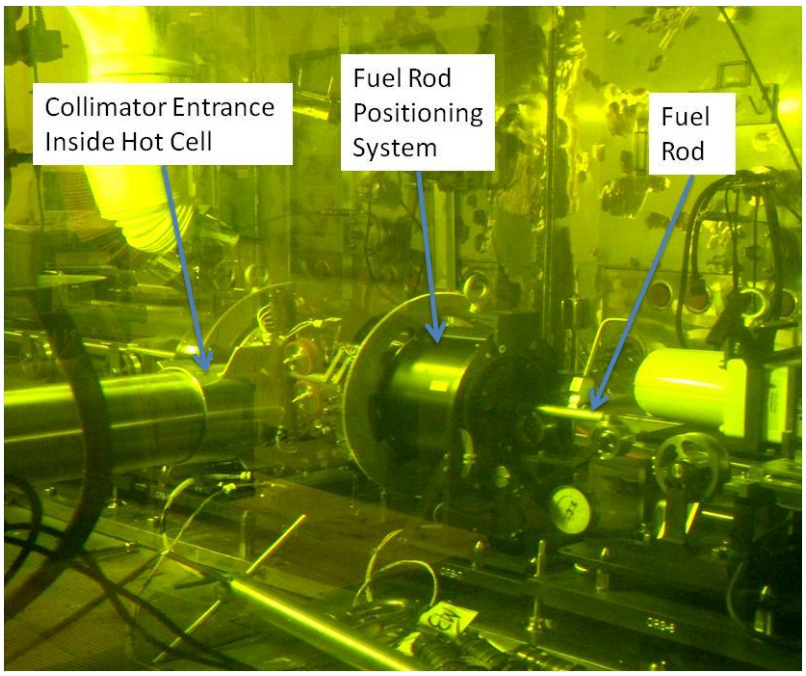

Figure 20. ADEPT system

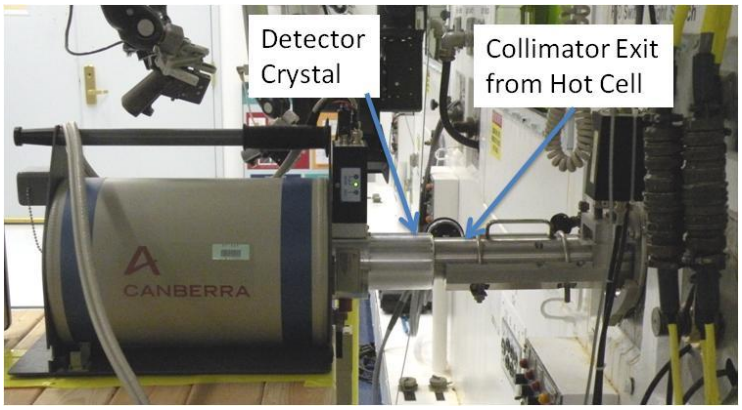

Figure 21. Collimator extension

The same LEGe and ORTEC PopTop detectors from the July 2008 measurements were used for the TMI XRF measurements and the fission product gamma scans. However, the tungsten 3” end cap of the LEGe was removed as shown in Figure 21. The fuel rod was aligned with the collimator hole such that the radiation would stream through the collimator to the detector crystal. During the XRF measurements, the fuel rod was 73.74” from the LEGe detector face.

Figure 22 shows the collimator outside of the hot cell for maintenance. The extension region is not connected to the main collimator in this picture, but the carriage piece for the extension is visible. Figure 23 shows the end view (closest to the fuel during measurements) of the collimator outside the hot cell. The collimator has two main pieces the stationary and movable collimator. The small movable insert piece (shown in Figure 23) can move in and out to change the size of the collimator hole.

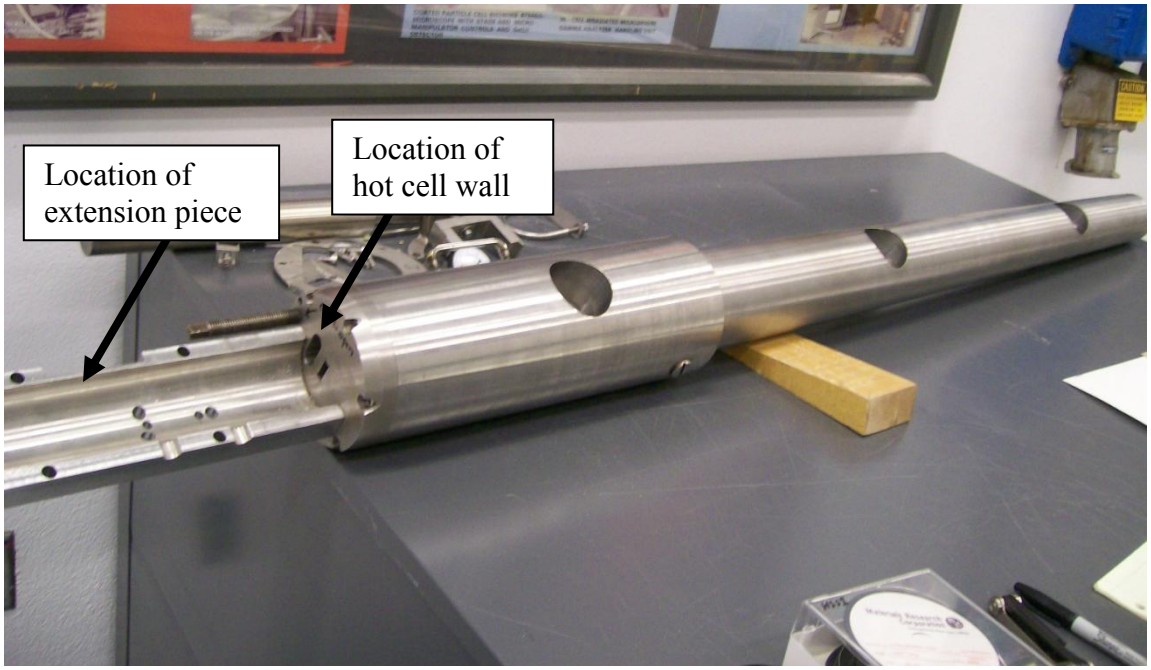

Figure 22. January 2009 measurement campaign collimator

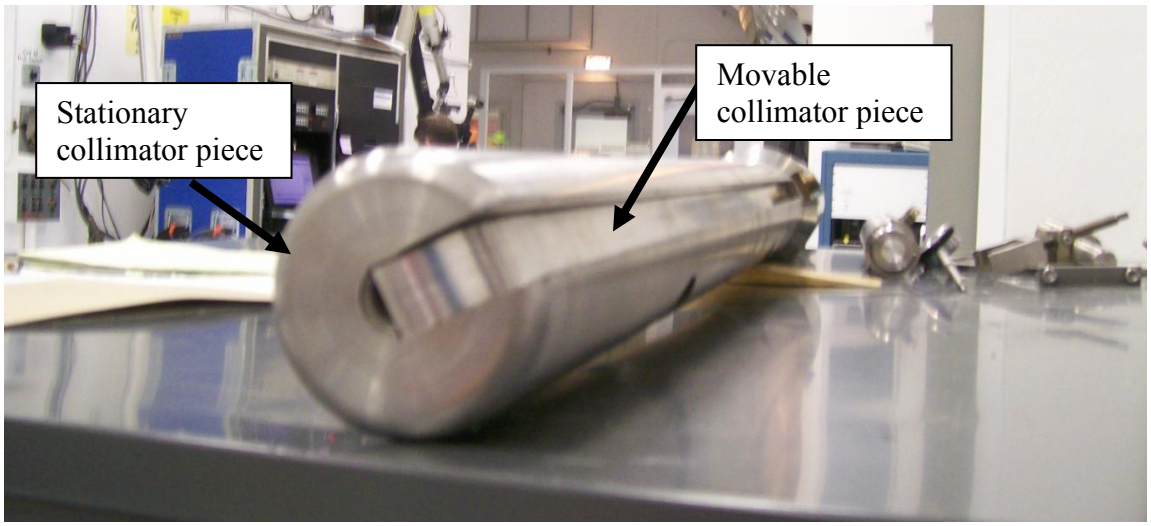

Figure 23. Collimator end

Figure 24 shows a close up of the collimator as it would be viewed from outside the hot cell wall location (with the upper extension piece removed). The collimator plate at the wall is stationary with slit dimensions of 0.75” by 0.25”.

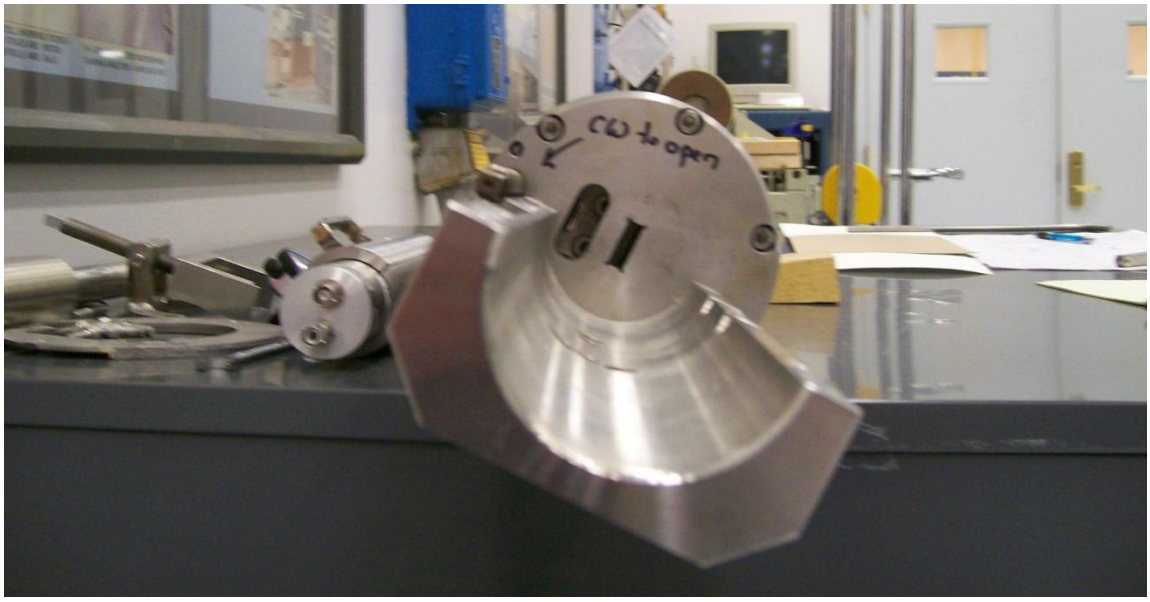

Figure 24. Collimator end plate

2.3.2 Measurement Procedures

2.3.2.1 Fission Product Gamma Scans

The general measurement procedure was to conduct the fission product gamma scans along the axial length of a fuel rod with the ORTEC PopTop in 75 mm increments and for 120s (live time), estimate the relative burn-up, select a location, perform a 10 minute fission product count with the ORTEC PopTop, and perform an overnight or long XRF measurement with the Canberra LEGe detector at the same location. Prior to the fission product gamma scans, the ORTEC Pop Top was positioned and energy calibrated with

Ba-133 and Eu-152 10 μCi point sources. Then the shipping tube would be changed. The rods were measured in the order 616A and 616CD.

2.3.2.2 X-Ray Fluorescence Measurements

The XRF measurement locations were chosen from the 2 minute gamma scan measurements. XRF measurement times varied from a few hours to 12 hours. Table **4** below displays the different count times and reference positions for the TMI XRF measurements. The reference position is the relative position of the measurement location along the fuel rod with respect to the fuel rod ends, during the measurement.

Table 4. TMI XRF Count Time Data

Rod Number	Reference Position (mm)	Measurement Time (s)
616 A	261	4.637E+04
616 A	550	5.623E+04
616 A	411	6.833E+03
616 A	530	6.262E+03
616 A	586	7.161E+03
616 A	661	8.276E+03
616 A	730	4.272E+04
616 CD	1984	6.371E+03

2.3.3 Spectrum Analysis

2.3.3.1 Fission Product Gamma Scans

The fission product gamma scans provide information about the isotopic composition and burn-up profile of the spent fuel rod. This section provides fission product identification in the fission product gamma-ray measurements, and section 3.2.1

presents the fission product data analysis. Figure 25 displays the fission product gamma-ray measurement at the 730 mm location on rod 616A for a 10 minute count using Genie 2000 software. Figure 25 shows the presence of Cs-134, Cs-137, Sb-125, and Eu-154. Since the TMI fuel is older than the North Anna fuel (13.3 years versus 4.2 years), certain shorter lived fission products are not visible in the spectrum. Figure 26 displays the entire spectrum with the Compton edge, Compton Continuum, and backscatter peak. Table 5 summarizes the Cs-137 and Cs-134 measured counts at the energy peaks of interest from the fission product measurements at different locations.

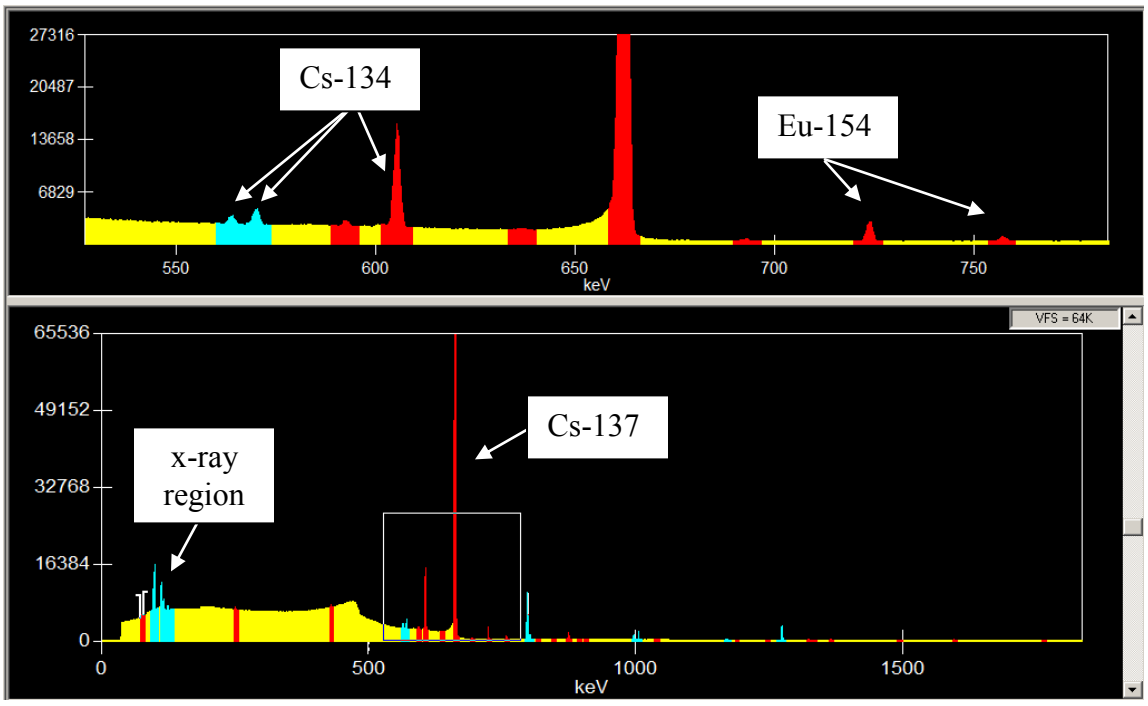

Figure 25. 10 min fission product gamma measurement at 730 mm rod 616A

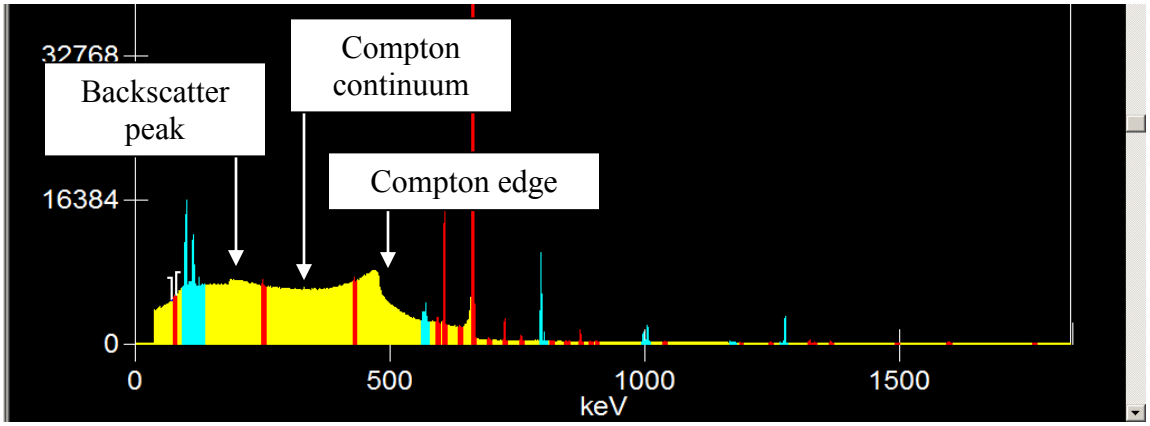

Figure 26. Features of 10 min 730 mm fission product scan

Table 5. Summary of TMI Cs-134 and Cs-137 count data

Rod Number	File Name/ Position	Relative Horizontal Position (in)	Cs-137 661.2	σ(661.2)	Cs-134 563.26	σ(563.26)	Cs-134 569.29	σ(569.29)	Cs-134 604.66	σ(604.66)
616 A	261	0.000	9.03E+05	969.78	1.28E+03	94.8	2.15E+03	105.98	1.44E+04	153.31
616 A	550	50.000	1.12E+06	1082.58	1.74E+03	114.91	3.68E+03	133.94	2.28E+04	280.46
616 A	411	150.000	1.43E+06	1223.32	2.78E+03	116	6.05E+03	138.72	3.73E+04	224.39
616 A	530	252.000	1.66E+06	1315.35	4.22E+03	130.94	7.87E+03	151.38	5.05E+04	258.05
616 A	586	325.000	1.83E+06	1328.45	4.67E+03	136.01	8.65E+03	157.29	5.29E+04	263.58
616 A	661	400.000	1.83E+06	1385.93	5.11E+03	140.88	9.48E+03	163.73	6.01E+04	279.06
616 A	730	452.000	1.82E+06	1396.18	5.11E+03	156.4	9.78E+03	177.19	6.09E+04	434.77
616 C&D	1984	0.000	2.00E+06	1451.03	5.99E+03	149.68	1.13E+04	174.62	6.91E+04	298.11

2.3.3.2 X-Ray Fluorescence Measurements

The January 2009 XRF measurements also successfully showed the Pu K-shell x-ray peak at 103.7 keV in each spectrum. The 730 mm 616A XRF spectrum is shown in Figure 27. This spectrum is qualitatively similar to the spectrum from the July 2008 measurements.

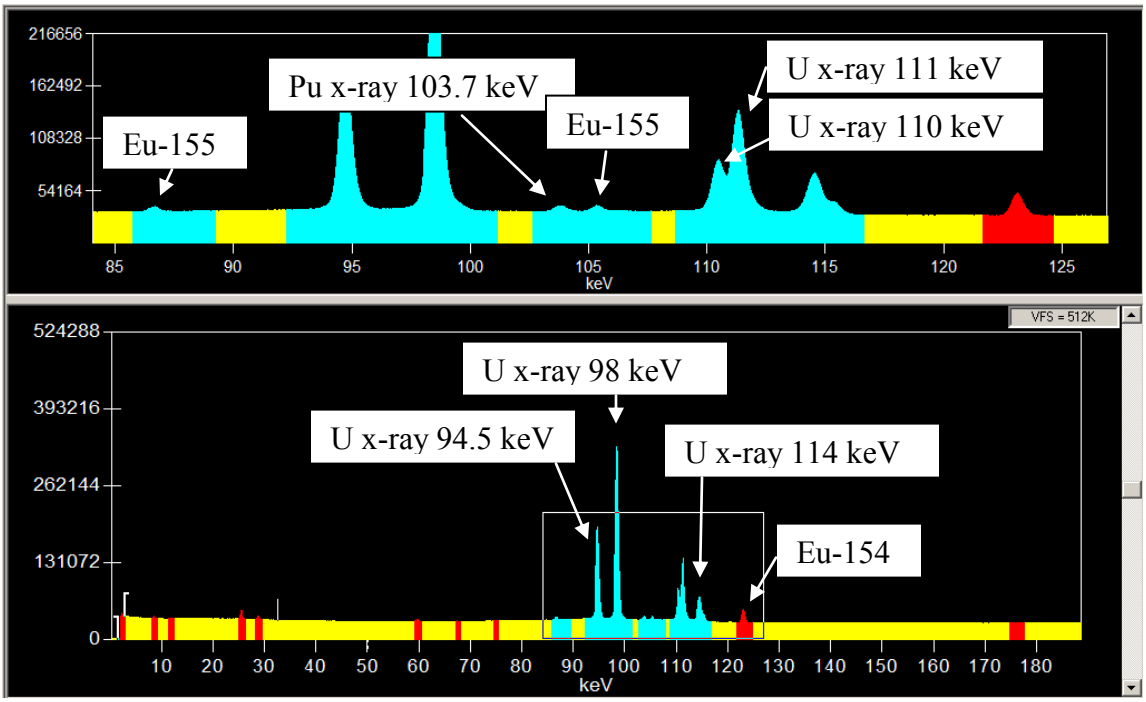

Figure 27. XRF spectrum at 730 mm on rod 616A

3. SPENT FUEL DATA ANALYSIS

3.1 Fission Product Data Analysis to Determine Fuel Burn-up

3.1.1 Derivation of Cs134/Cs137 Activity Ratio

After spent fuel is discharged from a reactor, the fuel burn-up can be determined using measurements of certain parameters, known as burn-up indicators that have known relationships with UO_2 fuel burn-up[20]. One particular method is to measure the activity ratio of Cs-134 to Cs-137. Cs-137 has the advantage of being produced by U and Pu with almost the same yield, having a long half life, having a small absorption cross section, and its concentration in spent fuel increasing almost linearly with fuel burn-up. Cs-134 is produced more through Pu-239 than U-235 as the fissioning isotope. A ratio measurement has the advantage of being a relative measurement, meaning the geometric efficiencies need not be included in the evaluation.

This section shows how the count ratio of two different photopeaks in a gamma spectrum can be correlated to an activity ratio. This derivation was applied to the isotopes of interest, Cs-134 and Cs-137, from July 2008 and January 2009 fission product gamma measurements. Later sections describe how the Cs-134 and Cs-137 activity ratios at the XRF measurement locations were then translated to the corresponding burn-up values.

Assume an experimental arrangement is configured such that a sample of several isotopes is isotropically emitting gamma-rays. Also assume the gamma-rays are born uniformly inside the sample, and the emitting isotopes have long half-lives in comparison to the measurement time. The experimental set-up includes a detector which

views the sample through a thick collimator. Assume the collimator is perfect, and radiation interactions with the collimator shielding are completely absorbed. Also assume the gamma-rays only interact in the sample, the collimator, and the detector. The system is surrounded by a vacuum.

The count rate (C'_{ij}) in the detector due to the gamma-rays of energy j emitted from the decays of isotope i is given by:

$$C'_{ij} = A_i Y_{ij} \varepsilon^{geo} \varepsilon_j^{int} \varepsilon_j^{sample} \quad (3)$$

where A_i is the rate of decay of isotope i in the sample (decays per second), Y_{ij} is the yield of gamma-rays of energy j from the decay of isotope i, ε^{geo} is the probability that a gamma-ray that escapes from the sample will have the correct solid angle to impinge upon the detector, ε_j^{int} is the probability that a gamma-ray that impinges upon the detector will interact in the detector active region and result in a count, and ε_j^{sample} is the probability that a gamma-ray of energy j that is born in the sample will escape the sample.

If two isotopes of interest (isotopes X and S) existed, isotope X emits gamma-rays of energy j, and isotope S emits gamma-rays of energy k, then the count rates in a photopeak would be given by:

$$C'_{Xj} = A_X Y_{Xj} \varepsilon^{geo} \varepsilon_j^{int} \varepsilon_j^{sample} \quad (4)$$

$$C'_{Sk} = A_S Y_{Sk} \varepsilon^{geo} \varepsilon_k^{int} \varepsilon_k^{sample} \quad (5)$$

Dividing Equation (4) is divided by Equation (5) yields,

$$\frac{C'_{Xj}}{C'_{Sk}} = \frac{A_X}{A_S}\frac{Y_{Xj}}{Y_{Sk}}\frac{\varepsilon_j^{int}}{\varepsilon_k^{int}}\frac{\varepsilon_j^{sample}}{\varepsilon_k^{sample}} \quad (6)$$

Solving Equation (6) for the ratio of activities,

$$\frac{A_X}{A_S} = \frac{C'_{Xj}}{C'_{Sk}}\frac{Y_{Sk}}{Y_{Xj}}\frac{\varepsilon_k^{int}}{\varepsilon_j^{int}}\frac{\varepsilon_k^{sample}}{\varepsilon_j^{sample}} \quad (7)$$

The isotope ratio of primary interest is the Cs-134/Cs-137 ratio. Since Cs-137 has only a single gamma-ray at 662 keV, Equation (7) becomes:

$$\frac{A_{134}}{A_{137}} = \frac{C'_{134,j}}{C'_{137,662}}\frac{Y_{137,662}}{Y_{134,j}}\frac{\varepsilon_{662}^{int}}{\varepsilon_j^{int}}\frac{\varepsilon_{662}^{sample}}{\varepsilon_j^{sample}} = R_{134/137,j} \quad (8)$$

The Cs-134/Cs-137 activity at the time of counting can be estimated from each Cs-134 gamma line; we will call this ratio $R_{134/137,j}$. The Cs-134 gamma lines include the 563 keV, 569 keV and 604 keV lines. Propagation of errors on Equation (8) will provide an estimate of the uncertainty in this ratio. This uncertainty is denoted as $\sigma_{134/137,j}$. By combining these estimated ratios using a combined average, the best estimate of the Cs-134/Cs-137 activity ratio is acquired using:

$$\bar{R}_{134/137} = \sum_{j=1}^{J} \frac{R_{134/137,j}}{\left(\sigma_{134/137,j}\right)^2} \Big/ \sum_{j=1}^{J} \frac{1}{\left(\sigma_{134/137,j}\right)^2} \quad (9)$$

The uncertainty in this best estimate is given by

$$\bar{\sigma}_{134/137} = \left[\sum_{j=1}^{J} \frac{1}{\left(\sigma_{134/137,j}\right)^2}\right]^{-1/2} \quad (10)$$

Thus, $\bar{R}_{134/137} \pm \bar{\sigma}_{134/137}$ can be acquired from the ratio of count rates from the measurements, the ratios of yields are known from nuclear data libraries, and estimates of the ratios of escape probabilities and intrinsic efficiencies. The yields for the lines of

interest are shown in Table 6. The ratio of intrinsic efficiencies can be acquired from a measurement of a Eu-152 point source. The ratio of sample escape probabilities can be acquired by simulating the sample in MCNP5 and calculating the probabilities of gamma-rays of various energies escaping the sample.

Table 6. Summary of half-lives and yields of gamma lines of interest[14]

Isotope	**Photopeak Energy (keV)**	**Half-life (years)**	**Yield (%)**
Cs-134	563.26	2.0652	8.338
Cs-134	569.29	2.0652	15.373
Cs-134	604.66	2.0652	97.62
Cs-137	661.2	30.08	85.1

3.1.2 Probability of Escape Calculation

An identification slice of each sample was simulated using MCNP5 to calculate the probabilities of gamma-rays of various energies escaping the sample. The fuel pin dimensions are known. Each fuel pin (and shipping tube) was then simulated explicitly using MCNP5. Multiple MCNP5 simulations were executed using a homogenously distributed gamma-ray source inside the fuel at discrete energies. Eleven discrete energies were used: 0.4 MeV, 0.5 MeV, 0.6 MeV, 0.662 MeV (energy of Cs-137 gamma –ray), 0.7 MeV, 0.8 MeV, 0.9 MeV, 1 MeV, 1.1 MeV, 1.2 MeV and 1.3 MeV. A surface tally (f2) was obtained at the shipping tube outer surface. This tally provided the surface photon flux (photons/cm^2/s) at the discrete energy (+/- 0.0001 energy bin width) on the outside of the shipping tube.

The relative probabilities of gamma-rays escaping the fuel rod at various energies to 662 keV (Cs-137 gamma-ray energy) was calculated using:

$$\frac{\varepsilon_j^{sample}}{\varepsilon_{662}^{sample}} = \frac{\theta_j}{\theta_{662}} \tag{11}$$

where θ_j is the MCNP-calculated surface photon flux on the shipping tube outer surface with an initial photon energy of j and θ_{662} is the MCNP-calculated surface photon flux on the shipping tube outer surface with an initial photon energy of 662 keV. Error propagation was included in the calculations.

The procedure described above was used to calculate the ratio of escape probabilities for the North Anna and TMI fuels. The data given in Table 7 was used for the MCNP simulations. The MCNP5 surface flux results for the North Anna and TMI fuels are provided in Appendix A and C, respectively. The resultant escape probabilities versus energy are shown in Figure 28 for both the North Anna (red) and TMI (blue) fuels. As can be seen, the two have nearly identical escape ratios. Also displayed on the plots are polynomial fits to the MCNP5 calculated data points. These fits could be used to determine this ratio for any energy between 400 and 1300 keV. Using the polynomial fits, the escape ratios for the photopeaks of interest from Cs-137 and Cs-134 for the North Anna and TMI fuels were calculated. Those ratios are shown in Table 8.

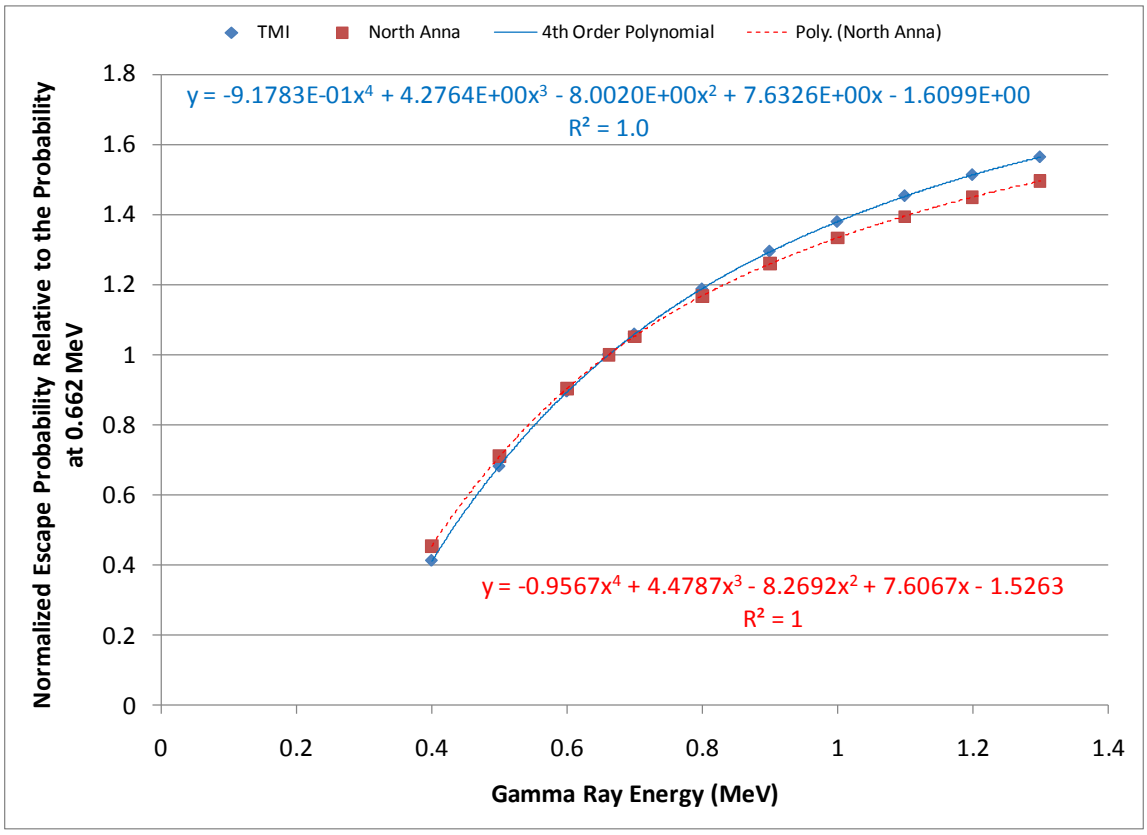

Figure 28. Escape probabilities for the North Anna and TMI fuel rods

Table 7. Fuel Data for Escape Ratio Calculations

Parameter	North Anna	TMI
Fuel Material	UO_2	UO_2
Fuel Enrichment	3 w/o	3 w/o
Fuel Pin Radius	0.40958 cm	0.4681 cm
Clad Material	M5	Zircalloy-4
Clad Thickness	0.057 cm	0.069 cm
Shipping Tube Material	Stainless Steel	Stainless Steel
Shipping Tube Thickness	0.15875 cm	0.15875 cm

Table 8. Escape Ratios for North Anna and TMI fuels

Isotope	Photopeak Energy (keV)	Escape Ratio	
		North Anna	TMI
Cs-134	563.26	0.839	0.822
Cs-134	569.29	0.850	0.834
Cs-134	604.66	0.912	0.902
Cs-137	661.2	1.00	1.00

3.1.3 Efficiency Calibration

The ratio of intrinsic efficiencies can be acquired from a gamma-ray measurement of a Eu-152 source. Only the relative efficiencies at various energies are needed. Thus, a high accuracy calibration standard is not required. The intrinsic relative efficiency calibration was determined for each measurement campaign by measuring a Eu-152 gamma-ray spectrum and calculating the efficiency relative to the gamma-ray yield, using:

$$\varepsilon_{Xj}^{inc} = \frac{C\prime_{Xj}}{Y_{Xj}} \tag{12}$$

Figure 29 displays the calculated efficiency results as a function of energy and a polynomial fit to these results for both the TMI (red) and North Anna (blue) measurement campaigns. There is more error in the TMI peaks than the North Anna data, providing a significant source of error in the calculated TMI intrinsic efficiencies. The individual spectrum peak net areas, corresponding gamma-ray yields, and calculated efficiency results are included in Appendix A and Appendix C. This fit was used to determine the relative efficiencies of the Cs-134 and Cs-137 fission product photopeaks. Table 9 summarizes the calculated intrinsic efficiencies for both the North Anna and TMI measurements.

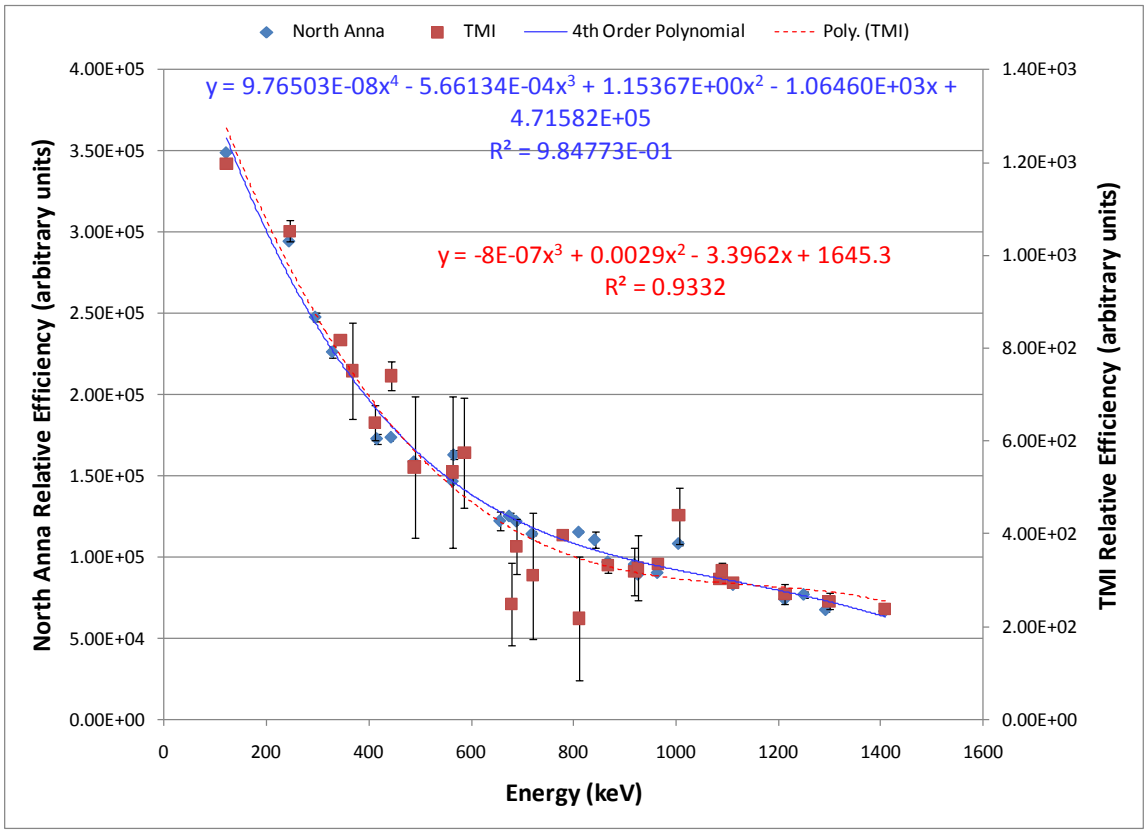

Figure 29. North Anna and TMI relative intrinsic efficiencies using Eu-152 calibration source

Table 9. Relative intrinsic efficiencies for the North Anna Cs-134 and Cs-137 peaks

Isotope	**Photopeak Energy (keV)**	**Relative Intrinsic Efficiency (arbitrary units)**	
		North Anna	TMI
Cs-134	563.26	1.466E+05	5.011E+02
Cs-134	569.29	1.452E+05	4.955E+02
Cs-134	604.66	1.376E+05	4.648E+02
Cs-137	661.2	1.270R+05	4.229E+02

3.1.4 Calculating the Cs-134/Cs-137 Activity Ratio

After the probability of escape and relative intrinsic efficiency as a function of energy were determined for each fuel and at the photopeak energies of interest, the Cs-134/Cs-137 ratios were calculated using Equations (8), (9) and (10). Table 10 summarizes the best estimate Cs-134/Cs-137 activity ratios at the different locations for the North Anna fuel. Table 11 summarizes the best estimate Cs-134/Cs-137 activity ratios for the TMI fuel. From reactor physics, it is known that as burn-up increases the Cs-134/Cs-137 activity ratio increases. Therefore it can be concluded from the calculations that the burn-up of the measured rod locations for the North Anna fuel increase in the following order: 649G, 649A, 649CD and 649EF.

Table 10. North Anna Cs-134/Cs-137 activity ratios

Rod Number	**Cs-134/Cs-137 Activity Ratio**
649A	0.5264 ± 0.0018
649CD	0.5520 ± 0.0018
649EF	0.5540 ± 0.0021
649G	0.5203 ± 0.0019

Table 11. TMI Cs-134/Cs-137 activity ratios

Rod Number	Reference Position (mm)	Cs-134/Cs-137 Activity Ratio
616 A	261	0.01399 ± 0.00014
616 A	550	0.01788 ± 0.00021
616 A	411	0.02290 ± 0.00013
616 A	530	0.02672 ± 0.00013
616 A	586	0.02550 ± 0.00012
616 A	661	0.02888 ± 0.00013
616 A	730	0.02951 ± 0.00019
616 CD	1984	0.03047 ± 0.00013

3.1.5 Translation to Burn-up

We relate the Cs-134/Cs-137 activity ratio to burn-up using the expected Cs-134/Cs-137 ratio for the fuel as a function of burn-up. This relationship was established using the zero-dimensional reactor physics code Origen2. The initial enrichment of the fuel, the operational history, and discharge date of the fuel was input into Origen2.

The North Anna fuel was a four cycle fuel, meaning the fuel went through 4 operational cycles and four shutdowns. The cycle burn-up values and operation times were provided by Reference 31. The specific power was calculated by dividing the cycle burn-up by the number of operational days. Table 12 provides a summary of the operational history, cycle burn-up and cycle specific power for the North Anna fuel.

Table 12. Summary of North Anna operation history

	Days	Cumulative Days	Cumulative Burn-up (MWd/MTU)	Cycle Burn-up (MWd/MTU)	Specific Power (W/g)
Cycle 1	460	460	22424	22424	48.7478
Shutdown 1	24	484			
Cycle 2	522	1006	46390	23966	45.9119
Shutdown 2	26	1032			
Cycle 3	520	1552	52461	6071	11.675
Shutdown 3	511	2063			
Cycle 4	455	2518	67615	15154	33.3055
Shutdown 4	1551	4069			

The TMI D5 fuel rod was a two cycle fuel. The operation times and cycle burn-up values at different axial locations for rod H6 were provided. The TMI rod D5 came from the same assembly as H6, so these burn-up values were averaged to provide a cycle burn-up for these simulations. The specific power was calculated by dividing the averaged cycle burn-up by the number of operational days. Table 13 provides a summary of the operational history, averaged cycle burn-up and calculated cycle specific power.

Table 13. Summary of TMI operation history

	Days	Hours	Cumulative Days	Cumulative Burnup (MWd/MTU)	Cycle Burnup (MWd/MTU)	Specific Power (W/g)
Cycle 1	666	15984	666	26529.625	26529.625	39.8343
Shutdown 1	35	840	701			
Cycle 2	693	16632	1394	48736.75	22207.125	32.0449
Shutdown 2	4870	116880	6264			

The Origen2 simulations used the US-PWR predefined cross sections sets. An initial enrichment of 4.199% U-235 and 4.0% U-235 was used for the North Anna and TMI fuels, respectively. The simulations modeled the operational and shutdown times while using scaled specific power values. Eight simulations were executed using specific power scaling factors of 0.25, 0.5, 0.75, 0.9, 1, 1.1, 1.25, and 1.5. These simulations provided a spectrum of fuel burn-up with the same operational history. The Origen2 outputs provided an estimated radioactivity of actinides and fission product isotopes on the day of the measurement campaign. Figure 30 shows the Cs-134/Cs-137 activity ratio as a function of fuel burn-up from the Origen2 simulations.

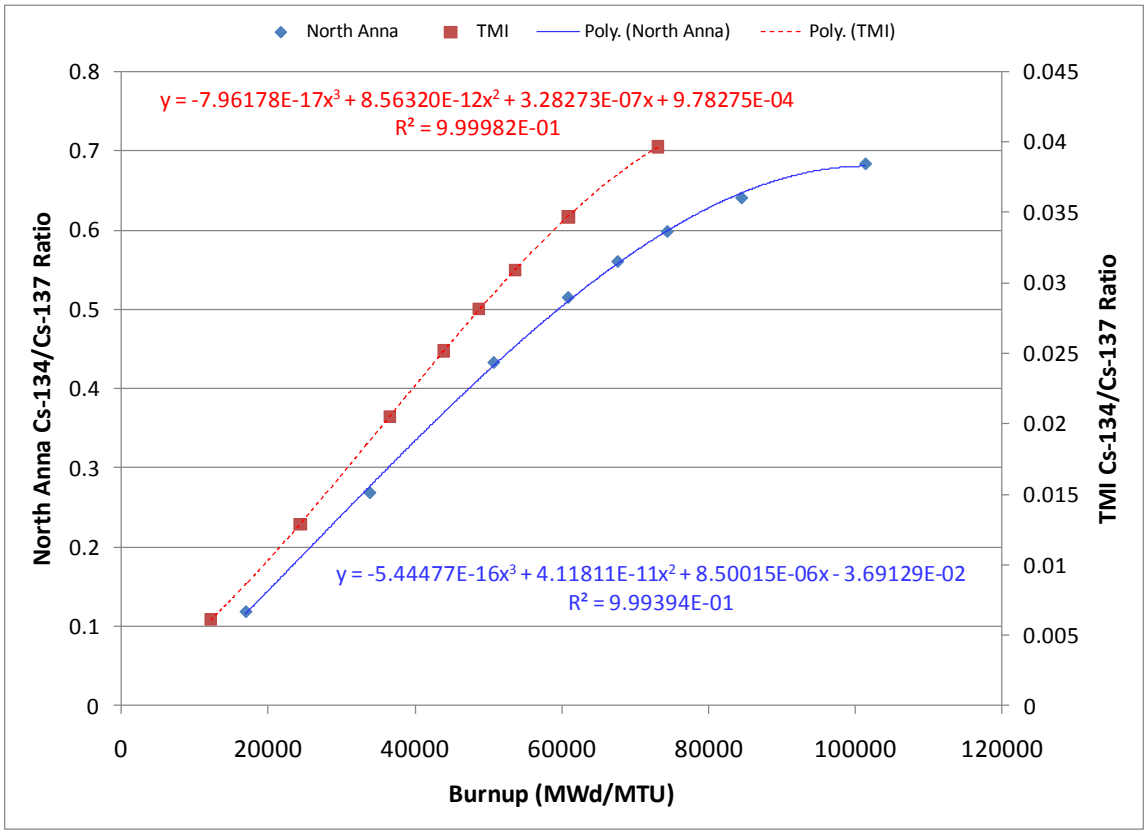

Figure 30. Cs-134/Cs-137 versus burn-up from North Anna and TMI Origen2 simulations

To determine the burn-up at the XRF measurement locations, the calculated Cs-134/Cs-137 activity ratios (Table 10 and Table 11) were fit to the polynomial trend-lines in Figure 30. Table 14 displays the correlated burn-up results. The burn-up values for the North Anna fuel range from 62-67 GWd/MTU. Thus, the North Anna XRF measurements did not cover a wide burn-up range. The burn-up values for the TMI fuel ranged from 27-59 GWd/MTU.

Table 14. North Anna and TMI correlated burn-up

Fuel	**Rod Number/Position**	**Correlated Burn-up (MWd/MTU)**
North Anna	649A	63064
North Anna	649CD	66744
North Anna	649EF	67021
North Anna	649G	62184
TMI	616A 261 mm	26699
TMI	616A 550 mm	33441
TMI	616A 411 mm	42674
TMI	616A 530 mm	50496
TMI	616A 586 mm	47904
TMI	616A 730 mm	56857
TMI	616CD 1984 mm	59209

3.2 Plutonium/Uranium Photopeak Analysis

The XRF spectra from the July 2008 and January 2009 campaigns were analyzed using Canberra's Genie 2000 software. The spectra were analyzed using an interactive peak fit to acquire peak areas (counts) for the Pu x-ray peak at 103.7 keV and the U x-

ray peaks at 98.4 keV and 94.6 keV. The 103.7 keV and 98.4 keV x-ray lines are both $K_{\alpha 1}$ lines and have a relative intensity of 100%. Figure 31 shows the interactive peak fit analysis for the Pu x-ray at 103.7 keV and the Eu-155 105.3 keV peak.

Figure 32 displays the Pu 103.7 keV x-ray peak to the U 94.6 keV x-ray peak ratio versus the correlated burn-up values at the measured locations for the North Anna fuels. This plot does show a linear relationship between the Pu 103.7 keV/U 94.6 keV x-ray peak ratio and the fuel burn-up, but these measurements only cover a small burn-up range (62-67GWd/MTU). Therefore these XRF measurement results are not quantitative, but are qualitative. A larger burn-up range was needed to conclude a definite relationship between the Pu/U x-ray peak and burn-up.

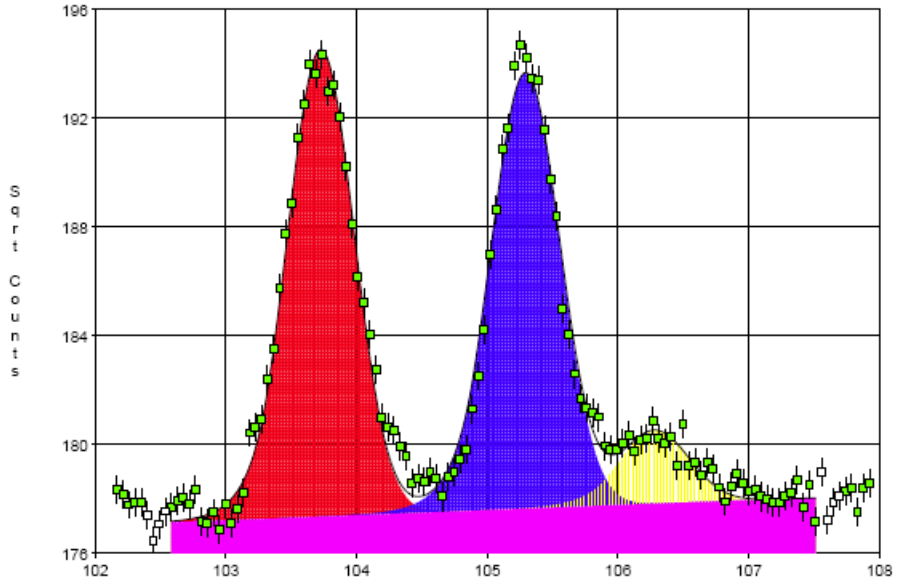

Figure 31. Interactive peak analysis for XRF measurements

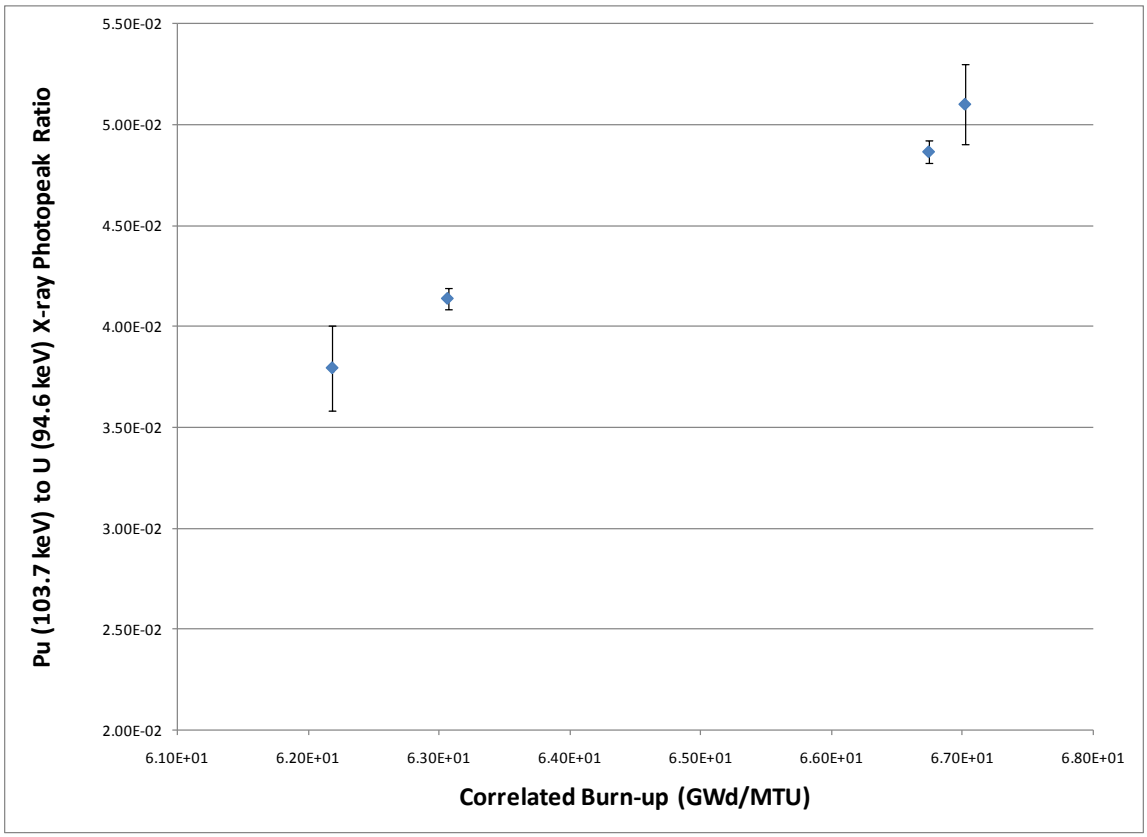

Figure 32. North Anna Pu (103.7 keV)/U (94.6 keV) x-ray peak ratio as a function of corresponding burn-up

Figure 33 displays the ratio of the Pu 103.7 keV x-ray peak to the U 94.6 keV x-ray peak versus the correlated burn-up values at the measured locations for the TMI fuel. This plot shows a linear relationship between the Pu 103.7 keV/U 94.6 keV x-ray peak ratio and the fuel burn-up. The TMI XRF measurements provided quantitative results, measuring the Pu to U photopeak ratio as a function of burn-up with burn-ups ranging from 27 GWd/MTU to 59 GWd/MTU.

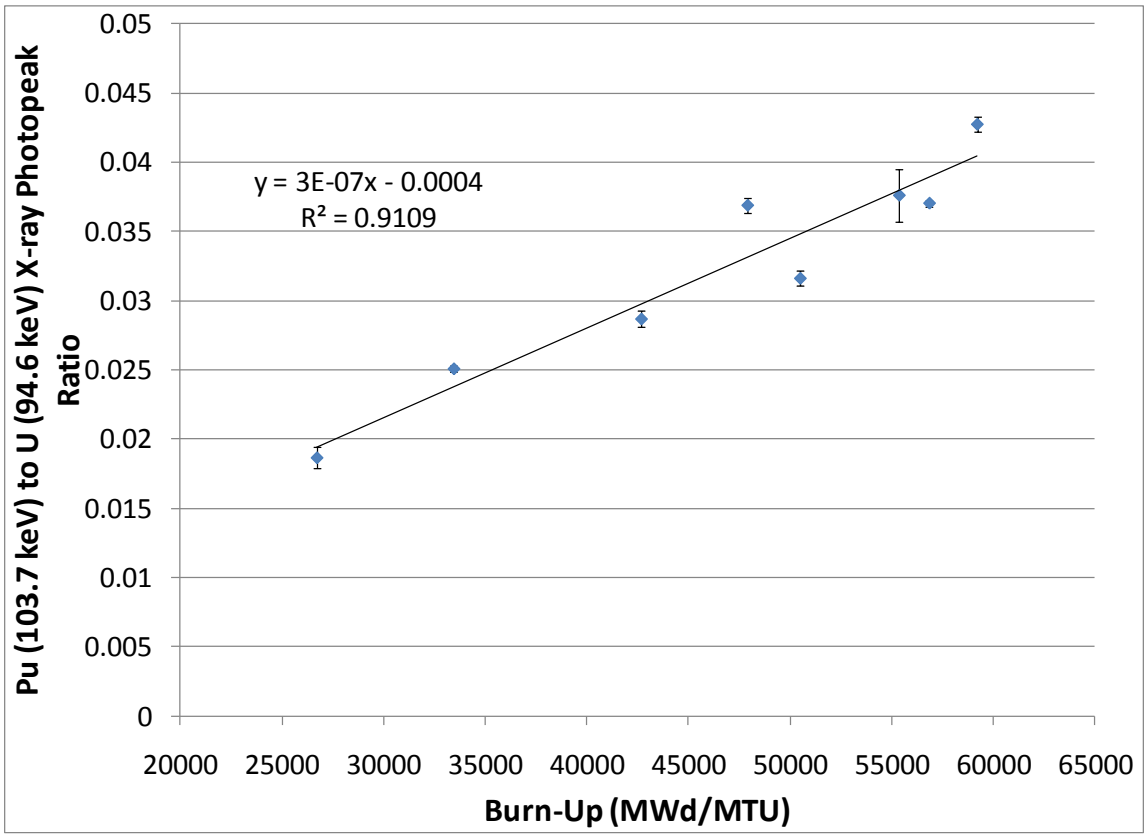

Figure 33. TMI Pu (103.7 keV)/U (94.6 keV) x-ray peak ratio as a function of corresponding burn-up

3.3 Translation to Plutonium Content for the July 2008 Campaign

3.3.1 2D Fuel Pin Simulations

Using the correlated burn-up values, North Anna fuel pin transmutation and depletion simulations were conducted to estimate the Pu/U content of the fuel pin at the specific XRF measurement locations. Assuming the axial profile of the spent fuel over the solid angle of the detector through the collimator is uniform, a two-dimensional fuel pin simulation could be used to estimate the radial distribution of actinides, minor actinides, and fission products. Thus the Pu/U content can be estimated at a specific burn-up.

The modern lattice physics code implemented for the North Anna pin simulations was TransLAT, described in Section 1. Each TransLAT simulation consisted of an infinite cylindrical fuel pin with cladding surrounded by water in an infinite lattice. The build-up and depletion of nuclides was simulated using the operational history and known initial values of the North Anna fuel. Table 15 summarizes the initial input parameters used in all the North Anna simulations. The M5 cladding was assumed to be 100% zirconium because TransLAT does not have niobium in its data library.

Table 15. Summary of TransLAT North Anna parameters

Moderation Average Temperature	578 K
Average Fuel Temperature	854 K
M5 Clad Average Temperature	628 K
Fuel Pellet Radius	0.409575 cm
Clad Thickness	0.057 cm
Outer Radius of clad	0.466575 cm
Fuel Rod Pitch	1.26 cm
Initial Fuel Enrichment U-235	4.199 wt%
Fuel Density	10.44 g/cc
Cycle 1 boron concentration	842 ppm
4-cycle average soluble boron concentration	794 ppm

An average soluble boron concentration of 842 ppm was used for cycle 1, and an average soluble boron concentration of 794 ppm was used for cycles 2 to 4. Boron concentrations for each cycle and the boron let down curve were not provided. However based on previous work by J.C. Wagner, simulations have shown cycle-averaged soluble boron concentrations results in small differences in the ratios of the main fission product and actinide atom densities[30]. Minor differences will exist using a constant boron

concentration in Pu isotopes due to spectral hardening at higher burn-ups[30]. In reality boron concentrations are near zero late in the fuel cycle. For the North Anna simulations, it was assumed the spectral hardening effect would be negligible.

The radial distribution of nuclides was simulated using 20 radial regions in the fuel pin. In Reference 31, the exponential distribution of radial fuel regions was determined through numerical experimentation to be the appropriate choice for simulating a cylindrical pin cell. It was also determined that 20 radial regions accurately characterizes the radial distribution within the limits of the transport solver[31]. In a given cylindrical fuel pin, the fission rate and neutron spectrum vary from the pin surface to the center, and the exponential distribution allows for the attenuation of the low energy neutrons[31]. The exponential radial fuel region distribution is given by

$$r(i) = R_{fo}\left[\frac{1-\exp\left(-\Sigma_a i\right)}{1-\exp\left(-\Sigma_a \mathrm{N_r}\right)}\right] \quad for\ i = 1,2,3\ldots, N_r \tag{13}$$

where Σ_a is a one-group macroscopic absorption cross section, $\mathrm{N_r}$ is the number fuel regions, R_{fo} is the outer fuel radius and i is the fuel region number[31]. The previous research also concluded for most LWR using a one-group absorption cross section value of 0.55 cm^{-1}, an approximation by the U-235 and U-238 thermal absorption cross section values, yielded reasonable distribution results. Since North Anna is a LWR, the 0.55 cm^{-1} value was utilized. A summary of the calculated radii for the North Anna TransLAT simulations using 20 fuel radial regions and Equation (13) are provided in Appendix B. By using fuel regions, TransLAT calculates the average flux and average isotopic concentration over each region[22]. An assumption is built in that the distribution of isotopes is uniform over each region.

Four TransLAT simulations with the correlated burn-up values from the fission product measurements (63,064 MWd/MTU, 66,744 MWd/MTU, 67,021 MWd/MTU and 62,183 MWd/MTU) were executed to estimate the radial distribution of materials. These simulations follow the same initial parameters and operation cycle but have different specific power values resulting in different final burn-up values. A summary of the North Anna TransLAT simulation cases and their corresponding scaling factor, cycle specific power, cycle burn-up and cycle cumulative burn-up values are provided in Appendix B.

3.3.2 Spent Fuel Pin Radial Profiles

The North Anna TransLAT analysis showed the Pu and fission products are biased to the outer edge of the fuel. The analysis also showed as the fuel burn-up increases the Pu and fission product concentrations are biased to the outer fuel region more prominently. Figure 34 and Figure 35 display the Pu density and fission product density as a function of radius at burn-ups of 10 GWd/MTU, 30 GWd/MTU, and 63 GWd/MTU. Main Pu production on the fuel edge is expected in a thermal reactor, because neutrons created in the fuel have a high probability of being absorbed in U-238 entering a fuel pin at lower energies from slowing down in the moderator. The radial distribution of Pu is favorable because the XRF measured is from the outer edge layer (~300 μm)[11] of the spent fuel. Since the fission product distribution is biased to the outer edge of the fuel, the gamma-rays and beta particles from fission product decay emissions may induce more XRF in the Pu edge. In reality the fission products, Pu, and U will migrate in the fuel and possibly into the fuel cladding.

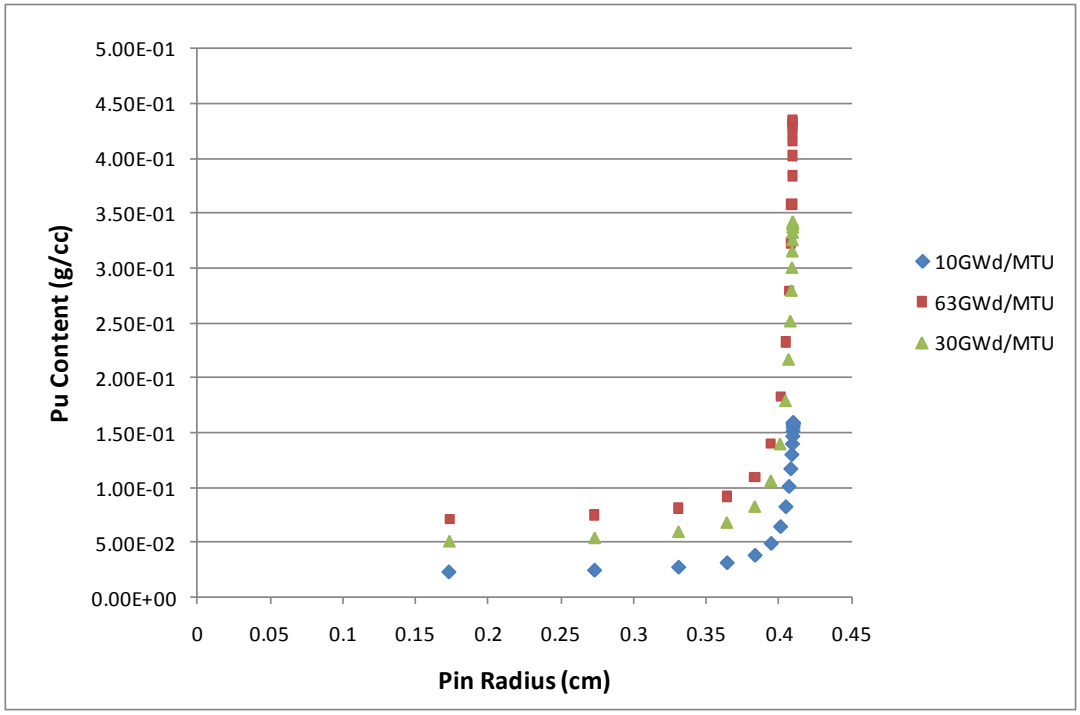

Figure 34. Radial Pu content distribution 649A North Anna case

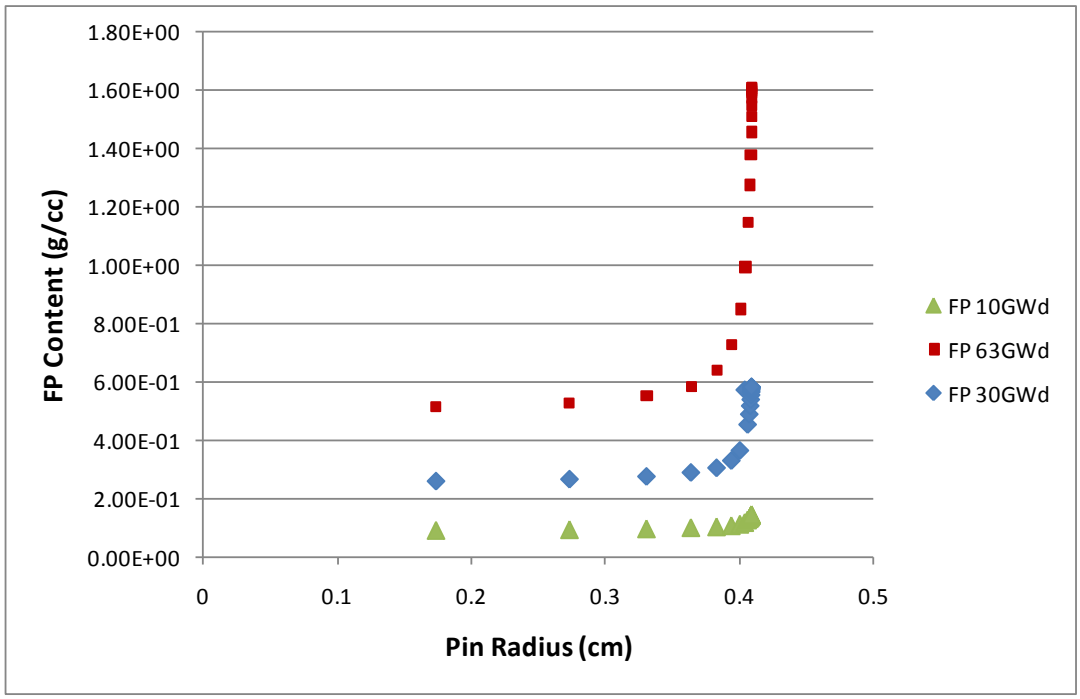

Figure 35. Fission product radial distribution 649A North Anna case

Figure 36 and Figure 37 display the Pu density and fission product density as a function of radius at the North Anna 649 rod correlated burn-ups, respectively. Since the final burn-up values are close in range (62-67 GWd/MTU), the Pu concentration distributions look almost equal. The fission product distribution does show distinctly lower values for the 649G case at ~62GWd/MTU.

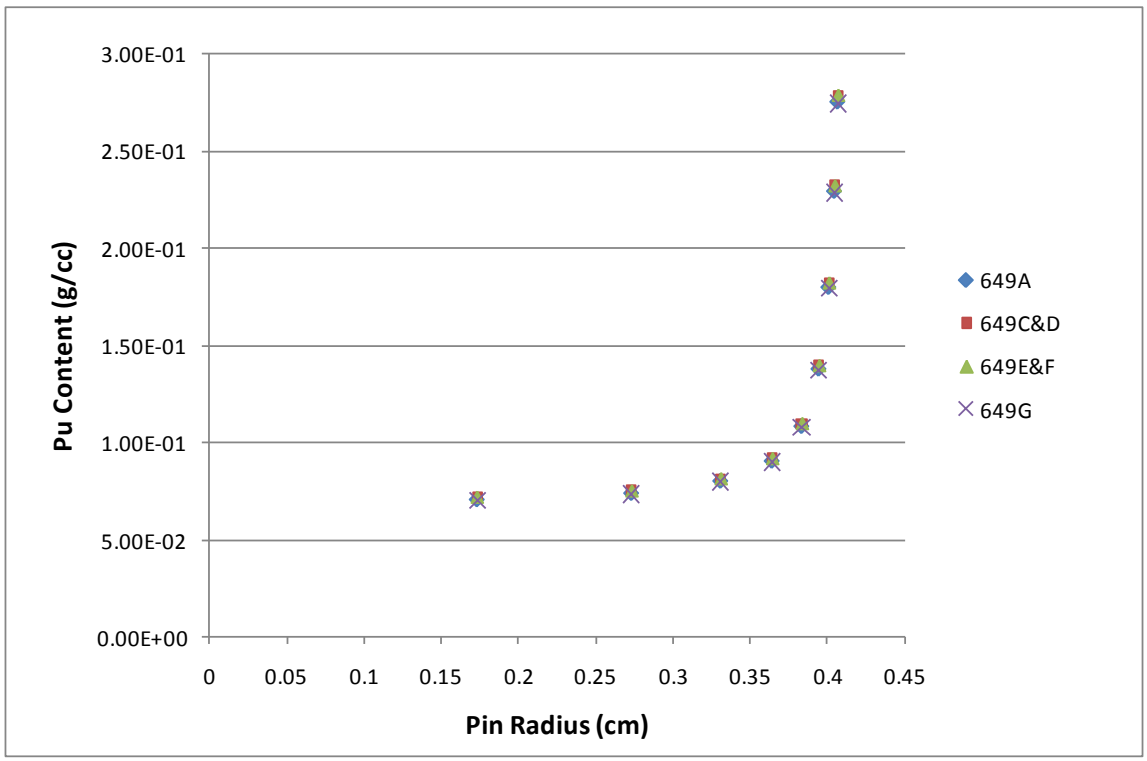

Figure 36. North Anna Pu radial distributions

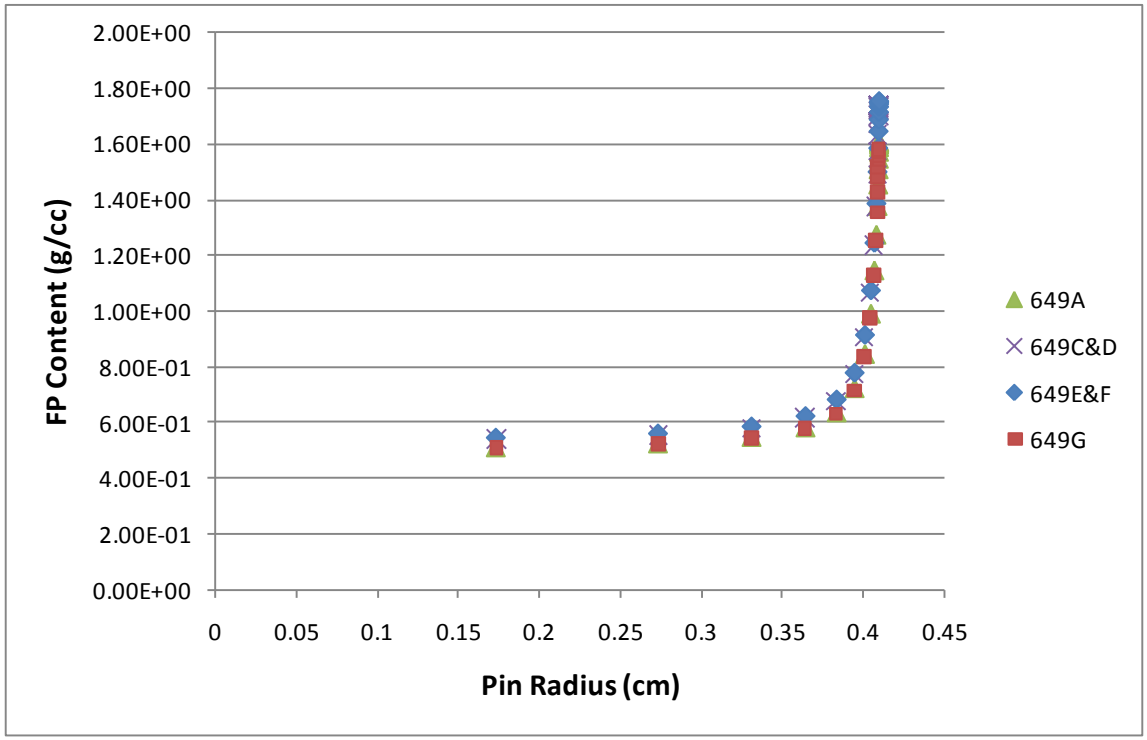

Figure 37. North Anna fission product radial distribution

3.3.3 Correlation Results

Using the known Cs-134/Cs-137 activity ratios, the Pu/U photopeak ratios, and the TransLAT correlated simulations, the Pu/U photopeak ratios can be correlated to an estimated Pu/U content at the North Anna XRF measurement locations. Figure 38 shows the TransLAT calculated Pu/U content ratio for the corresponding fuel pin XRF measurements as a function of Cs-134/Cs-137 content ratio.

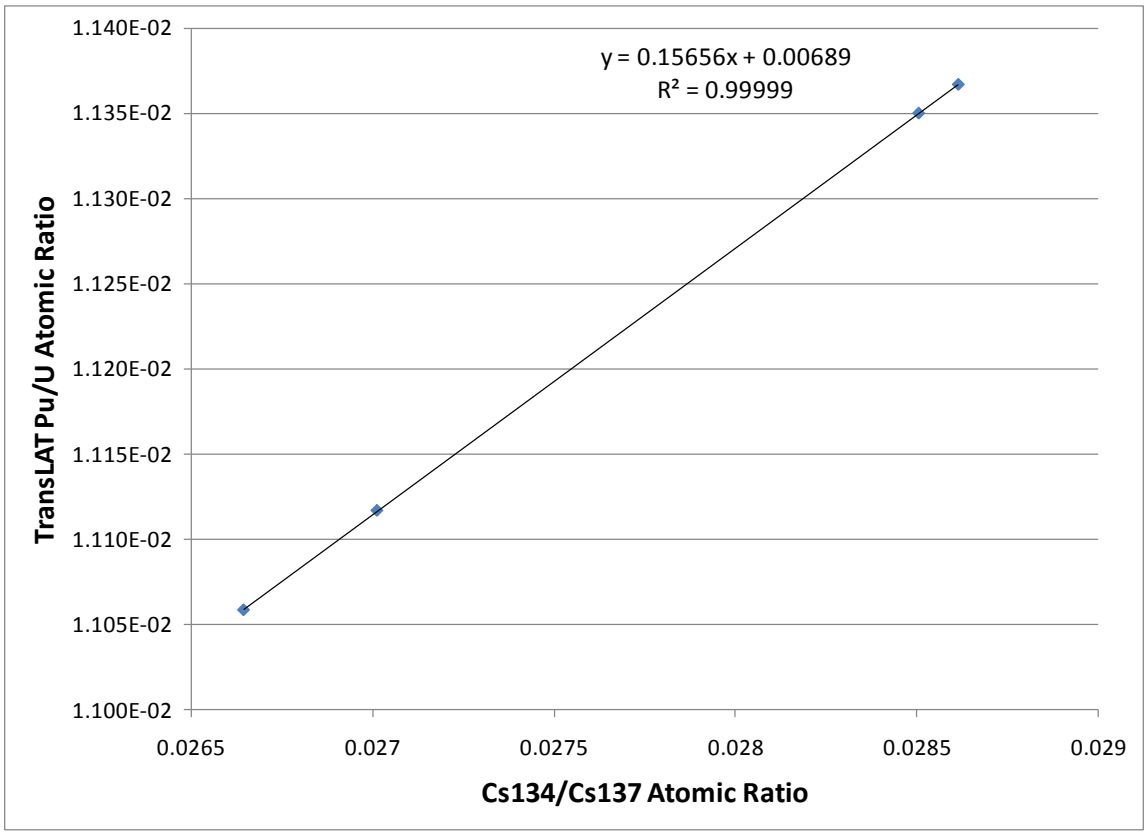

Figure 38. TransLAT calculated North Anna Pu/U ratio versus Cs-134/Cs-137

Once the relationship between the pin Pu/U and Cs-134/Cs-137 content ratios were established, the measured Cs-134/Cs-137 activity ratios can be converted to Cs-134/Cs-137 concentration ratios and translated to corresponding Pu/U content ratios. The measured North Anna activity ratios from Table 10 were converted to content ratios and fit to the linear trend in Figure 38, establishing the corresponding Pu/U content ratio at the XRF measurement locations. The measured Pu/U photopeak ratio as a function of Pu/U content for the North Anna measurements is shown in Figure 39 including uncertainties.

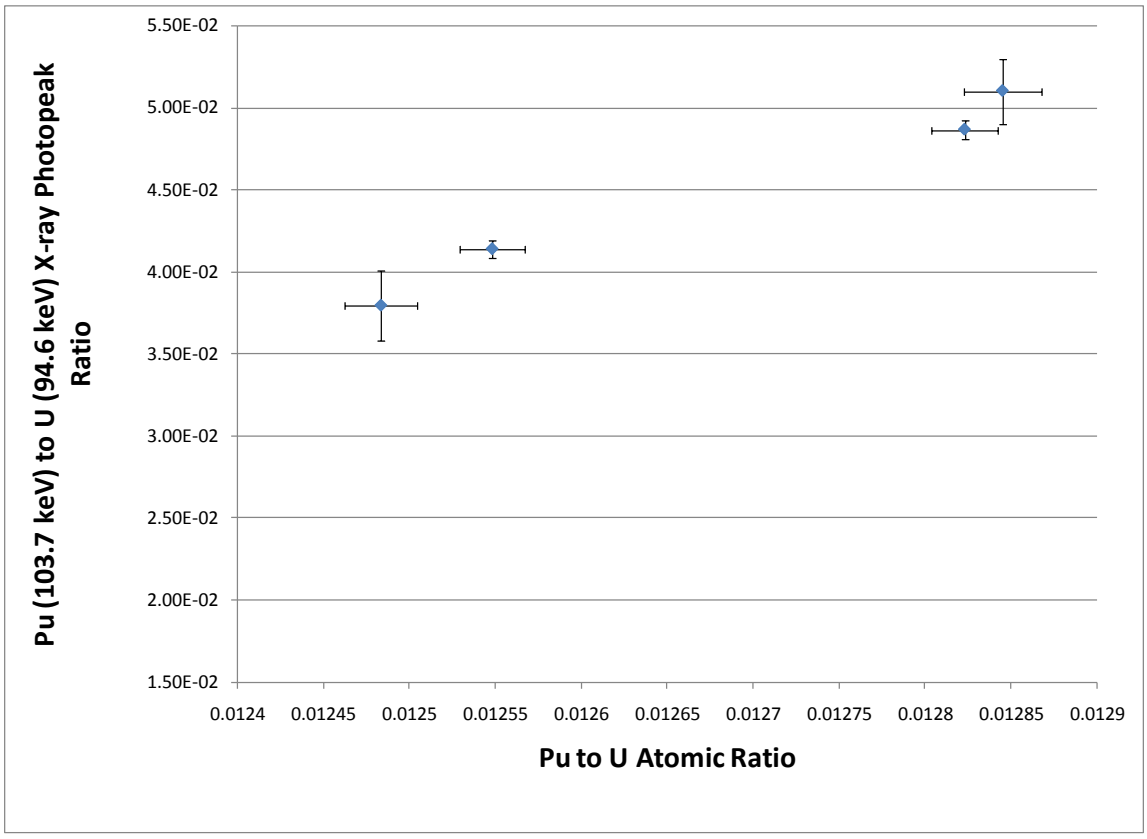

Figure 39. North Anna Pu/U peak ratio versus Pu/U TransLAT calculated content ratio

3.4 Translation to Plutonium Content for the January 2009 Campaign

3.4.1 2D Fuel Pin Simulations

Similar to the North Anna TransLAT simulations, two-dimensional fuel pin TMI simulations were conducted to estimate the radial profile of actinide, minor actinide and fission product content. Using the correlated burn-up values at the XRF measurement locations and the operational history, TMI fuel pin transmutation and depletion simulations were performed to estimate the radial distribution of Pu/U content. Each TransLAT simulation consisted of an infinite cylindrical fuel pin with cladding

surrounded by water in an infinite lattice. Table 16 summarizes the initial input parameters used in all the TMI TransLAT simulations.

Table 16. Summary of TransLAT TMI parameters[29]

Moderation Average Temperature	578 K
Zry-4 Clad Average Temperature	628 K
Fuel Pellet Radius	0.4681 cm
Clad Thickness	0.069 cm
Outer Radius of clad	0.5371 cm
Fuel Rod Pitch	1.303 cm
Initial Fuel Enrichment	4.0 wt%
Fuel Density	10.412 g/cc

Soluble boron concentrations measured at intervals of operation were provided. The measured boron concentrations were plotted and showed the boron let down curves were fairly linear. For the simulations, intermediate boron concentrations were calculated using linear interpolation between the measured values. The measured and calculated soluble boron concentrations used in the TransLAT simulations are included in Appendix D. The radial distribution of nuclides was simulated by using 20 radial regions in the fuel pin. The radii were calculated using Equation (13) and are summarized in Appendix D. TransLAT simulations were ran using the same operational cycle but with different average fuel temperatures and specific power values resulting in different final burn-up values.

Eight simulations using the correlated burn-up values from the fission product measurements were executed to estimate the radial distribution of materials. Calculating the specific power for the TMI simulations was more complex than the North Anna simulations. Burn-up cycle values and temperatures were provided for the H6 rod at

different axial locations. This rod was in the same assembly as the D5 rod measured. The cycle burn-up at the closest correlating location to the XRF measurement location was used to calculate the specific power and provide the average fuel temperatures. The H6 burn-up, calculated specific power, and average fuel temperature values for the correlating closest locations to the XRF measurement location in D5 are provided in Appendix D. The H6 cycle specific powers were then scaled to calculate the desired burn-up value for the simulation. The scaled burn-up values are provided in Appendix D for each TMI TransLAT simulation.

3.4.2 Boron Crud Simulations

The D5 TMI spent fuel rod originated from a fuel assembly with substantial boron crud build-up; therefore, a preliminary boron crud sensitivity study using TransLAT was performed to investigate the effect of the boron crud on the nuclide radial distribution. For model simplicity, the boron crud build-up was modeled as a uniform boron layer outside the fuel cladding with varying thicknesses of 1E-2, 1E-3, 1E-4, and 1E-5 cm. These cases were compared to a base case in which there is no boron lining. Each case used the power history of the TMI fuel with an averaged specific power for each cycle. The results are shown in Figure 40 and Figure 41 using the fuel pin average values from TransLAT. Figure 40 shows the relationship between Cs-134 to Cs-137 atomic ratio and fuel burn-up. As the boron lining thickness increases, the Cs-134 to Cs-137 atomic ratio shifts to a higher value. However, the difference between the base case and the 1E-5 cm and 1E-4 cm boron thickness cases are negligible.

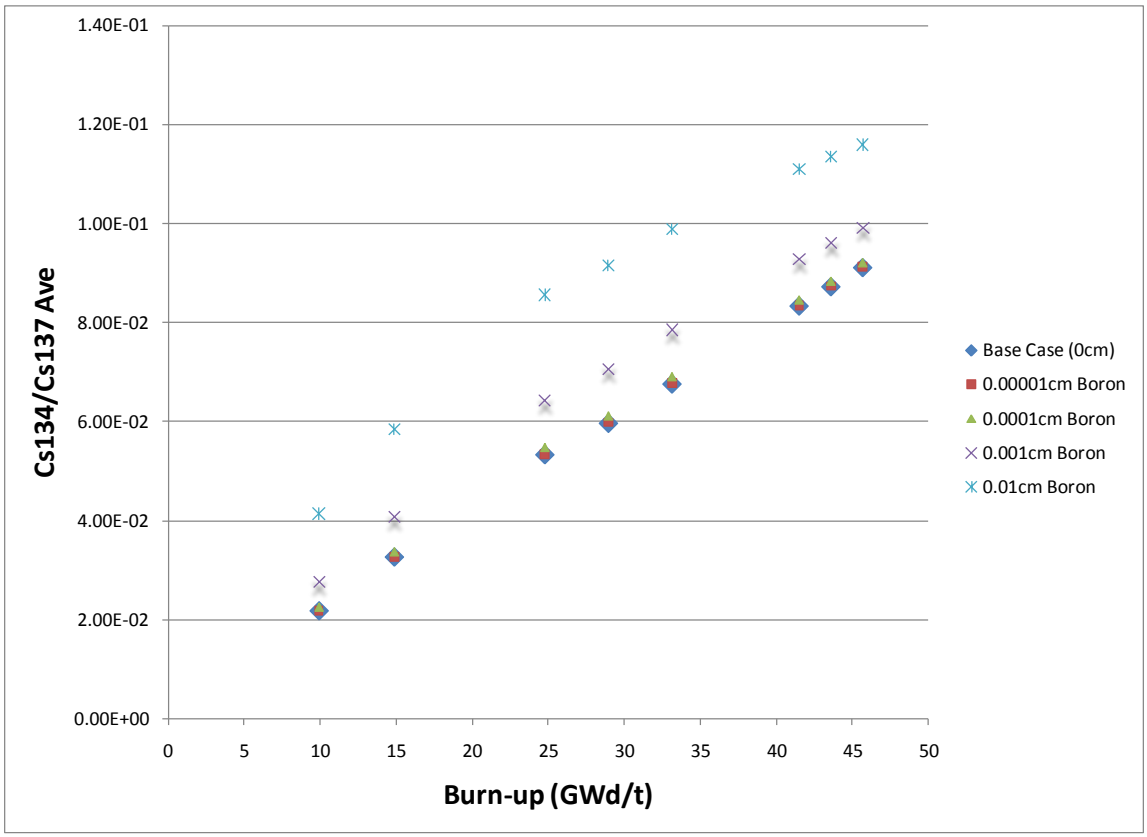

Figure 40. Boron results Cs-134 to Cs-137 atomic concentration ratio versus fuel burn-up

Figure 41 shows the atomic concentration of Pu as a function of burn-up for the different boron cases. Again, the difference between the base case and the 1E-5 cm and 1E-4 cm boron thickness cases are negligible. For the remaining cases, the Pu atomic concentration versus burn-up curve steepens as the boron thickness increases, showing the Pu atomic concentration increasing dramatically in comparison to the base case.

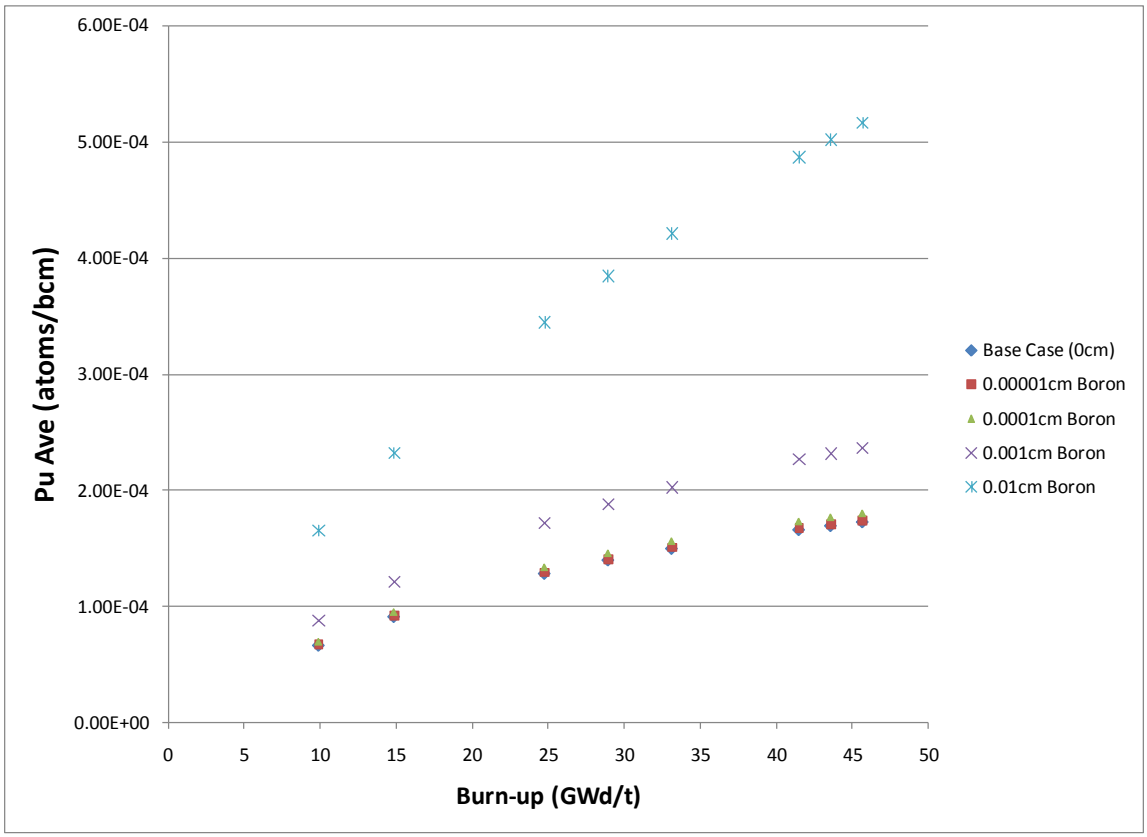

Figure 41. Boron results fuel pin averaged Pu atomic concentration versus fuel burn-up

The boron sensitivity study provided valuable information on the effects of the boron layer on the Pu content and the Cs-134 to Cs-137 ratio. Only the extreme boron thicknesses cases showed significant differences from the base case. In reality boron crud build-up occurs in localized locations; therefore, this sensitive study was inherently conservative. Analysis of the more realistic cases, 1E-5 cm and 1E-4 cm, showed the boron layer has a negligible effect on the nuclide radial distribution. Therefore it was assumed the boron crud build-up was negligible and would not be considered in the TransLAT TMI simulations.

3.4.3 Spent Fuel Pin Radial Profiles

The TMI simulations demonstrated radial nuclide distributions with the same behavior as the North Anna simulations. Figure 42 and Figure **43** display the Pu density and fission product density as a function of radius at the TMI D5 rod correltated burn-ups, respectively. Since the final burn-up values range from 27 to 59 GWd/MTU, the Pu and fission product concentration distributions have more variation than the North Anna TransLAT simulations.

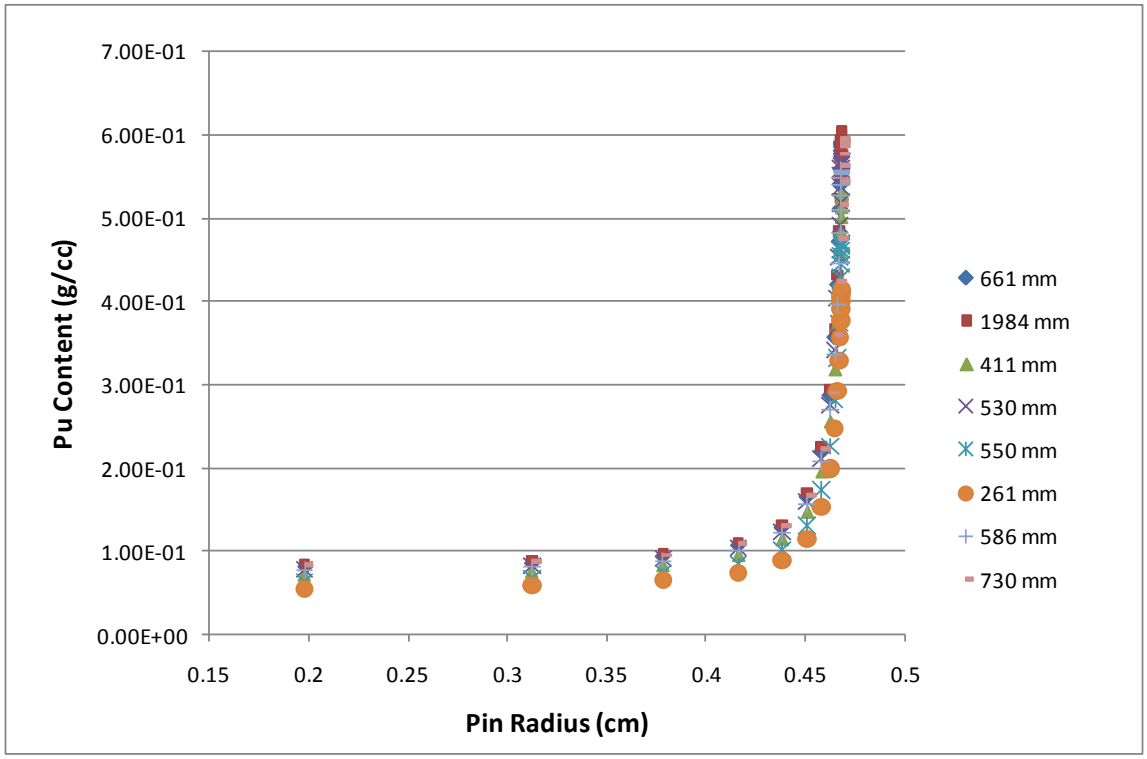

Figure 42. TransLAT TMI Pu radial distribution

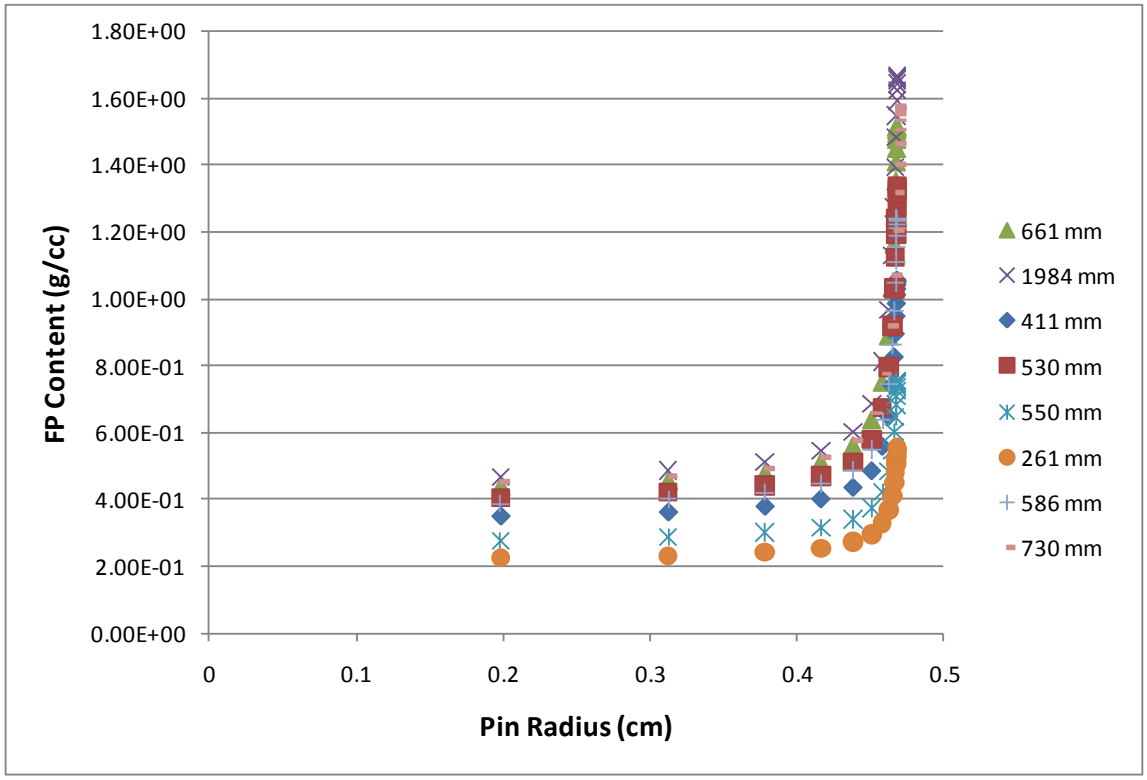

Figure 43. TransLAT TMI fission product radial distribution

3.4.4 Correlation Results

Using the known Cs-134/Cs-137 activity ratios, the Pu/U photopeak ratios, and the TransLAT correlated simulations, the Pu/U photopeak ratios were correlated to an estimated Pu/U content at the TMI XRF measurement locations. In the same manner as the North Anna TransLAT analysis, the TransLAT calculated Pu/U content ratio for the fuel pin for the corresponding XRF measurements was plotted as a function of Cs-134/Cs-137 content ratio, shown in Figure 44. The TMI relationship between Pu/U and Cs-134/Cs-137 is very different from the North Anna relationship due to the varying fuel

ages. The TransLAT predicted Cs-134/Cs-137 content ratio for the TMI spent fuel is much lower from the decay of Cs-134 (2.0648 year half-life).

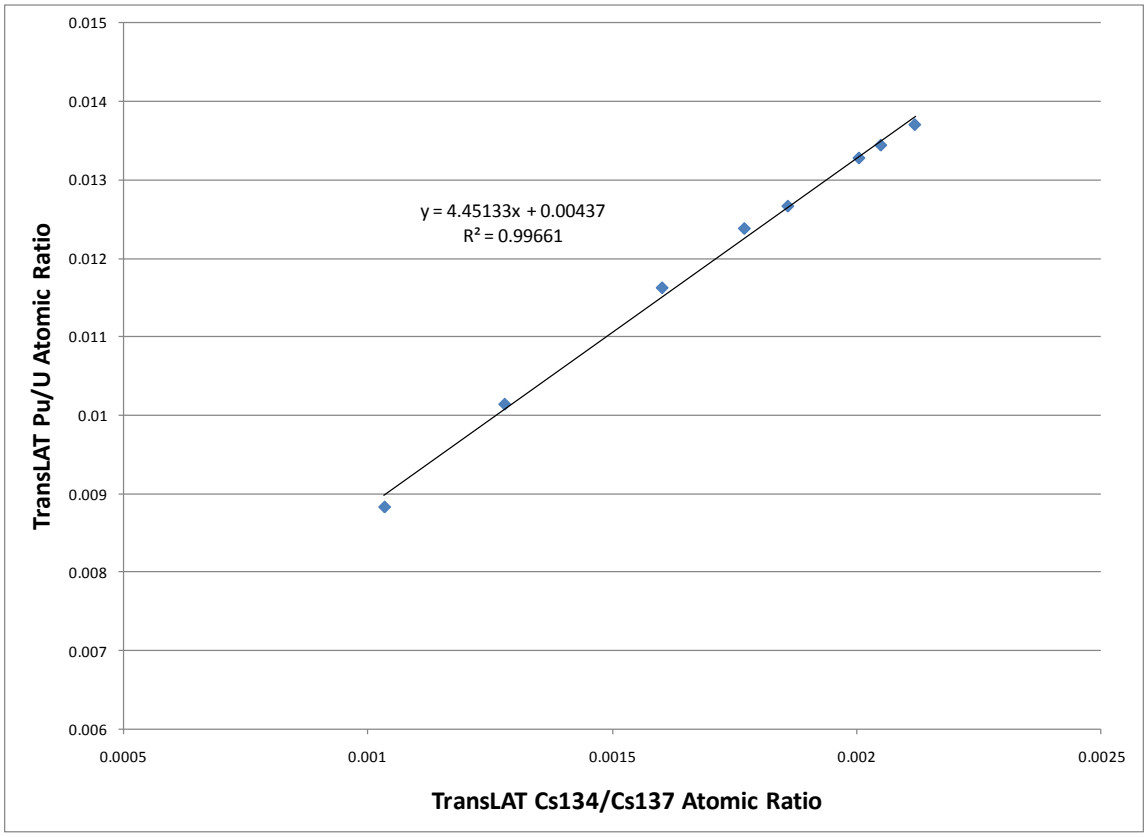

Figure 44. TMI TransLAT Pu/U ratio as a function of Cs-134/Cs-137

Once the relationship between the fuel pin Pu/U and Cs-134/Cs-137 content ratios was established, the measured Cs-134/Cs-137 activity ratios were converted to Cs-134/Cs-137 concentration ratios and translated to corresponding Pu/U content ratios. The measured Pu/U photopeak ratio as a function of Pu/U content for the TMI measurements is shown in Figure 45 including uncertainties. Figure 45 shows the Pu/U peak ratio has a direct linear relationship to Pu/U content. This relationship can be calibrated using destructive analysis of the TMI spent fuel rod at the measurement locations. Once this

relationship is calibrated, it can be used to determine the Pu/U content of the current fuel.

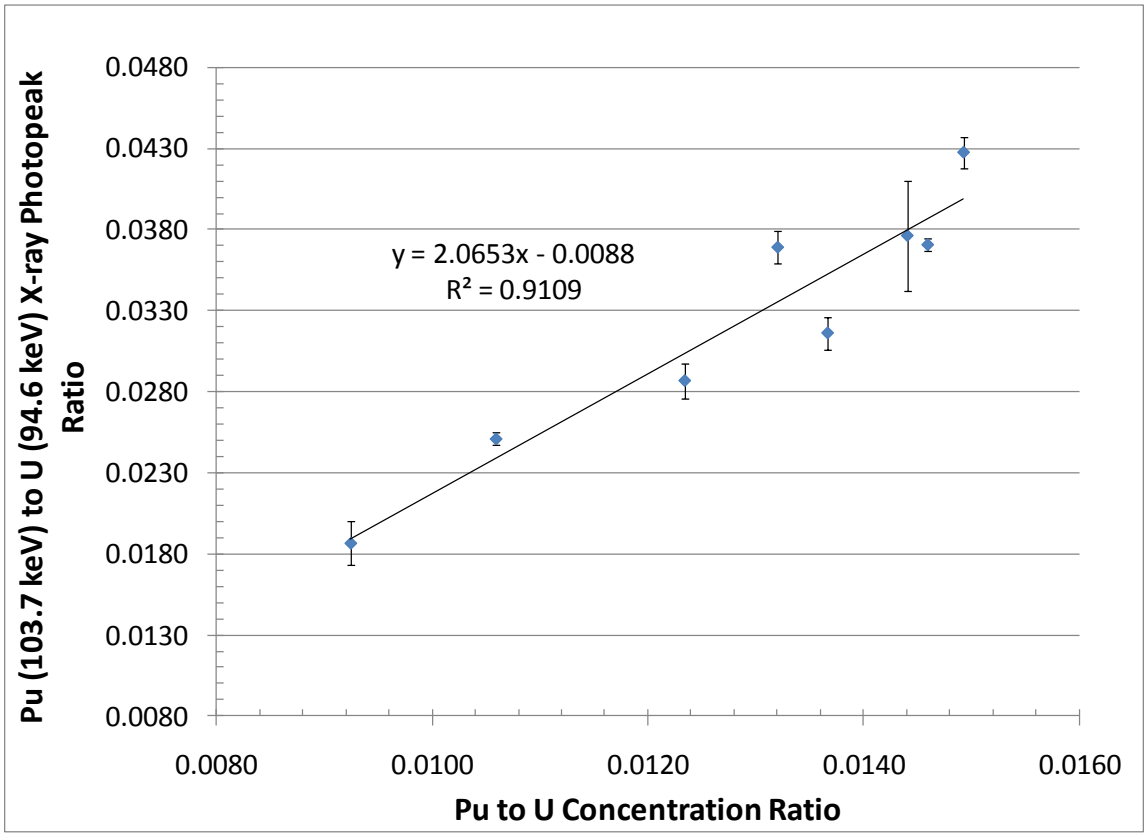

Figure 45. TMI measured Pu/U peak ratio versus TransLAT calculated Pu/U content ratio

4. UNDERSTANDING THE PHYSICS OF XRF MEASUREMENTS FOR SPENT FUEL

This section investigates the spent fuel experiments to further understand the physics of the XRF measurements through radiation transport simulations. We present the sources of measurable radiation in the spent fuel experiments and the investigation of the photon and beta source contributions to the creation of XRF in the spent fuel using MCNP5. Also MCNP5 fuel pin and detector simulations of the experiments are presented to explain the contributions of noise to the detector.

4.1 Sources of Measureable Radiation

In the XRF experiments, there are several sources of measurable radiation by the HPGe detector. There are measurable gamma and x-rays from the fuel, cladding, shipping tube, collimator, surrounding shielding and the detector. The sources born in the fuel include: (1) gamma-rays from fission products, (2) x-rays from actinides induced by gamma or beta radiation, (3) Compton from fission product gamma-rays, and (4) bremsstrahlung from fission product beta decay. The HPGe detector measures these sources from the fuel and the resulting Compton and backscatter interactions. The Compton is produced by fission product gamma rays, Compton gamma-rays, bremsstrahlung gamma-rays, and x-rays (induced by beta and gamma-rays in fuel) interacting in the collimator, cladding, shipping tube, detector, detector can, etc. The measurable backscatter is a result of fission product gamma-rays, Compton gamma-rays, and bremsstrahlung gamma-rays interacting in the shielding materials. Compton and backscatter can adversely affect the signal-to-noise ratio.

For model simplification and reducing computer run-times, it is desired to assume only photon sources contribute significantly to the measured spent fuel spectra. By assuming only photons, bremsstrahlung from the fuel, beta induced x-rays, Compton from bremsstrahlung and beta induced x-rays, and backscatter from bremsstrahlung will not be accounted for in the simulations. The following section compares the gamma-ray spectra from the fuel for photon and beta sources to determine if the assumption of only sources from photons is valid.

4.2 Investigating the Photon and Beta Source Term

The initial spent fuel detector system simulations brought to attention the question of how the different XRF sources in spent fuel are contributing to the measured spectra and if the assumption of using only photon sources is valid. This study investigates the results of MCNP5 transport calculations of XRF from gamma-ray and beta decay of fission product and actinide isotopes. Two cases were considered, the North Anna spent fuel with a correlated burn-up of 63.064 GWd/MTU (case 649A) and TMI fuel at a correlated 56.857 GWd/MTU burn-up (case 730mm). The previously calculated isotopic contents from TransLAT were used to calculate the fission product gamma and beta source strengths in MCNP5. This study involved simulating a cylindrical spent fuel pin with a surrounding cylindrical HPGe detector, to ensure all gamma-rays and x-rays escaping the fuel were captured. Simulations were performed using the calculated beta source or gamma source. The source term calculations and simulated results are presented.

4.2.1 Derivation of Photon Source Strength

The TransLAT calculated isotopic concentrations for the North Anna and TMI spent fuel cases were utilized to create a photon source input for the MCNP simulations. This section provides a derivation of the photon source strength for the individual gamma lines from the decay of fission product and actinide isotopes for a particular radial region.

Assume the photon source will be calculated for a cylindrical spent fuel pin with several concentric radial regions. The radial regions have uniform isotopic concentrations within each region, and the photon source is uniform within each region emitting isotropically. The spent fuel contains several known nuclides and the corresponding isotopic concentrations, which emit gamma-rays from radioactive decay. Assume the problem is time independent; therefore, the isotopic concentrations are constant. Each photon emitting isotope has an activity given by

$$A_{Xr} = N_{Xr}\lambda_X \tag{14}$$

where A_{Xr} is the activity of isotope X in region r, N_{Xr} is the isotopic concentration in region r, and λ_X is the decay constant for the isotope. Each isotope emits one or more photons at characteristic energies; thus, the activity from particular gamma-ray energy from the decay of isotope X is given by

$$A_{Xri} = N_{Xr}\lambda_X Y_{Xi} \tag{15}$$

where Y_{Xi} is the yield of the gamma-ray at energy i. In MCNP5 the source strength is entered as a probability of emission of a particular gamma line, and the gamma lines are automatically normalized to one. Therefore, the calculated activities, which are

proportional to the probability of emission, were used in MCNP5. N_{Xr} was taken directly from the specific TransLAT simulation for the 20 radial regions, and Y_{Xi} and λ_X values were provided from nuclear data tables. Since the sources are normalized to one in each region, a regional probability distribution, equal to the total region source normalized to the total fuel pin source, was used to account for the radial source distribution.

4.2.2 Derivation of Multi-group Beta Source Spectrum

The TransLAT calculated isotopic concentrations for the North Anna and TMI spent fuel cases were also utilized to create a multi-energy-group beta spectrum for the MCNP simulations. This section provides the derivation of the multi-group beta source from the decay of fission product and actinide isotopes for a particular radial region.

Assume the beta source will be calculated for a cylindrical spent fuel pin with several concentric radial regions. The radial regions have uniform isotopic concentrations within each region, and the beta source is uniform within each region emitting isotropically. The spent fuel contains several known nuclides and the corresponding isotopic concentrations, that emit betas from radioactive decay. Assume the problem is time independent; therefore, the isotopic concentrations are constant. Each isotope emits one or more betas with characteristic continuous beta energy spectra. An individual beta spectrum can be approximated by

$$\int_0^E I_x(e)de \cong \sum_0^G I_{xg}\Delta e_g \qquad (16)$$

where $I_x(e)$ is the intensity of the beta at energy e for isotope x, E is the maximum beta spectrum energy, I_{xg} is the intensity for a energy group, Δe_g is the energy increment for

a particular energy group, and G is the last energy group. The beta intensity for energy group g for all isotopes and all beta emissions inside region r is given by

$$I_{gr} = \sum_{x=1}^{X} \sum_{i=1}^{I} N_{xr} \lambda_x Y_i I_{xig} \tag{17}$$

where I_{gr} is the intensity for region r for energy group g for all isotopes and beta emissions. The beta spectrum intensities for each isotope were provided by Reference 32. These intensity values were for 10E6 beta decays of the isotope discretized in 1 keV energy increments. These intensity spectrum values already account for the beta yields.

The beta spectrum with 1 keV energy bins were combined into larger energy groups to satisfy the input limits of MCNP5. The energy bins were combined using Equation (18),

$$\bar{I}_{Gr} = \frac{\sum_{g=g1}^{g2} \left(\sum_{x=1}^{X} \sum_{i=1}^{I} N_{xr} \lambda_x Y_i I_{xig} \right) \Delta e_g}{\sum_{g=g1}^{g2} \Delta e_g} \tag{18}$$

where g_1 and g_2 are the first and last energy groups in the new combined energy group, Δe_g is the energy bin size for group g, and $\bar{I}_{Gr}$ is the intensity for the new combined energy group for region r. The fission product beta source term was approximated by a 317 multi-group beta spectrum comprised of the individual isotopic beta spectra ranging from 0 MeV to 3.17 MeV (maximum beta energy from individual spectra) for each region. As with the photon source, a regional probability distribution was used. The beta created spectrum accounted for the beta decay of 100 fission product and actinide isotopes, including the strongest fission product beta sources.

4.2.3 Photon and Beta Source Comparison

To compare the photon and beta induced XRF, MCNP5 simulations of a simplified fuel pin model were implemented. This model consisted of a cylindrical spent fuel pin with 20 radial regions, fuel cladding, the shipping tube, and a surrounding cylindrical HPGe detector with a crystal thickness of 1.5cm (same as XRF experiments), within a vacuum region. The spent fuel pin was 4 cm long, and the source uniformly extended the entire fuel pin. Figure 46 shows an x-y plane and x-z plane of the North Anna fuel pin simulations.

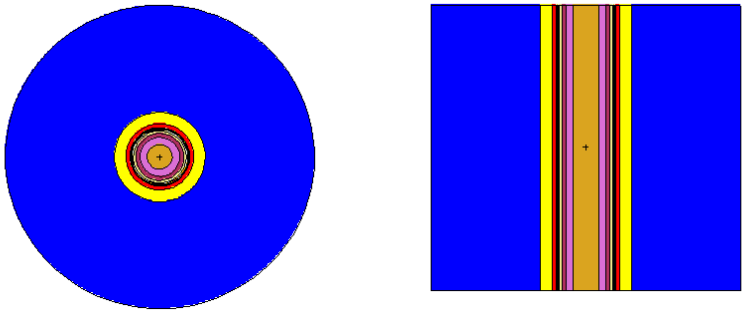

Figure 46. North Anna simplified pin model geometry, (left) x-y plane and (right) z-x plane

The North Anna and TMI spent fuel pin simulations used the TransLAT created isotopics for the different fuel regions and used the appropriate fuel pin geometries. The North Anna fuel pin had an outer fuel radius of 0.409575 cm, a M5 cladding thickness of 0.057 cm and a stainless steel shipping tube thickness of 0.0625 cm. The TMI spent fuel pin had an outer radius of 0.4681 cm, a Zirchaloy-4 cladding thickness of 0.069 cm and a stainless steel shipping tube thickness of 0.0625 cm. North Anna 649A case at 63.064 GWd/MTU (4.2 year old fuel) and TMI fuel case 730mm at 56.857 GWd/MTU (13.3

year old fuel) were used. The simulated spectra were analyzed using Genie 2000 software to calculate the net peak area and uncertainties for the peaks of interest.

Using the photon created source for each case, MCNP5 photon simulations were executed for 1E8 histories. The resulting photon spectra had uncertainties of 1-2%. Then simulations were conducted using the multi-group beta spectrum source. For the North Anna case three beta source simulations were conducted accounting for x-rays, bremsstrahlung, and Compton: created in the fuel only, created in the fuel and cladding, and created in the fuel, cladding, and shipping tube. These source differences were accomplished by changing the electron importances in the geometric cells in MCNP5. The beta source induced gamma-ray spectra in the x-ray energy region had 4-5% uncertainties.

The North Anna beta simulations showed by including the beta interactions in the cladding with the fuel, the beta induced spent fuel XRF was accounted for more completely. Figure 47 shows the results of the three North Anna beta simulations in the x-ray energy region. The fuel and clad simulation shows increased peak values and continuum significantly compared to the fuel only simulation. The increase in the U XRF peaks is larger than the increase in the Compton continuum. By also including the shipping tube, the peaks and continuum increase proportionally. Figure 47 also shows the two main contributors of Compton background originate from the fuel and the fuel cladding. In consequence of these beta source results, the TMI simplified beta source simulations considered the x-rays, bremsstrahlung, and Compton created in the fuel, cladding, and shipping tube.

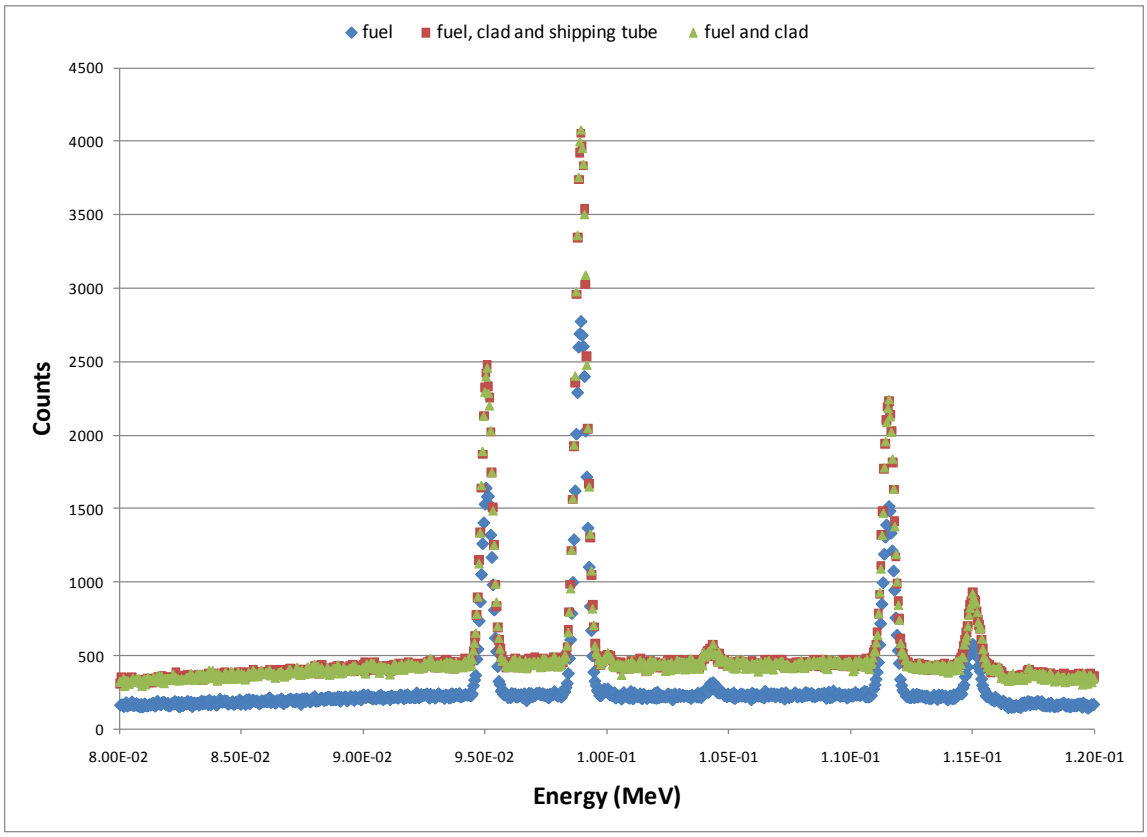

Figure 47. North Anna simplified pin model with beta induced gamma spectrum

Figure 48 displays the North Anna photon source results, beta source results, and a combination of the photon and beta source results. The peak at 105.3 keV and 86 keV are fission product gamma-rays and in consequence are not visible in the beta induced spectrum. The beta source induced gamma-ray spectrum was scaled by 2.4 to account for the differences in the initial photon and beta source strengths. Figure 48 shows the gamma-ray spectrum from the beta source is much lower than from the photon source. Observing the 98.4 keV U x-ray peak, the photon source contributes 86.14% +/- 4.96% to the peak, while the beta source contributes 13.86% +/- 1.48%. Therefore for LWR spent fuel at ~4.2 years old at nominal 67 GWd/MTU burn-ups, the photon source

contributes more to the XRF production than the beta source. Unfortunately the Pu x-ray peak at 103.7 keV is indistinguishable in the beta induced spectrum because it is buried in the background.

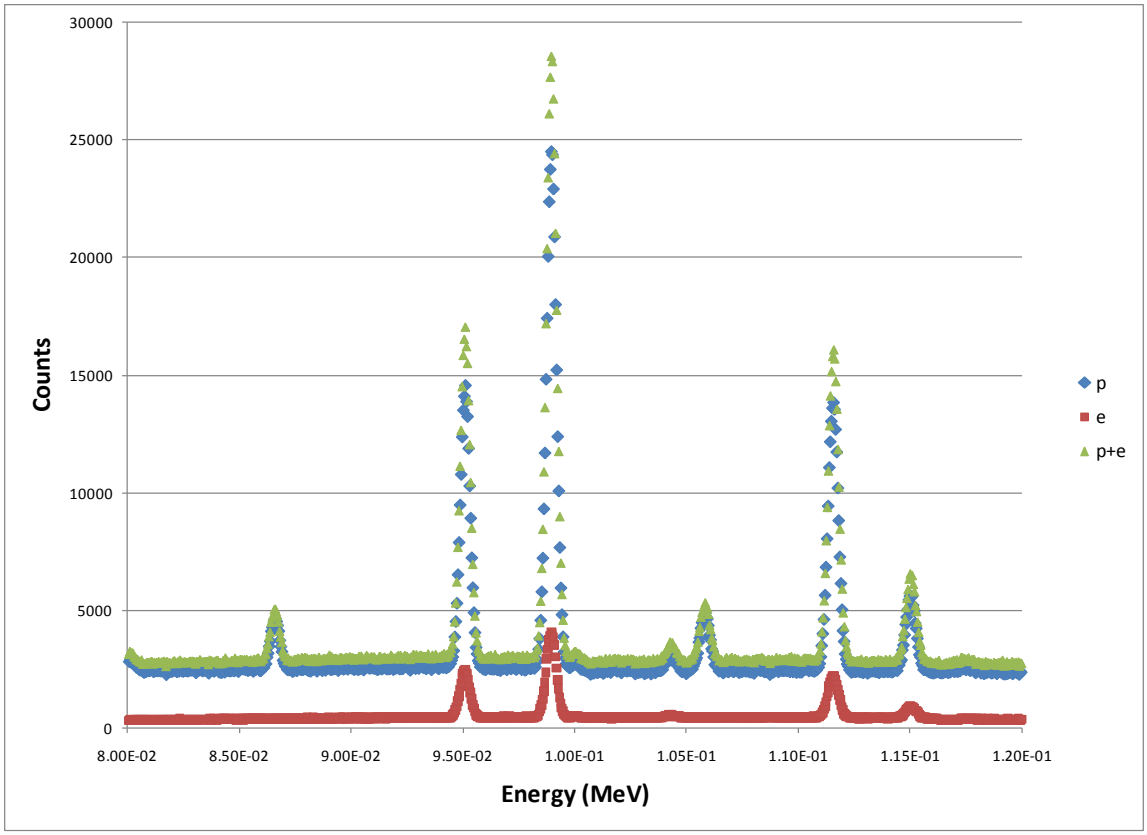

Figure 48. North Anna simplified model beta and gamma-ray induced spectrum comparison

Figure 49 displays the TMI photon source results, beta source results, and a combination of the photon and beta source results. The beta source induced gamma-ray spectrum was scaled by 3.55 to account for the differences in the initial photon and beta source strengths. Figure 49 shows a similar pattern to the North Anna results. For the TMI case, the photon source contributes 86.7% +/- 4.53%, and the beta source contributes 13.2% +/- 1.5% to the 98.4 keV U x-ray peak. Therefore for LWR spent fuel

at ~13.3 years old at nominal 50 GWd/MTU burn-ups, the photon source contributes more to the XRF production than the beta source. Again, the Pu x-ray peak at 103.7 keV was hidden in the noise.

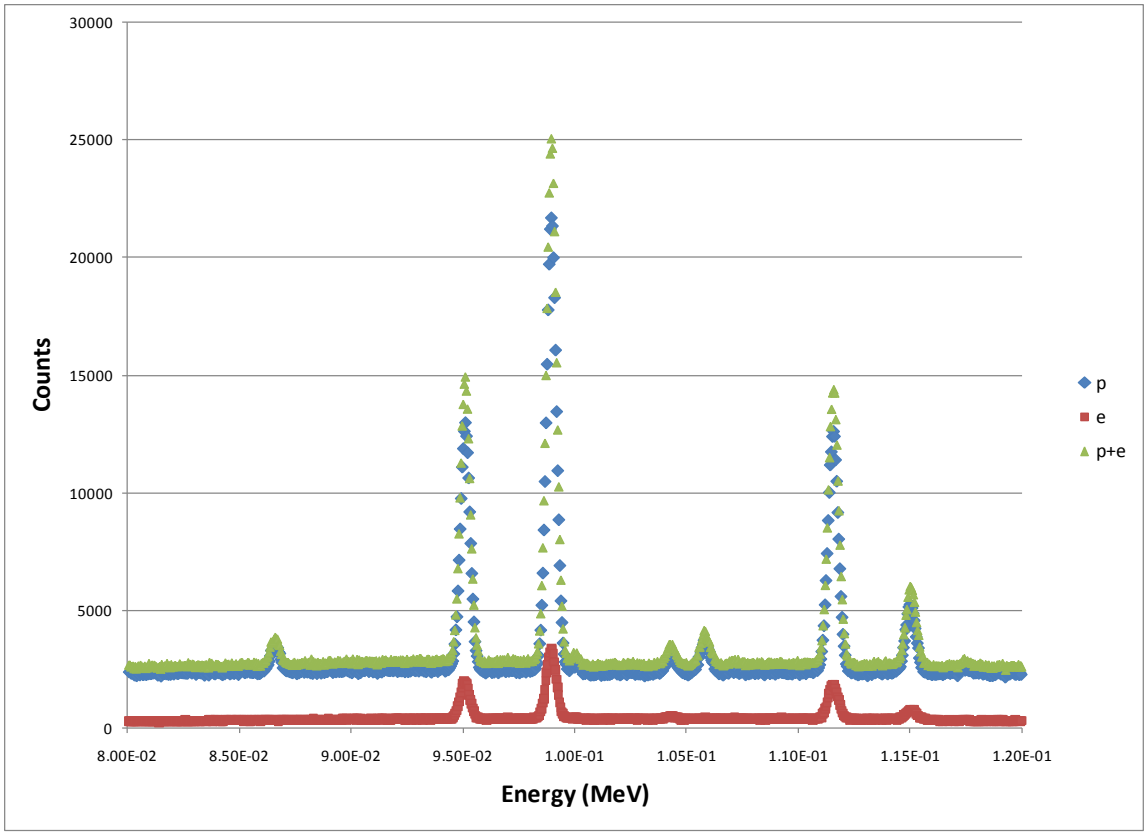

Figure 49. TMI simplified model beta and gamma-ray induced spectrum comparison

The ratio of the Pu and U x-rays to the background was also observed to establish the relationship between the signal-to-noise ratio for the beta and photon source problems. The integral background counts were taken from 101.3 keV to 102.4 keV between the Pu and U x-ray peaks of interest. For the North Anna simulations, the U to background ratios and Pu to background ratios were 3.60 +/- 0.33 and 0.09 +/- 0.01 for the beta source problem and 3.92 +/- 0.08 and 0.11 +/- 0.01 for the photon source

problem respectively. For the TMI simulations, the U to background ratios and Pu to background ratios were 3.79 +/- 0.38 and 0.16 +/- 0.02 for the beta source problem and 4.08 +/- 0.08 and 0.14 +/- 0.01 for the photon source problem respectively. In both cases, the U to background and Pu to background ratios were in good agreement within uncertainties. Since the ratios were in good agreement it was assumed the signal-to-noise ratio is directly proportional to the source activity, and for the simplified pin case, the photon source does not underestimate the background.

The XRF source term study showed for 4.2 year to 13.3 year old fuel ranging from ~50 GWd/MTU to ~67 GWd/MTU burn-up the photon source contributes approximately 86% and the beta source contributes approximately 14% to x-rays. Also for additional simulations it can be assumed the photon only problem can be used to model XRF stimulation, the photon problem will not underestimate the background, and the signal-to-noise ratio is directly proportional to activity.

4.2.4 Simple Pin Model Photon Spectra and Measured Spectra Comparison

Additional simulations using the simple pin model were conducted to compare to the measured XRF spectra. These simulations only considered the photon created source. During simulations there were three interesting findings in how MCNP5 treats x-ray production: (1) the U and Pu x-ray energies are 0.5 keV higher, (2) the 110 keV and 111 keV U x-ray peaks are combined into one peak at the average energy and (3) minor K-shell, L-shell and M-shell XRF interactions are not included in the physics calculations. The Pu x-ray energy increase by 0.5 keV caused the Eu-155 105.3 keV peak to interfere

with the Gaussian peak tail; therefore, the Eu-155 105.3 keV source was shifted to 105.8 keV to compensate.

Figure 50 shows the simple pin model photon simulation and measured spectrum normalized to the 98.4 keV U x-ray peak for the TMI 730 mm case. The measured and simulated spectra were analyzed using Genie 2000 software. The net peak areas and background integral counts from 101.3 keV to 102.4 keV were determined for comparison. Analysis showed the simulated fission product gamma peaks over predicted the measured peak values, shown by the 105.3 keV Eu-155, 123 keV Eu-154, and the 86.5 keV peaks. The analysis also showed the fission product gamma lines did not uniformly over predict the measured spectra values; therefore, TransLAT incorrectly calculates the relative build-up of certain fission products. Since the fission products visible in the spectra are uncommonly used for operation verification, it was expected these fission products were not benchmarked in the code. TransLAT does correctly calculate the decay of isotopes, and the gamma lines visible in the measured and simulated spectra are the same. For Pu/U x-ray analysis, the only fission product gamma line of concern was the Eu-155 peak at 105.3 keV (adjusted to 105.8 keV in the simulation). The measured spectra show the 105 keV peak height at approximately the same level as the 103.7 keV Pu x-ray peak, while the simulated spectra show the 105.3 keV peak relatively higher. This peak increase can cause the peak tail to interfere with the Pu x-ray peak. Since the 105.3 keV gamma line does not adversely affect the stimulation of U and Pu x-rays, the 105.3 keV gamma line was reduced to match the measured spectra to avoid Pu x-ray peak interference.

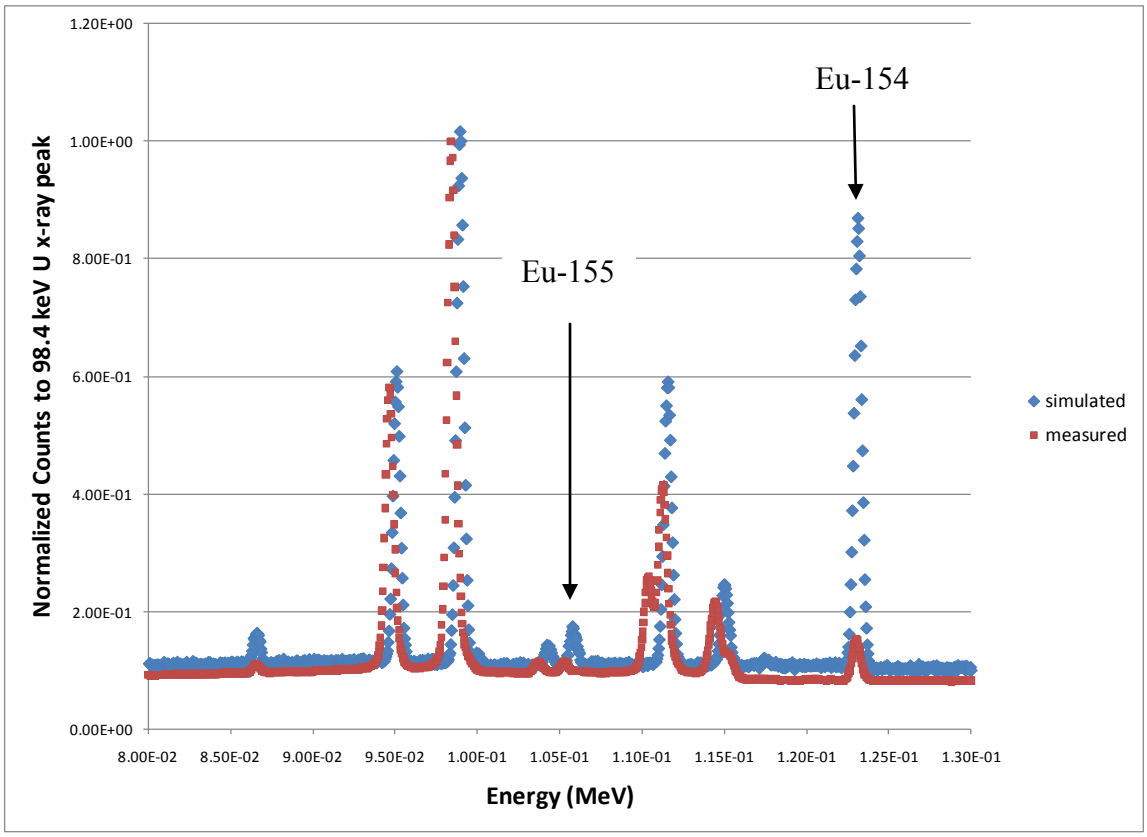

Figure 50. TMI 730 mm case simplified model and measured spectra

The Pu/U peak ratios were also analyzed for the simple fuel pin model simulations using Genie 2000 software. Figure 51 displays the TMI simulated and measured Pu/U peak ratios as a function of correlated burn-up using the 98.4 keV U x-ray peak. Figure 51 shows the simulations over predicted the Pu/U x-ray peak ratio compared to the measured values, but their relationships between Pu/U peak ratios are burn-up are similar. Since a relationship was able to be established, the simple spent fuel simulations can be benchmarked and used to predict spent fuel measurements. The simulations over predicted the Pu/U ratio by an average factor of 1.6. The North Anna simulations also

over predicted the Pu/U peak ratio compared to the measurements, but the burn-up values were too close to conclude a relationship.

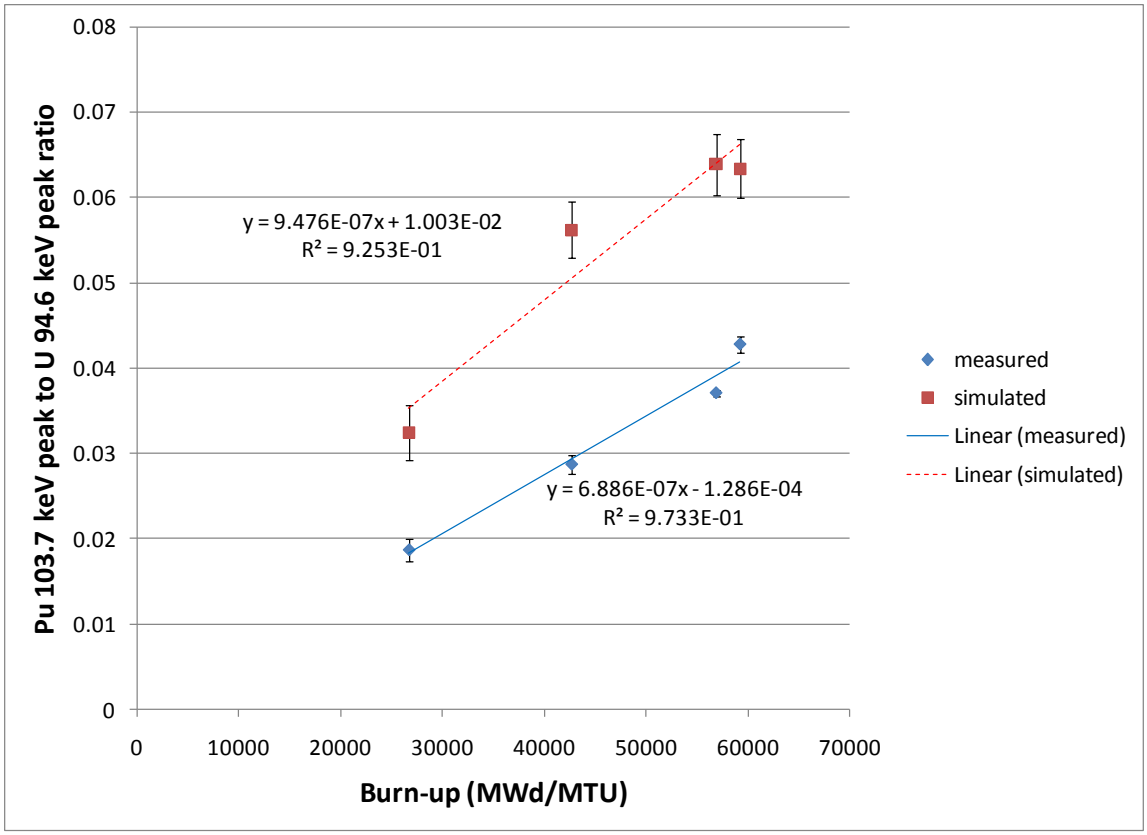

Figure 51. TMI simple model simulated and measured Pu/U ratio versus burn-up

4.3 Background Contribution from the Spent Fuel Rod

The spectra differences from the fuel, cladding, and shipping tube were also considered for the photon source problem. Figure 52 shows the results of North Anna photon simulations in the x-ray energy region. These photon simulations were conducted by excluding the cladding and then the cladding and shipping tube. Figure 52 shows by including the cladding and shipping tube, the gamma-ray peaks decrease significantly

from attenuation. Also the continuum remains approximately the same in the different simulations.

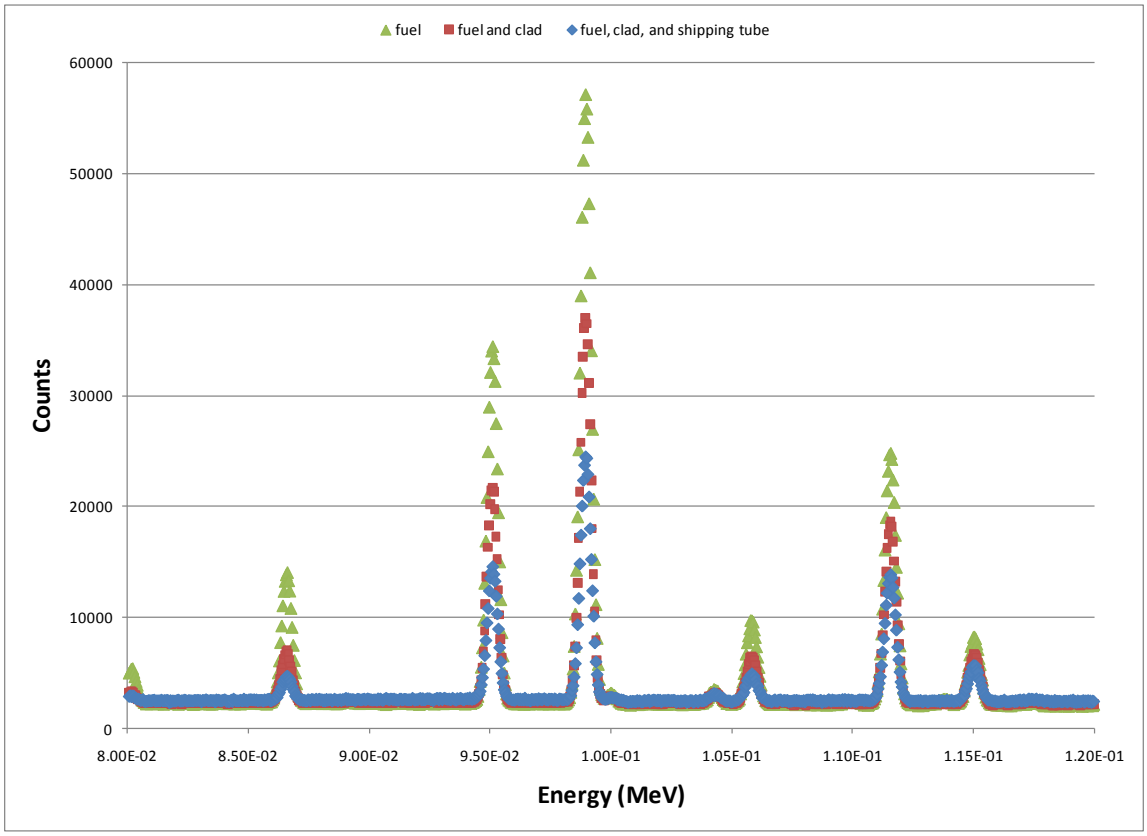

Figure 52. North Anna simplified pin model with photon induced gamma spectrum

The background level was also calculated for the photon simulations by excluding the peaks from the spectrum and averaging the background between 76.2 keV and 162 keV. Table 17 displays the calculated average background for the three cylindrical pin photon simulations. Table 17 shows the majority of the background contribution is from the fuel itself. By adding the cladding, the background increased by a 1.005 +/- 0.002 factor, and by adding the cladding and shipping tube the background increased by 1.086 +/- 0.002.

Table 17. Average background for North Anna 649A photon cylindrical simulations

	Average Background (counts/source particle)	**Uncertainty (counts/source particle)**
Fuel, Clad and Shipping Tube	2.337E-05	3.613E-08
Fuel and Clad	2.151E-05	3.626E-08
Fuel	2.140E-05	3.788E-08

The simple pin model TMI photon simulations showed similar results. Figure 53 shows the TMI 730 mm case simulations including the fuel, the fuel and cladding, and the fuel, cladding, and shipping tube. The background levels were also calculated for the TMI simulations, shown in Table 18.

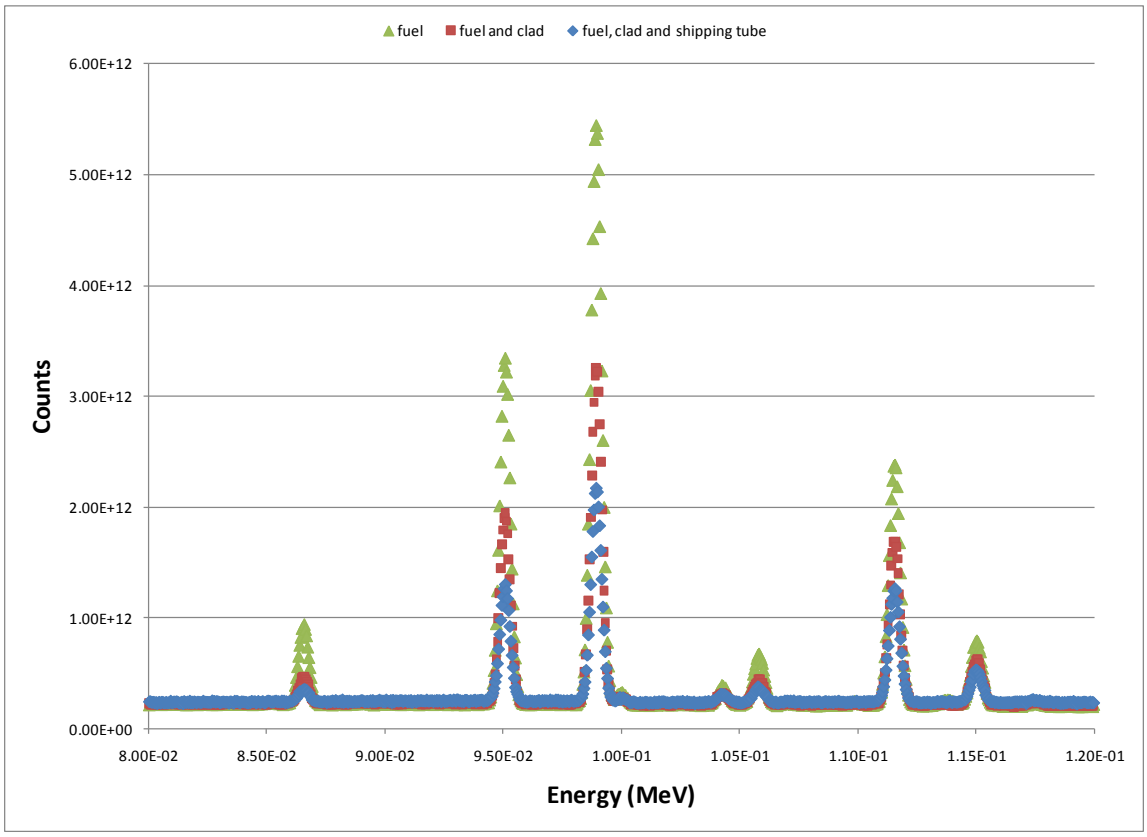

Figure 53. TMI simplified pin model with photon induced gamma spectrum

Table 18. Average background for TMI 730 mm photon cylindrical simulations

	Average Background (counts/source particle)	**Uncertainty (counts/source particle)**
Fuel, Clad and Shipping Tube	2.252E-05	4.336E-08
Fuel and Clad	2.085E-05	4.595E-08
Fuel	2.074E-05	4.891E-08

Table 18 shows the majority of the background contribution is from the fuel itself. By adding the cladding, the background increased by a 1.005 +/- 0.003 factor, and by

adding the cladding and shipping tube, the background increased by 1.080 +/- 0.003. These simulations show the fuel rod can be removed from the shipping tube for improved signal-to-noise ratio.

In conclusion, the cylindrical spent fuel pin simulations showed the fuel is the main contributor to the Compton background, and the shipping tube is the second strongest contributor. Spent fuel simulations, using only a photon source, adequately account for the creation of x-rays from Pu and U for spent fuel ranging from 26 GWd/MTU to 67 GWd/MTU burn-up values and cooling times from 4.2 to 13.3 years. TransLAT does not accurately calculate the relative amounts of uncommon fission products, but the Pu/U analysis is not adversely affected. Spent fuel simulations over predict the Pu/U ratio, but the relationship with fuel burn-up is similar.

4.4 Detector System Simulations

Detector simulations were performed to understand the sources of Compton background from the collimator, the detector and surroundings in the spent fuel measurements. Modeling the spent fuel experiments proved to be difficult using MCNP5/MCNPX. The detector system problem was essentially a radiation streaming problem through a pin hole geometry. The difficulty arose from the probability of the created XRF from the spent nuclear fuel reaching the detector. Traditional variance reduction techniques were applied to increase the probability of reaching the detector and improving statistics, such as directional biasing, energy and cell importances, etc.; however, MCNP does not have the ability to apply these techniques to secondary

radiation including XRF. Therefore, the detector system problem was solved using two separate simulations, a source definition simulation and a detector system simulation.

4.4.1 Photon and X-Ray Source Definition Simulations

The source definition simulations modeled a fuel pin with cladding and a shipping tube inside a void. The fuel pin contained 20 radial regions with uniform isotopics within each region using the TransLAT calculated isotopic distributions and primary photon sources from fission product and actinide decay. The source simulations accounted for gamma-rays from fission products, x-rays induced by gamma radiation, and Compton from fission product gamma-rays and x-rays (induced by gamma-rays) interacting in the fuel, cladding, and shipping tube. By assuming only photons, bremsstrahlung from the fuel, beta induced x-rays, and Compton from bremsstrahlung and beta induced x-rays were not accounted for in the simulations. Also the Eu-155 105.3 keV source was shifted in energy to 105.8 keV. Figure 54 displays the North Anna fuel pin geometry, and Figure 55 displays the TMI fuel pin geometry. The dimensions of the fuel pins were the same as the cylindrical fuel pin simulations.

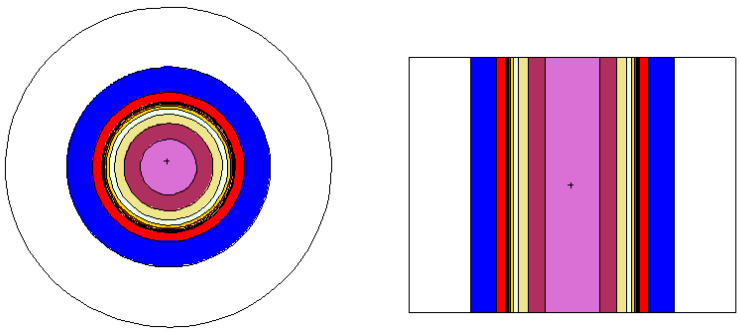

Figure 54. North Anna source definition simulation geometry, (left) x-y plane and (right) z-x plane

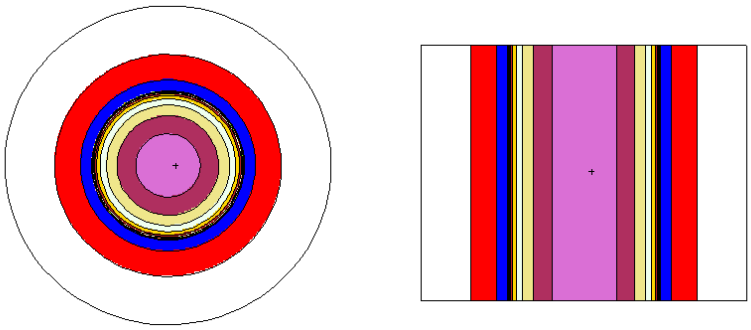

Figure 55. TMI source definition simulation geometry, (left) x-y plane and (right) z-x plane

The probability of emission was uniform over each region, and the initial source was isotropically emitted. The creation of secondary radiation, including XRF, is embedded in MCNP5. The photon surface flux through the shipping tube outer surface, including secondary radiation, was accounted for to be used in the detector simulations. Since the fuel pin was modeled in a vacuum, photons exiting the shipping tube cannot backscatter into shipping tube, and the surface flux accounts for only photons exiting the fuel pin. The surface flux provides the photons per cm^2 per source particle for the energy bin.

Source definition simulations were performed for the North Anna and TMI spent fuel cases using the surface flux tally over the shipping tube to account for photons and x-rays leaving the shipping tube. The surface flux was divided into five different tallies for the source definition, accounting for gamma-rays from 0 MeV to 1.6 MeV in energy: 0 to 0.08 MeV, 0.08 to 0.2 MeV, 0.2 to 0.4 MeV, 0.4 to 0.8 MeV, and 0.8 to 1.6 MeV. The surface tally was divided into 100 eV energy bins from 0 to 0.08 MeV and 0.2 to 1.6 MeV, and to ensure an accurate source definition for the x-ray region, the tally was divided into 60 eV energy bins from 0.08 to 0.2 MeV. After data analysis the energy bin

containing the Eu-155 105.8 keV peak was reduced to match the measured Eu-155 105.3 keV peak with respect to the Pu x-ray peak.

The surface flux over the cylindrical pin was then translated to a surface source probability distribution in the North Anna and TMI detector simulations. In the detector simulations, the energy was sampled by first sampling an energy bin according to the bin probabilities from the surface flux tally and then sampling uniformly within the chosen energy bin. The source was represented by a surface the size of the collimator hole. Since the surface flux source provided photons per surface area and the photons were emitted isotropically over the new defined surface source in the detector problem, the physics were maintained. Also by defining the surface source the size of the collimator hole, the source could be translated along the collimator length.

The disadvantage of the surface flux source is the resolution limit and an introduced source bias. Since an HPGe detector was implemented for the XRF measurements, the resolution from the surface flux source should be adequate. The source bias is introduced by binning the source in different energy groups causing forward peaked gamma-rays in the simulated spectrum. Since the energy bin size is 60-100 eV, the source biasing should be negligible. The advantages of using the surface flux tally are easier data analysis and defined uncertainties by MCNP5. With the chosen group structure, the uncertainties in the source simulations were approximately 1-3% in the 0.05 MeV to 0.2 MeV range, less than 1%-3% in the 0.2 MeV to 0.8 MeV range, and 2-7% in the 0.8 to 1.2 MeV range. Below 0.02 MeV the uncertainties ranged from 9-30%. Above 1.2 MeV

the problem was ill posed due to scarce gamma lines resulting in 30-100% uncertainties; therefore energies above 1.2 MeV were not included in the detector simulations.

4.4.2 North Anna MCNP5 Detector System Simulations

4.4.2.1 North Anna Detector System Geometry Modeling

The North Anna detector system simulations modeled the July 2008 North Anna spent fuel measurements. The detector system consisted of a long stainless steel collimator inside a high density concrete hot cell wall, an HPGe detector, and a circular surface source all within air. The stainless steel collimator was 36” in length and spanned the thickness of the hot cell wall. The collimator has two sections with a different pin hole sizes; the hole starts from a 3 cm hole narrowing to a pin hole diameter of 0.3 cm. The circular surface source was the size of the collimator pin hole, 0.3 cm diameter. Figure 56 shows the detector system set-up, from left to right: the nitrogen filled detector dewar, the HPGe detector, and the collimator inside the hot cell wall. The dimensions of the MCNP model are the same as the actual experiment; however, the supporting features and small details are excluded.

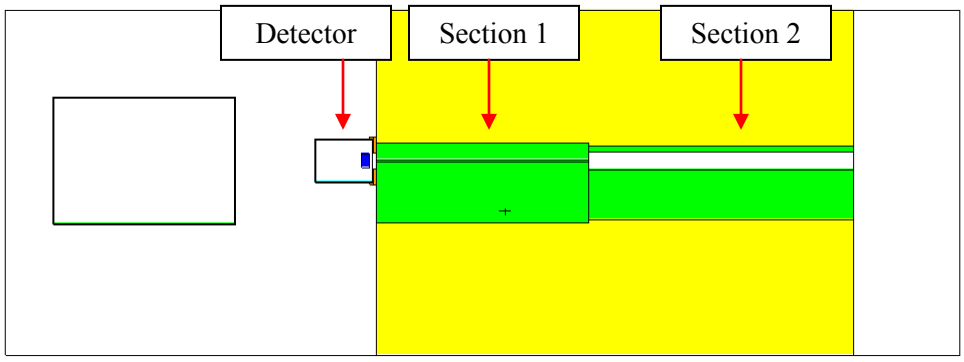

Figure 56. North Anna detector simulation geometry

Figure 57 shows collimator pin hole from the view of the detector. The pin hole is off centered vertically by 3.8 cm and has a radius of 0.15 cm. The detector window is aligned with the pin hole.

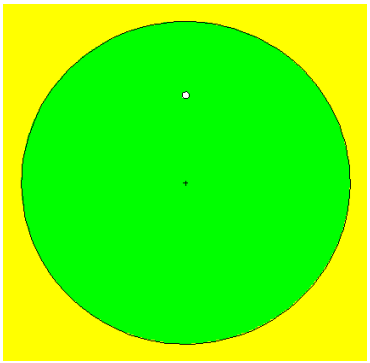

Figure 57. North Anna collimator pin hole geometry

Figure 58 shows a close up of the modeled HPGe detector. The HPGe detector was modeled using the detector specifications for the LEGe from the actual measurements. Figure 58 shows the Al detector can, HPGe crystal, the Al window and the tungsten collimator. The detector geometry also has been simplified by not including the electronics, the outer casing, and temperature controlling devices. All detector simulations were modeled in air.

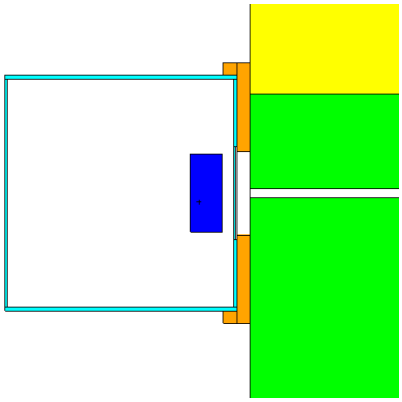

Figure 58. North Anna HPGe detector geometry

4.4.2.2 North Anna Detector System MCNP5 Movable Source Simulations

The detector simulations were performed to further understand the contributions of the stainless steel collimator, the tungsten collimator, the detector window, and the detector encasing to the measured background. In the North Anna simulations, the surface source was a 0.15 cm radius circular source (size of the collimator hole) and was moved along the length of the collimator. Figure 59 displays the locations chosen for simulations, marked with a red line: front of the detector (x=-0.001 cm) and 5 cm from the detector (x=5 cm). To account for the actual source difference at the different locations along the collimator, the probability of the radiation from the fuel rod reaching the location of the redefined surface source inside the collimator was estimated. The probability was calculated as the solid angle viewed from the location inside the collimator projected onto the fuel rod divided by the total solid angle (4π). The solid angle was calculated for each location of interest along the collimator and multiplied by the corresponding spectra output values for the TMI and North Anna simulations.

Additional simulations were also conducted to show the background contribution from the detector can and the tungsten collimator by changing those regions to voids.

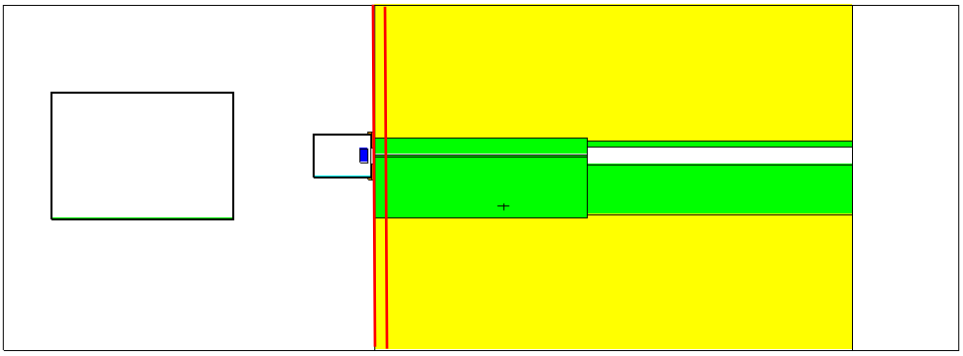

Figure 59. North Anna source locations

In the North Anna detector simulations, the defined photon source was born uniformly over the circular surface and implemented modified sampling methods. Any Monte Carlo event can be sampled from any arbitrary distribution rather than the physical probability as long as the particle weights are adjusted to compensate[21]. Thus with modified sampling methods, the statistical sampling of a problem can be altered to increase the number of tallies per particle[21]. The source biasing modified sampling method in MCNP5 was used to make more source particles start in a direction towards the detector crystal and to improve the convergence rate of the problem. A built-in exponential distribution function was used to generate a continuous probability density function for the source direction, provided by Equation (19).

$$p(\mu) = ce^{a\mu} \tag{19}$$

where a is a user specified parameter. The exponential biasing method does not create a monodirectional photon source; thus, the photons born in the collimator hole still have

interactions with the collimator, the wall, the tungsten detector collimator, and the detector encasing. Figure 72 shows the particle tracking for 1000 histories for the circular surface source at the collimator end (x=-0.001) with an exponential biasing of a=2. Figure 72 shows the photons have collisions with their surroundings, thus the simulated spectrum will show possible sources of background in the measurements.

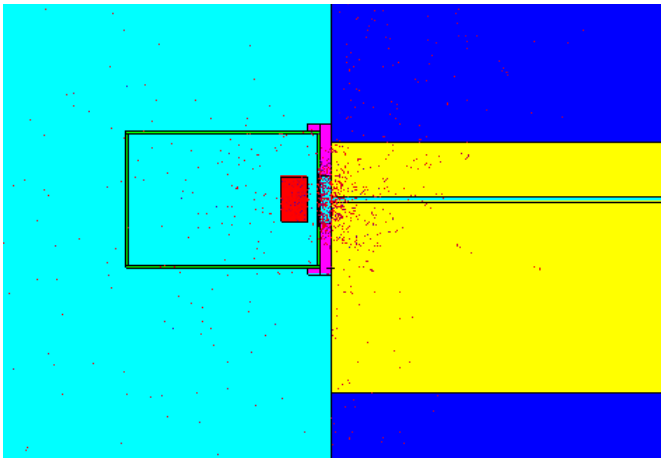

Figure 60. North Anna detector simulation particle tracking, source at x=-0.001

Figure 61 shows the North Anna 649A simulated spectrum for the circular source at x=-0.001 using an exponential bias of a=2.0 from 0 to 0.2 MeV. This spectrum includes the initial source and background from Compton interactions in the collimator end, the detector can, and the detector crystal. This simulated spectrum is similar to the cylindrical pin simulated spectra except for the additional peaks at 59.2 keV and 67.7 keV. The strong 59.2 keV peak is the result of high energy photons causing XRF of the tungsten collimator, and the 67.7 keV is from the Coulomb excitation of W-182.

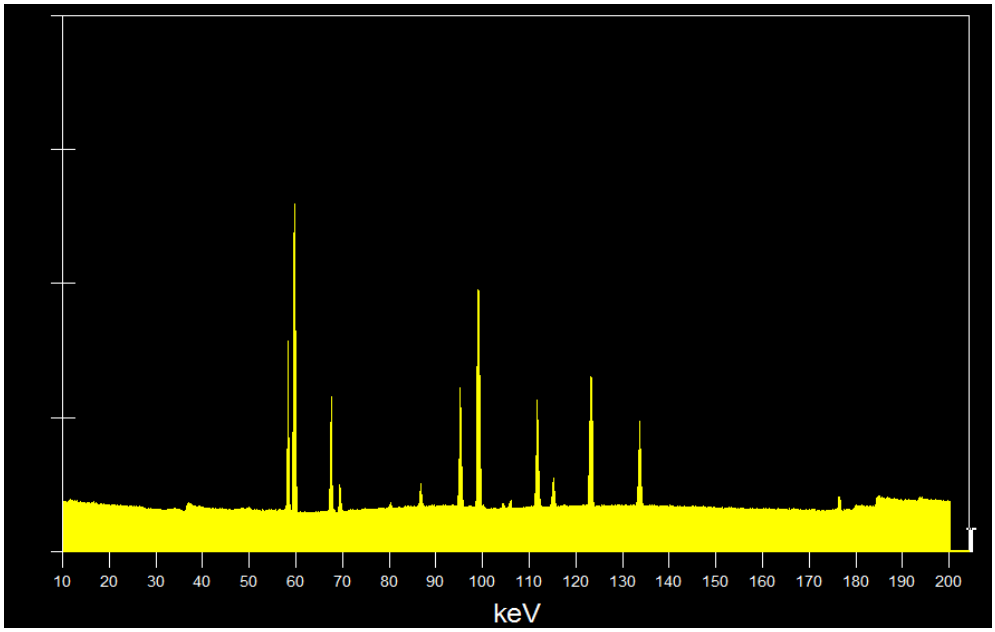

Figure 61. North Anna 649A detector simulation, source at x=-0.001

The background level was calculated for the source simulation at x=-0.001 by excluding the peaks from the spectrum and averaging the background between 76.2 keV and 162 keV. Prior to background averaging, the spectrum was corrected by accounting for the probability of the radiation reaching the initial location in the collimator from the spent fuel rod. Two more simulations were performed at x=-0.001, one excluding the tungsten collimator and one excluding the tungsten collimator and the detector can. The average background was also calculated for comparison.

Figure 62 shows the simulated spectra for the source at the detector front and using exponential biasing for the regular geometry case, the case without the tungsten collimator, and the case without the tungsten collimator and detector can. Figure 62 clearly shows the high energy photons interact with the front of the tungsten collimator, causing the tungsten XRF peaks and Compton excitation peaks. Figure 62 also shows

the continuum is slightly higher for the simulation not including the tungsten collimator; thus, the increase in background from Compton interactions in the tungsten collimator is less than the radiation attenuation through it. Without the tungsten collimator, the average background is 8.6 % +/- 0.13% higher than when included in the simulation, shown in Table 19.

Table 19 also shows the background is 3.16 % +/- 0.13 % lower when the detector can is additionally excluded; therefore, the background contribution from the detector encasing is greater than its radiation attenuation. The simulations at x=-0.001 cm showed the detector can contributes a majority of the background.

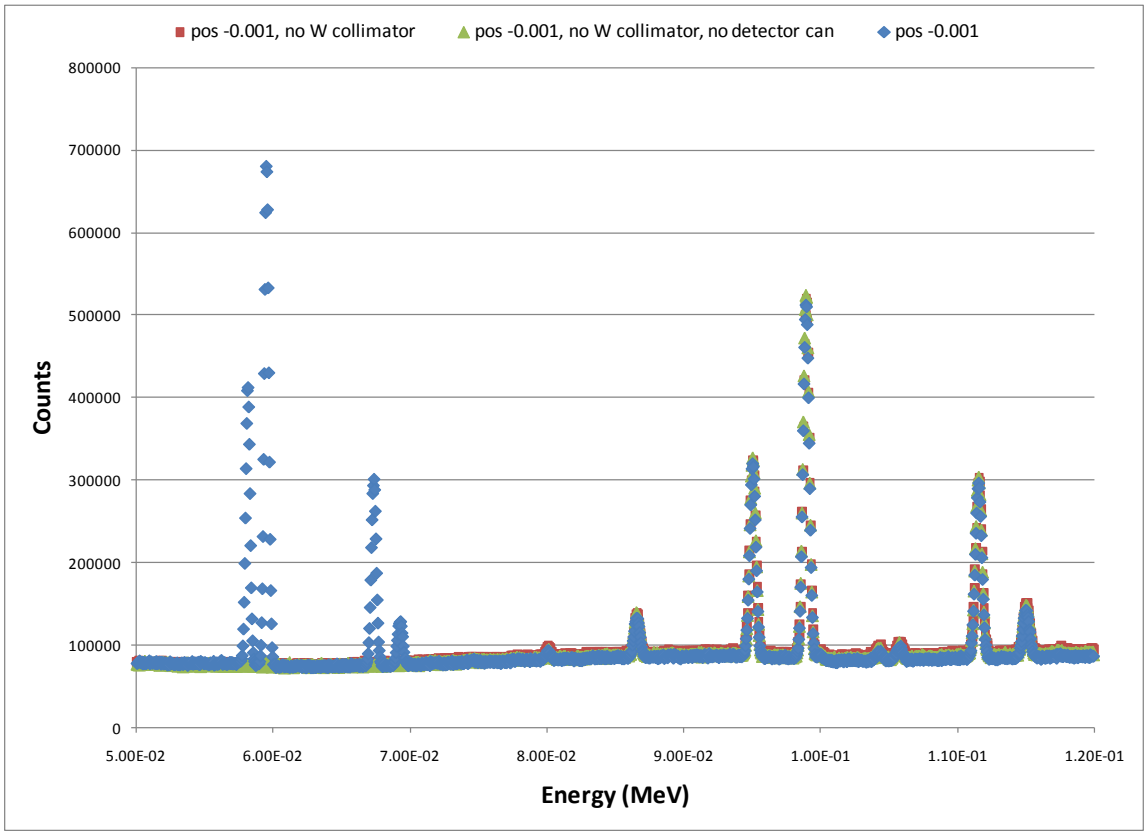

Figure 62. North Anna 649A detector simulation at detector front

Table 19. North Anna average background levels in detector using exponential biasing

	Average Background (counts/source particle)	**Uncertainty (counts/source particle)**
Position x=-0.001	8.430E-11	7.315E-14
Position x=-0.001, no W collimator	9.154E-11	8.482E-14
Position x=-0.001, no W collimator and detector can	8.863E-11	8.238E-14

In reality the radiation traveling out of the collimator hole would be streaming in an almost normal direction. Therefore, simulations were conducted where the source photons in the collimator hole were directed normal to the detector face, avoiding interactions with the stainless steel collimator, the wall, and the tungsten collimator. These normal source simulations were performed with the surface source at x=-0.001 cm, but the location along the collimator does not really matter. Three normal source simulations were performed, one regular North Anna geometry problem, one excluding the tungsten collimator, and one excluding the tungsten collimator and detector can. By excluding the tungsten collimator the background difference and backscatter off the tungsten collimator were observed.

Figure 63 shows the simulated spectra for the source at the detector front and using the normal source for the regular geometry case, the case without the tungsten collimator, and the case without the tungsten collimator and detector can. Figure 63 clearly shows a slight increase in the 59.2 keV peak from tungsten XRF when the tungsten collimator is included, thus photons are backscattering inside the detector from

the tungsten collimator into the crystal. However, the simulated spectra show the tungsten XRF peak is very small compared to the XRF from Pu and U and does not interfere. Table 20 shows the calculated average background for the normal source cases at x=-0.001 cm. Without the tungsten collimator, the average background is 0.06 % +/- 0.23% higher than when included in the simulation. Table 20 also shows the background is 0.35 % +/- 0.23 % higher when the detector can is additionally excluded. Within uncertainties the background level are consistent. Therefore when the source is normal to the detector window, the addition of the detector can and tungsten collimator do not significantly affect the background level and only slightly attenuate the incoming radiation.

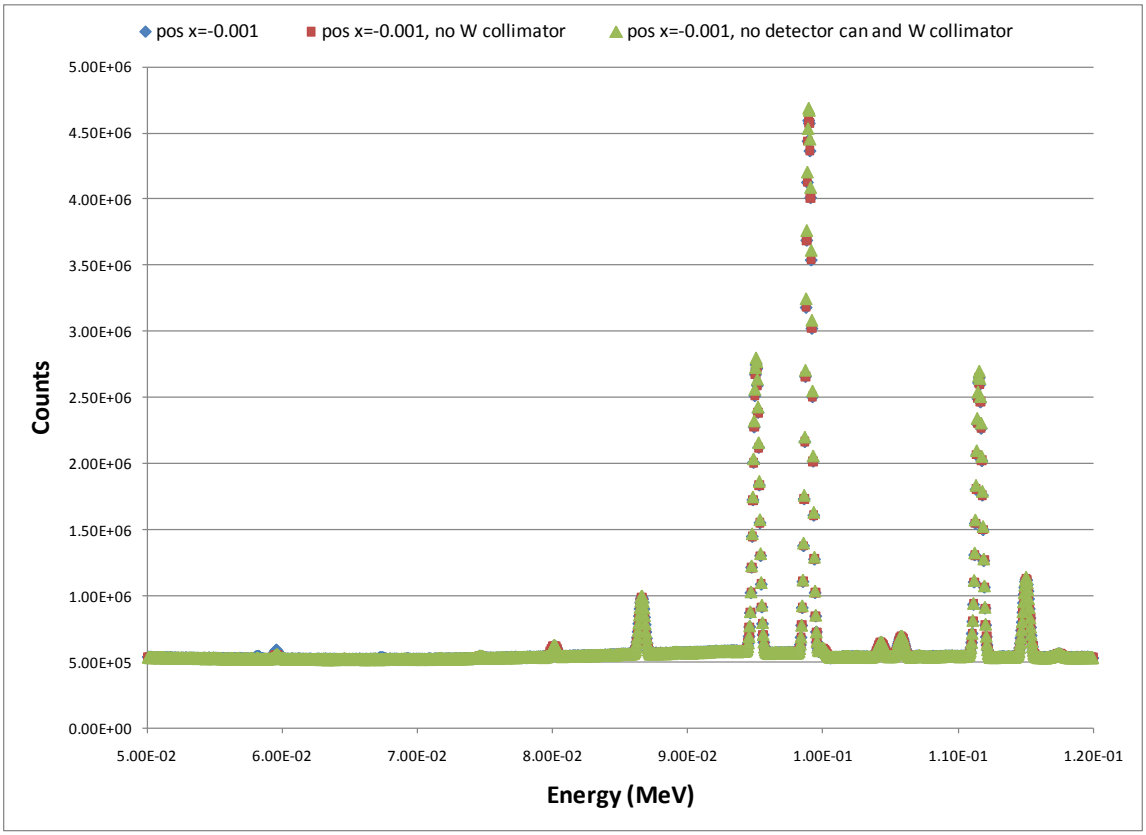

Figure 63. North Anna 649A detector simulation at detector front using normal source

Table 20. North Anna average background levels in detector using normal source

	Average Background (counts/source particle)	**Uncertainty (counts/source particle)**
Position x=-0.001	5.163E-10	8.524E-13
Position x=-0.001, no W collimator	5.166E-10	8.608E-13
Position x=-0.001, no W collimator and detector can	5.185E-10	8.534E-13

Figure 64 displays the photon spectrum with source at x=5 cm using exponential biasing of a=2.0. The tungsten XRF peaks are visible but the U and Pu x-rays are

swamped by the background created inside the collimator. Additional simulations showed due to the small size of the collimator pin hole (0.3 cm diameter), the detector simulation model is not a well posed problem when using the Monte Carlo techniques.

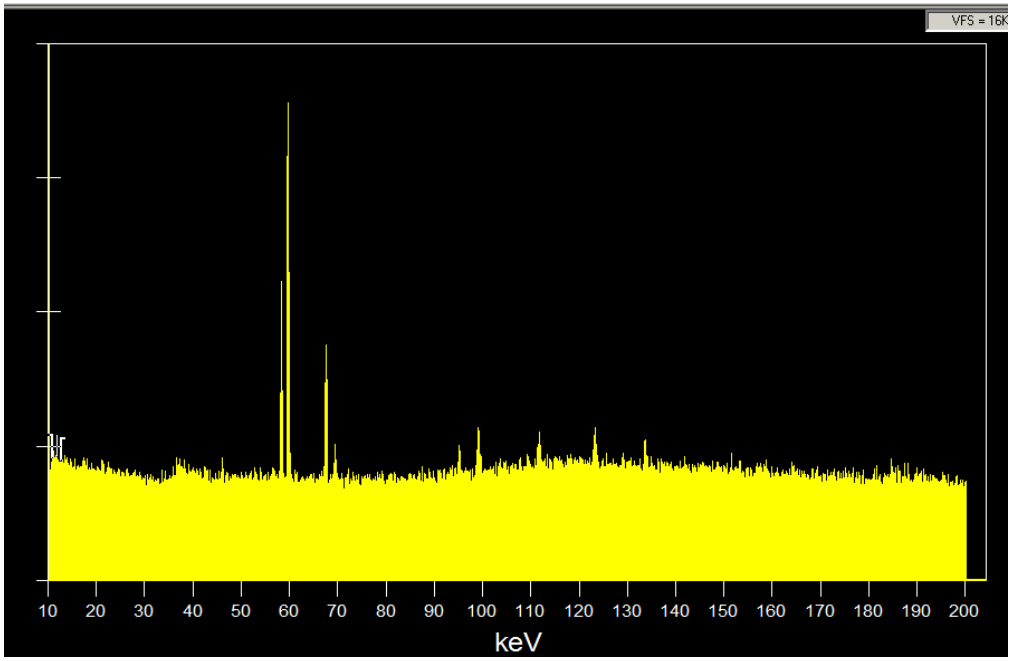

Figure 64. North Anna detector simulated spectra, source 5 cm from detector

4.4.3 TMI MCNP5 Detector System Simulations

4.4.3.1 TMI Detector System Geometry Modeling

The TMI detector system simulations modeled the January 2009 TMI spent fuel measurement campaign. The detector system consisted of a stainless steel collimator inside a high density concrete hot cell wall, a collimator extension piece outside the hot cell, an HPGe detector, the nitrogen filled detector dewar, and a rectangular surface source the size of the collimator hole all within air, shown in Figure 65. The collimator was 65.75” in length inside the hot cell, and the collimator had an extension outside the

hot cell wall 12.25” in length. For modeling the collimator was divided into 4 sections from left to right: the main section, the second section, collimator end plate, and collimator extension piece. The collimator also contained a movable section to change the collimator hole size inside the hot cell; it was assumed the collimator hole was the same as the end plate near the detector, 0.25” by 0.75”. However the collimator hole height changes depending on the collimator section; Figure 72, 73, 74 and 75 show the cross sectional views of the collimator from inside the hot cell to the detector.

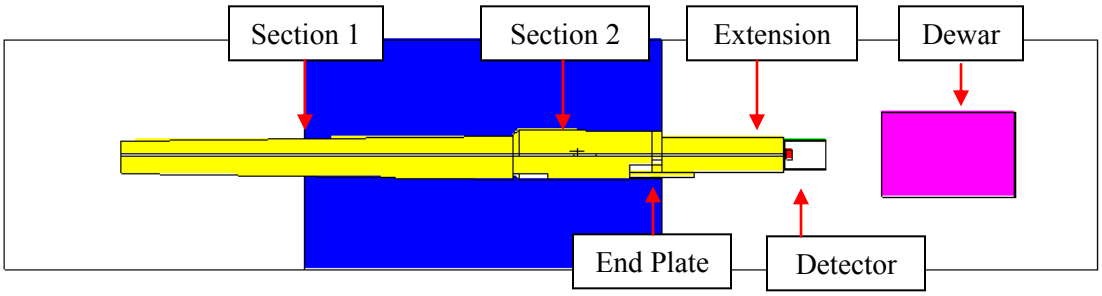

Figure 65. TMI detector simulation geometry

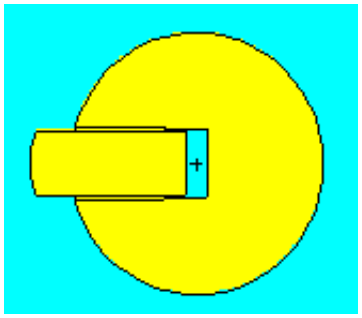

Figure 66. TMI collimator hole geometry inside hot cell at collimator end (Section 1), 0.25” by 0.75”

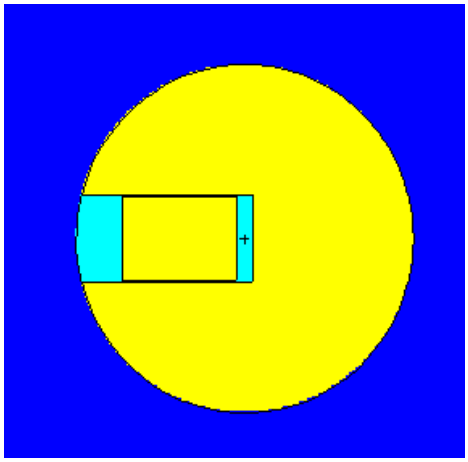

Figure 67. TMI collimator hole geometry Section 2, 0.25” by 1.3”

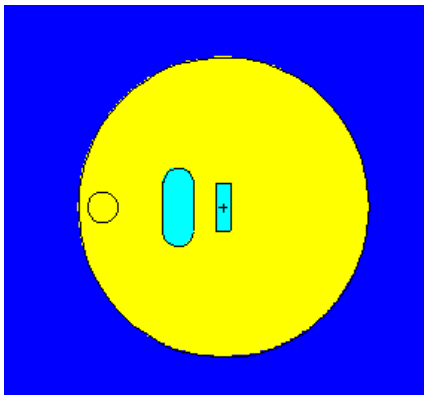

Figure 68. TMI collimator hole geometry inside end plate, 0.25” by 0.75”

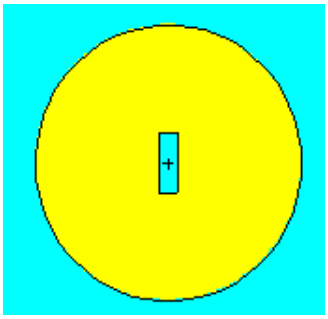

Figure 69. TMI collimator hole geometry in extension piece, 0.25” by 0.75”

The detector window is aligned with the collimator hole in Figure 69. Figure 70 shows a close up of the modeled HPGe detector. The HPGe detector is the same as the detector in the North Anna simulations except the tungsten collimator was removed as in the actual experiments. The detector geometry has also been simplified by not including the electronics, the outer casing, and temperature controlling devices. The major dimensions of the MCNP model are the same as the actual experiment; however, the supporting features and small details are excluded.

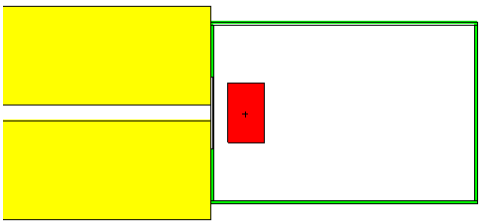

Figure 70. TMI HPGe detector geometry

4.4.3.2 TMI Detector System Movable Source Simulations

In the TMI simulations, the surface source has the 0.25” by 0.75” dimensions of the collimator hole and was moved along the length of the collimator. Figure 71 displays the locations chosen for simulations, marked with a red line: front of the detector (x=169.576 cm), 5 cm from the detector (x=165.575 cm), before collimator extension piece (x=138.429 cm), and beginning of section 2 (x=101.771 cm). These locations were chosen to show how the Compton background changes by adding the different collimator sections between the source and detector. The furthest location was based on the limits of the exponential biasing to provide good statistics.

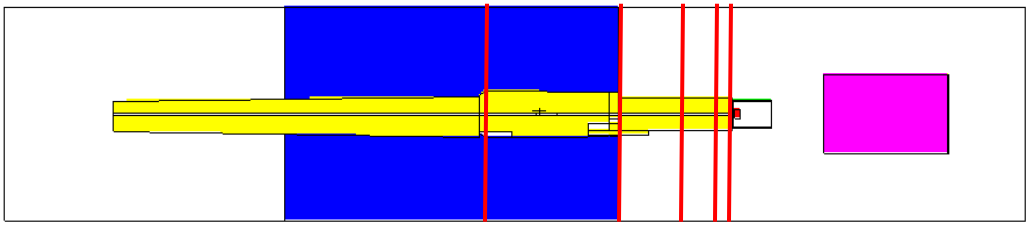

Figure 71. TMI source locations along collimator

Detector simulations were performed for TMI cases 261 mm (26.7 GWd/MTU), 411 mm (42.7 GWd/MTU), 730 mm (56.9 GWd/MTU) and 1984 mm (59.2 GWd/MTU) to observe the relationship between Pu/U simulated peaks and spent fuel burn-up. The detector simulations used the surface source located at the detector front (x=169.576) and implemented exponential directional biasing. The simulated spectra were analyzed using Genie 2000 software. Figure 72 displays the detector system simulated Pu/U peak ratio, the simple model simulated Pu/U peak ratio, and the measured Pu/U peak ratio for the different locations of the spent fuel. As expected the detector simulated Pu/U ratios over predict the measured Pu/U ratios; however the detector simulations more closely follow the trend of the measurements compared to the simple pin model simulations. This similar relationship shows that spent fuel simulations, like those performed in the thesis, can be benchmarked and used to predict Pu/U ratios in the spent fuel measurements. In theory, measurements and benchmarked simulations could be made for different fuel types (PWR, BWR, MOX, etc.) to create a data library that would be used to make accurate predictions of Pu content in spent fuel through simulations.

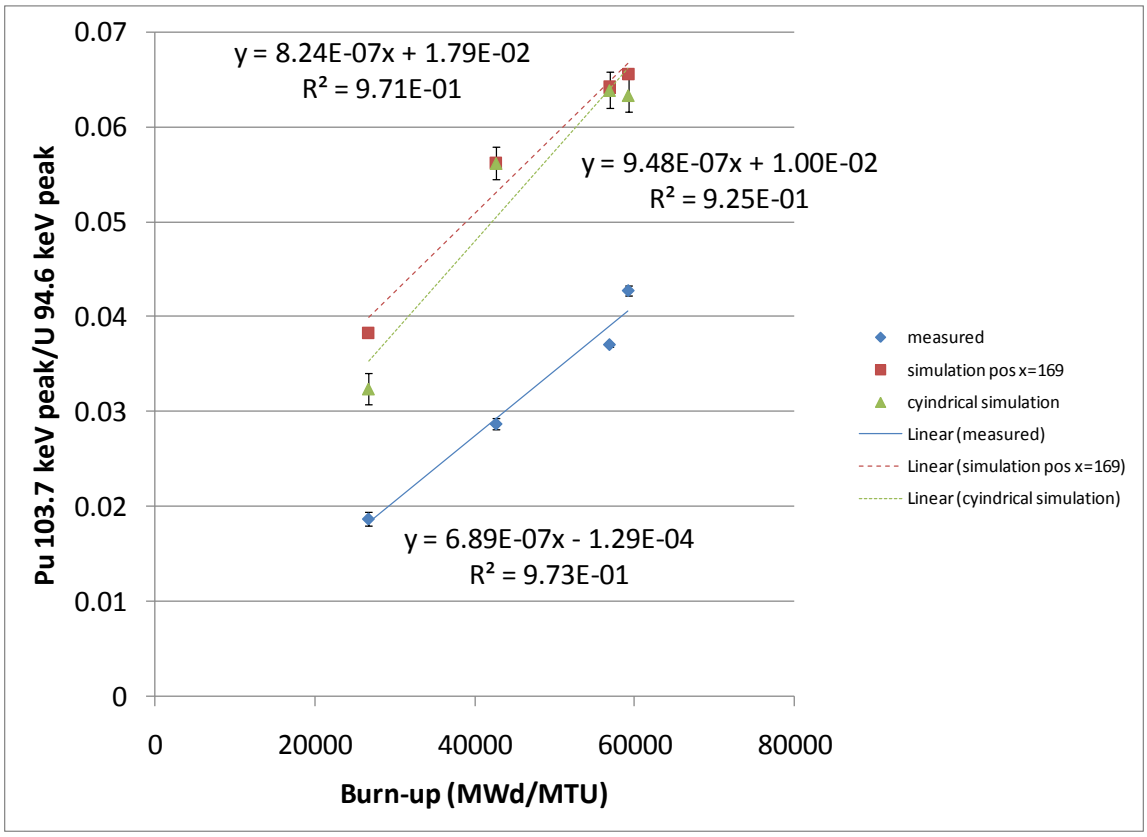

Figure 72. TMI detector simulation Pu/U versus burn-up comparison

To understand the background contributions, simulations were performed at the different locations along the collimator. At 0 cm (x=169.576 cm), 5 cm (x=164.575 cm), 10 cm (x=165.575 cm) and 31 cm (x=138.429 cm) away from the detector, exponential directional biasing of a=2 was implemented. The spectra with the source at 169.576 cm and 164.575 cm had clearly visible Pu and U x-ray peaks and a well defined continuum with uncertainties less than one, shown by Figure 73.

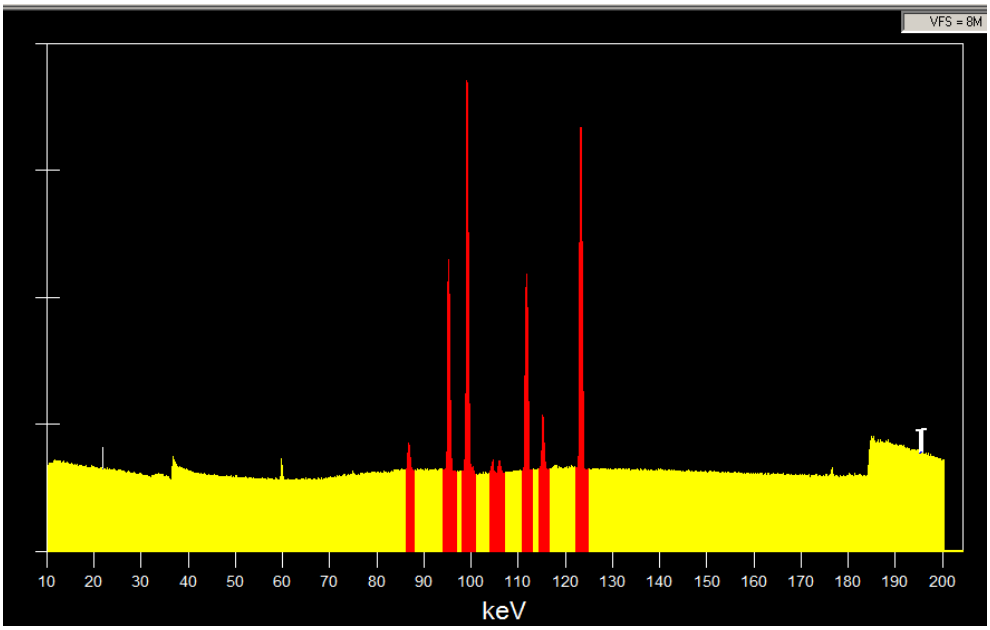

Figure 73. TMI 730 mm detector simulation, source at detector front

With increasing distance from the detector, the spectra could not distinguish the Pu x-ray peak due to uncertainties. The exponential biasing was increased to a=3.5 (strong bias); however, this increase caused over-biasing in the simulation and introduced catastrophic events in the detector. A catastrophic event in the detector happens when a low probability, high weight particle has an interaction in the detector crystal, causing the tally in the particular energy bin to drastically and unnaturally increase with high uncertainties. The main purpose of the detector simulations was to understand the sources of background in the detector system; therefore, the Pu x-ray peak does not have to be resolved to obtain the average background level. For the source at x=101.711 cm, the exponential biasing was increased to a=25 to provide better statistics in the detector crystal and still avoid overbiasing in the x-ray energy region, shown in Figure 74. To

observe the background contribution of the detector can, an additional simulation was performed at the detector front in which the detector can was excluded.

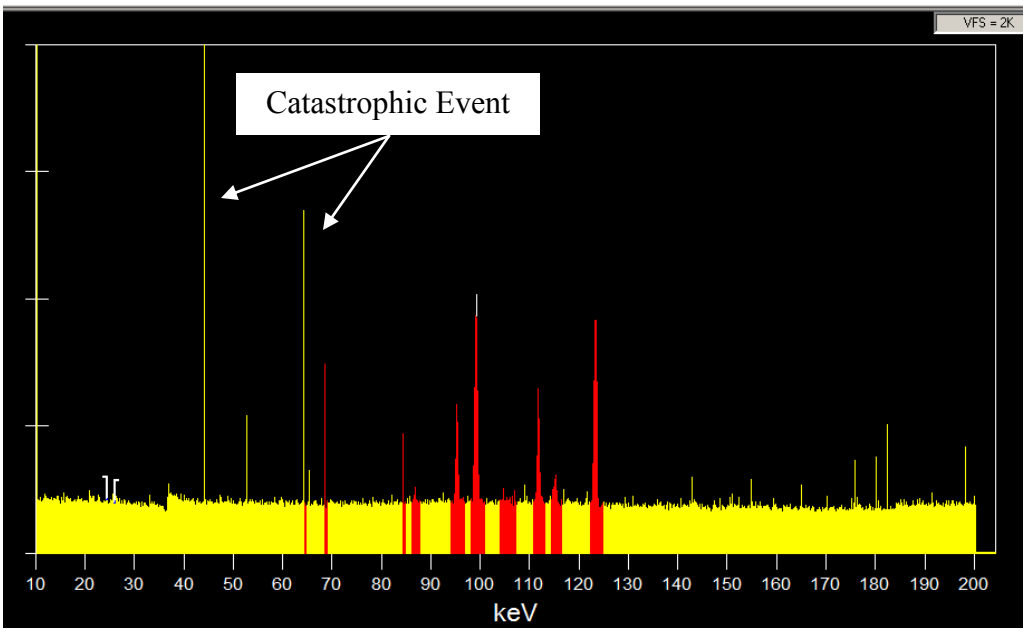

Figure 74. TMI 730 mm detector simulation, source at x=101.771 cm

Table 21 displays the average background levels for the cylindrical fuel simulations, the detector simulations with the surface source at different locations along the collimator, and the detector simulation excluding the detector can. In the detector simulations, the background from the fuel rod, cladding, and shipping tube are included in the surface source. The Compton produced inside the fuel is the main source of background, followed by the shipping tube and then the fuel cladding. Comparing the background in the detector simulations with and without to detector can, the interactions in the detector can contribute more to the continuum than interactions in the crystal. By excluding the detector can, the background decreased by 3.93 % +/- 0.10 %. The calculated average background with the source at different locations in the collimator

decreases proportionally to the inverse of the distance between the source and detector crystal squared ($1/r^2$). This behavior suggests the continuum contribution from the collimator is approximately the same no matter where the source is located. Therefore, it can be concluded most of the Compton continuum contribution from the collimator occurs at the collimator end. In conclusion the Compton continuum contributors in order of strongest to weakest are the following: the fuel, the shipping tube, the fuel cladding, the detector can, and the collimator end.

Table 21. TMI average background levels

	Average Background (counts/source particle)	**Uncertainty (counts/source particle)**
Fuel, Clad and Shipping Tube	2.252E-05	4.336E-08
Fuel and Clad	2.085E-05	4.595E-08
Fuel	2.074E-05	4.891E-08
Position x=169.576 (detector front)	1.303E-10	9.502E-14
Position x=169.576, no detector can (detector front)	1.252E-10	8.331E-14
Position x=164.575 (5 cm from detector)	9.584E-12	2.274E-14
Position x=159.575 (10 cm from detector)	1.538E-12	4.579E-15
Position x=138.429 (31 cm from detector)	1.156E-13	6.085E-16
Position x=101.771 (68 cm from detector)	1.881E-14	5.883E-17

4.5 Detector System Simulation Overview

The detector simulations showed the contributions to the Compton continuum from strongest to weakest are as follows: the fuel rod, the shipping tube, the cladding, the detector can, and the collimator end. The detector simulations accounted for the Compton produced by fission product gamma rays, Compton gamma-rays, and x-rays (induced gamma-rays in fuel) interacting in the collimator, cladding, shipping tube, detector, and detector can. The simulated spectra also accounted for the fission product gamma-rays and x-rays in the fuel. The detector simulations also showed the surface flux source was able to approximate the actual gamma-ray spectrum from the fuel rod. The detector simulations also showed the relationship between the simulated Pu/U ratio and fuel burn-up followed the same relationship as the spent fuel Pu/U measurement ratios.

5. CONCLUSIONS

The July 2008 and January 2009 spent fuel measurement campaigns at ORNL showed the Pu $K_{\alpha 1}$ x-ray at 103.7 keV can be measured from a single spent fuel rod using a planar HPGe detector with count time between 4 to 12 hours. These measurements were the first successful measurements of the Pu x-ray peak from PWR spent fuel. Cs-137 and Cs-134 measurements and Origen2 simulations were also utilized to determine the fuel burn-up at the XRF measurement locations. The 4.2 year old North Anna spent fuel measurements ranged from 62 to 67 GWd/MTU in burn-up, while the 13.3 year old TMI fuel measurements ranged from 27 to 60 GWd/MTU. The TMI XRF measurements provided quantitative results showing the linear relationship between the Pu/U measured ratio and fuel burn-up.

The cylindrical fuel pin simulations showed that for 4.2 year to 13.3 year old fuel ranging from ~50 GWd/MTU to ~67 GWd/MTU burn-up the photon source contributes approximately 86% and the beta source contributes approximately 14% to x-rays. The simulations also showed that the U x-ray peak to background ratio and Pu x-ray peak to background ratio were in good agreement between the photon source and beta source problem. Therefore, it can be assumed that the signal-to-noise ratio is directly proportional to the source activity, and for the simplified pin case, the photon source does not underestimate the background. The cylindrical fuel pin simulations showed the photon source adequately models the XRF and the Compton continuum in the spent fuel simulations.

Cylindrical fuel pin simulations were also conducted considering the affects of the Compton sources from the cladding, shipping tube, and fuel on the measured spectra. Analysis showed the Compton from the fuel contributed the most to the background, followed by the shipping tube and the cladding. TMI fuel pin simulations were also performed for different fuel burn-up values to establish a relationship between the Pu/U peak ratio and fuel burn-up. Comparing the actual measurement Pu/U ratios, the fuel pin simulations over predicted the Pu/U ratios, but the linear relationship was similar.

The simple fuel pin simulations also showed the relative concentrations of more uncommon fission products were calculated incorrectly using TransLAT. However this did not have an adverse effect on the relative stimulation of XRF in the spent fuel.

Detector system simulations were performed to understand the contributions to the Compton continuum from the detector can and the collimator. The detector simulations showed the contributions to the Compton continuum from strongest to weakest are as follows: the fuel, the shipping tube, the cladding, the detector can, and the collimator end.

MCNP5 source definition simulations accurately characterized the spent fuel spectrum, with the exception of the relative fission products due to the TransLAT calculated input. The surface flux defined surface source introduced a slight energy bias into the simulation, but worked for the HPGe resolutions. If one were performing Microcalorimeter spent fuel measurement simulations, one would want to use PTRAC in MCNP5 to create the source. The PTRAC method has the advantage of infinite resolution as the detector system source due to the output of discrete energies.

The detector system simulations were not well posed Monte Carlo problems. The detector system simulations consist of a radiation streaming problem with a small detector and small source geometries. Additional detector system simulations should be solved using deterministic methods or hybrid methods.

In addition to the simulations, destructive assay measurements should be conducted on the spent fuel at the locations of the XRF measurements. Destructive analysis will provide definite information on the Pu/U content and provide a benchmark for the XRF measurements and simulations.

REFERENCES

1. A.V. BUSHUEV, V.I. GALKOV, A.V. ZBONAREY, A.F. ZOLOTOV, A.A. KUTUZOV, N.A. MEL'NICHENKO, V.N. OZERKOV and V.V. CHACHIN, "A Nondestructive Method of Determining the Pu/U Ratio in Fast Reactor Fuel Elements, Based on X-Ray Spectrometry," *Atomic Energy*, **53**, 5 (1982).

2. C. RUDY, P. STAPLES, K.SEREDNIUK and I. YAKOVLEV, "Determination of Pu in Spent Fuel Assemblies by X-Ray Fluorescence," *Proceedings of 46th Annual Meeting of the INMM*, Phoenix, Arizona (July 10-14, 2005).

3. P.M. RINARD and G.E. BOSLER, "Safeguarding LWR Spent Fuel with the Fork Detector," Los Alamos National Laboratory LA-1 1096-MS (1988).

4. J.R. PHILLIPS, J.K. HALBIG, H.O. MENLOVE and S.F. KLOSTERBUER, "Apparatus for In Situ Determination of Burnup, Cooling Time and Fissile Content of an Irradiated Nuclear Fuel Assembly in a Fuel Storage Pond," United States Patent 4,510,117 (1985).

5. H.O. MENLOVE, T.D. REILLY, and R. SIEBELIST, "The Verification of Reactor Operating History Using the Fork Detector," *Proceedings of 37th Annual Meeting of the INMM*, Naples, Florida (July 28-31, 1996).

6. D.H. BEDDINGFIELD and H.O. MENLOVE, "Reactor Fuel Irradiation History Verification Using FDET Measurement of Fresh-Discharged Fuel Assemblies," Los Alamos National Laboratory LA-UR-01-2012 (2001).

7. "Use of the Fork Detector in Safeguards Inspections," Studiecentrum Voor Kernenergie Centre D'Etude de L'Energie Nucleaire, Scientific Report, Belgium (2007).

8. C. WILLMAN, A. HAKANSSON, O. OSIFO, A. BACKLIN, and S.J. SVARD, "Nondestructive Assay of Spent Nuclear Fuel with Gamma-ray Spectroscopy," *Annals of Nuclear Energy*, **33** (2006).

9. C. WILLMAN, O. OSIFO, A. HAKANSSON, and S.J. SVARD, "A Semi-Empirical Technique of Spent Nuclear Fuel Assemblies," *Proceedings of the 27th Annual Conference of the ESARDA*, London, United Kingdom (May 10-12, 2005).

10. C. WILLMAN (2006), Applications of Gamma Ray Spectroscopy of Spent Nuclear Fuel for Safeguards and Encapsulation. Ph.D. dissertation, Uppsala University, Uppsala, Sweden.

11. S.J. TOBIN, S.F. DEMUTH, M.L. FENSIN, J.S. HENDRICKS, H.O. MENLOVE and M.T. SWINHOE, "Determination of Plutonium Content in Spent Fuel with NDA—Why an Integrated Approach?" Los Alamos National Laboratory, LA-UR-08-03763 (2008).

12. O. OLDENBERG and N.C. RASMUSSEN, *Modern Physics for Engineers*. McGraw- Hill, Inc., New York (1996).

13. D. Reilly, N. Ensslin, S. Smith Jr., and S. Kreiner, *Passive Non-Destructive Assay of Nuclear Materials*, Washington, DC, NUREG-CR/5550 (1991).

14. Evaluated Nuclear Data File ENDF/B-6.0, Cross Section Evaluation Working Group, Brookhaven National Laboratory (2002).

15. W.M. STACEY, *Nuclear Reactor Physics*, John Wiley and Sons, Inc. (2001).

16. H. BAIRIOT, "Plutonium Management Options: Liability or Resource," *Nuclear Engineering and Technology*, **40**, 1 (2008).

17. "The Physics of Pu Recycling," Nuclear Energy Agency/Organization for Economic Co-operation and Development, **1-5** (1995).

18. "IAEA Safeguards Glossary 2001 Edition," International Atomic Energy Agency (2002).

19. M. SCHANFEIN, "Science and Technology Challenges for International Safeguards," *Proceedings of the INMM 49th Annual Meeting*, Nashville, Tennessee (July 13-17, 2008).

20. R.G. COCHRAN and N. TSOULFANIDIS, *The Nuclear Fuel Cycle: Analysis and Management* 2nd edition, American Nuclear Society, La Grange Park, Illinois (1990).

21. "A General Monte Carlo N-Particle Transport Code Version 5 Manual", Los Alamos National Security (2005).

22. "TransFXTM Computer Software Manuals: Advanced Particle Transport Software Using Three-Dimensional Deterministic Methods in Arbitrary Geometry," TransWare Enterprises Inc. (2001).

23. A.G. Croff, "A User's Manual for ORIGEN2 Computer Code," ORNL/TM-7175 (1980).

24. D.B. PELOWITZ, et al., "MCNPX 2.7A Extensions," LA-UR-08-07182, Los Alamos National Laboratory (2008).

25. W.S. CHARLTON, D. STROHMEYER, A. STAFFORD, S. SAAVEDRA, A.S. HOOVER, C.R. RUDY, "The Use of Self-Induced XRF to Quantify the Pu Content in PWR Spent Nuclear Fuel," *Proceedings of the 31st Annual Conference of the ESARDA*, Vilnius, Lithuania (May 26-28, 2009).

26. Canberra Industries, "Low Energy Germanium Detector," http://www.canberra.com/products/493.asp (2008).

27. G.F. KNOLL, *Radiation Detection and Measurement* 3rd Edition, John Wiley & Sons, Inc. (2000).

28. "Detector Specifications and Performance Data," Canberra Industries Report (2004).

29. "Summary Report of Commercial Reactor Criticality Data for Three Mile Island Unit 1," TDR-UDC-NU-000004 Rev 01, Bechtel SAIC Company, Las Vegas, Nevada (2001).

30. J.C. WAGNER, "Impact of Soluble Boron Modeling for PWR Burnup Credit Criticality Safety Analyses," *Trans. Am. Nucl. Soc.* **89**, 120-122 (2003).

31. W.S. CHARLTON, R.T. PERRY, B.L. FEAREY and T.A. PARISH, "Calculated Actinide and Fission Product Concentration Ratios for Gaseous Effluent Monitoring Using MONTEBURNS 3.01." *Nucl. Tech.*, **131** (2000).

32. Ernest O. Lawrence Berkeley National Laboratory and Lund University, Sweden, "WWW Table of Radioactive Isotopes", http://ie.lbl.gov/toi/index.asp, (1999).

APPENDIX A

NORTH ANNA CS-134/CS-137 ACTIVITY CALCULATIONS

Summary of MCNP5 surface flux values for calculating the probability of escape

Energy (MeV)	Flux (p/cm2/s)	Fractional Standard Deviation
4.00E-01	6.70E-03	0.0044
5.00E-01	1.05E-02	0.0034
6.00E-01	1.33E-02	0.0029
6.62E-01	1.47E-02	0.0027
7.00E-01	1.55E-02	0.0026
8.00E-01	1.72E-02	0.0025
9.00E-01	1.86E-02	0.0024
1.00E+00	1.96E-02	0.0023
1.10E+00	2.05E-02	0.0022
1.20E+00	2.13E-02	0.0022
1.30E+00	2.20E-02	0.0021

Summary of relative attenuation to a 662 keV gamma-ray for calculating the probability of escape

Energy (MeV)	Relative Attenuation (no units)	Standard Deviation (no units)
4.00E-01	0.45486	0.00235
5.00E-01	0.71141	0.00309
6.00E-01	0.90403	0.00358
6.62E-01	1.00000	0.00382
7.00E-01	1.05209	0.00394
8.00E-01	1.16753	0.00430
9.00E-01	1.26027	0.00455
1.00E+00	1.33384	0.00473
1.10E+00	1.39459	0.00486
1.20E+00	1.44927	0.00505
1.30E+00	1.49479	0.00511

Summary of Relative Efficiency Calibration using Eu-152 source for North Anna Cs-134/Cs-137 activity calculations

Energy (keV)	Yield (%)	Net Peak Area	Net Area Uncertainty	Relative Efficiency to 662 keV	Efficiency Uncertainty
121.7817	28.58	1.00E+07	3558.66	3.49E+05	1.24E+02
244.6975	7.5834	2.24E+06	1530.09	2.94E+05	2.01E+02
295.9392	26.51993	1.11E+05	1112.42	2.48E+05	2.48E+03
329.425	0.860572	2.92E+04	424.66	2.26E+05	3.29E+03
416.048	2.234039	1.91E+04	336.14	1.73E+05	3.04E+03
443.965	2.821359	5.49E+05	1126.9	1.74E+05	3.57E+02
488.6792	0.418921	6.67E+04	405.74	1.59E+05	9.66E+02
563.99	0.489321	7.21E+04	417.7	1.47E+05	8.51E+02
566.439	0.459325	2.11E+04	346.86	1.63E+05	2.68E+03
656.487	0.471259	1.78E+04	839.91	1.23E+05	5.78E+03
674.675	0.85658	2.17E+04	319.47	1.25E+05	1.85E+03
688.67	0.278388	1.05E+05	927.02	1.22E+05	1.08E+03
719.349	12.94173	3.87E+04	356.63	1.14E+05	1.06E+03
810.451	0.319611	3.71E+04	223.33	1.16E+05	6.96E+02
841.57	4.245423	1.84E+04	853.02	1.11E+05	5.14E+03
867.373	0.426684	4.14E+05	670.59	9.72E+04	1.57E+02
919.33	0.277585	4.10E+04	308.51	9.58E+04	7.21E+02
926.317	14.60468	2.49E+04	273.67	8.96E+04	9.84E+02
964.079	0.645647	1.34E+06	1322.81	9.06E+04	8.95E+01
1005.272	10.20668	7.03E+04	604.38	1.08E+05	9.33E+02
1112.069	1.727243	1.14E+06	1201.4	8.33E+04	8.78E+01
1212.948	13.64371	1.06E+05	347.86	7.43E+04	2.44E+02
1249.938	1.421922	1.46E+04	371.46	7.72E+04	1.97E+03
1292.778	1.62302	7.19E+03	134.98	6.78E+04	1.27E+03
1408.006	21.00494	1.41E+06	1216.44	6.69E+04	5.77E+01

APPENDIX B

NORTH ANNA TRANSLAT SIMULATIONS

TransLAT North Anna fuel radii

i	r(i)
1	0.17327368
2	0.27324389
3	0.33092169
4	0.36419888
5	0.38339815
6	0.39447517
7	0.40086605
8	0.40455327
9	0.40668061
10	0.40790797
11	0.4086161
12	0.40902466
13	0.40926037
14	0.40939637
15	0.40947483
16	0.4095201
17	0.40954622
18	0.40956129
19	0.40956998
20	0.409575

Summary of TransLAT simulation specific power and burn-up values

	Nominal	649A	649CD	649EF	649G
Scaling Factor	1	0.93269245	0.987118	0.991215	0.919663
Cycle 1 Scaled Specific Power (W/g)	48.748	45.467	48.120	48.320	44.832
Cycle 2 Scaled Specific Power (W/g)	45.912	42.822	45.320	45.509	42.223
Cycle 3 Scaled Specific Power (W/g)	11.675	10.889	11.525	11.572	10.737
Cycle 4 Scaled Specific Power (W/g)	33.305	31.064	32.876	33.013	30.630
Cycle 1 Scaled Cycle Burn-up (MWd/MTU)	22424.00	20914.70	22135.14	22227.00	20622.52
Cycle 2 Scaled Cycle Burn-up (MWd/MTU)	23966.00	22352.91	23657.28	23755.46	22040.64
Cycle 3 Scaled Cycle Burn-up (MWd/MTU)	6071.00	5662.38	5992.79	6017.67	5583.27
Cycle 4 Scaled Cycle Burn-up (MWd/MTU)	15154.00	14134.02	14958.79	15020.87	13936.57
Cycle 1 Scaled Cumulative Burn-up (MWd/MTU)	22424.00	20914.70	22135.14	22227.00	20622.52
Cycle 2 Scaled Cumulative Burn-up (MWd/MTU)	46390.00	43267.60	45792.42	45982.46	42663.16
Cycle 3 Scaled Cumulative Burn-up (MWd/MTU)	52461.00	48929.98	51785.21	52000.13	48246.43
Cycle 4 Scaled Cumulative Burn-up (MWd/MTU)	67615.00	63064.00	66744.00	67021.00	62183.00

APPENDIX C

TMI CS-134/CS-137 ACTIVITY CALCULATIONS

Summary of MCNP5 surface flux values for calculating the probability of escape

Energy (MeV)	Flux (p/cm2/s)	Fractional Standard Deviation
4.00E-01	4.74E-03	0.005
5.00E-01	7.82E-03	0.0038
6.00E-01	1.03E-02	0.0032
6.62E-01	1.15E-02	0.003
7.00E-01	1.21E-02	0.0028
8.00E-01	1.36E-02	0.0026
9.00E-01	1.48E-02	0.0025
1.00E+00	1.58E-02	0.0024
1.10E+00	1.67E-02	0.0023
1.20E+00	1.73E-02	0.0023
1.30E+00	1.79E-02	0.0022

Summary of relative attenuation to 662 keV gamma-ray for TMI Cs-134/Cs-137 activity ratios

Energy (MeV)	Relative Attenuation (no units)	Standard Deviation (no units)
4.00E-01	0.41336	0.00241
5.00E-01	0.68174	0.00330
6.00E-01	0.89525	0.00393
6.62E-01	1.00000	0.00424
7.00E-01	1.05844	0.00434
8.00E-01	1.18682	0.00471
9.00E-01	1.29429	0.00505
1.00E+00	1.37860	0.00530
1.10E+00	1.45224	0.00549
1.20E+00	1.51222	0.00572
1.30E+00	1.56297	0.00581

Summary of Relative Efficiency Calibration using Eu-152 source for TMI Cs-134/Cs-137 activity calculations

Energy (keV)	Yield (%)	Net Peak Area	Net Area Uncertainty	Relative Efficiency to 662 keV	Efficiency Uncertainty
121.7817	28.58	3.42E+04	286.49	1.20E+03	1.00E+01
244.6975	7.5834	7.98E+03	174.98	1.05E+03	2.31E+01
295.9392	26.51993	2.17E+04	183.86	8.18E+02	6.93E+00
329.425	0.860572	6.47E+02	89.7	7.52E+02	1.04E+02
416.048	2.234039	1.43E+03	85.42	6.40E+02	3.82E+01
443.965	2.821359	2.09E+03	87.07	7.41E+02	3.09E+01
488.6792	0.418921	2.28E+02	63.6	5.44E+02	1.52E+02
563.99	0.489321	2.61E+02	79.39	5.33E+02	1.62E+02
566.439	0.459325	2.64E+02	54.83	5.75E+02	1.19E+02
656.487	0.471259	1.17E+02	41.85	2.48E+02	8.88E+01
674.675	0.85658	3.20E+02	50.6	3.74E+02	5.91E+01
688.67	0.278388	8.64E+01	37.98	3.10E+02	1.36E+02
719.349	12.94173	5.13E+03	92.05	3.96E+02	7.11E+00
810.451	0.319611	6.98E+01	42.78	2.18E+02	1.34E+02
841.57	4.245423	1.41E+03	62.04	3.32E+02	1.46E+01
867.373	0.426684	1.36E+02	21.44	3.19E+02	5.02E+01
919.33	0.277585	9.09E+01	19.33	3.27E+02	6.96E+01

926.317	14.60468	4.89E+03	82.84	3.35E+02	5.67E+00
964.079	0.645647	2.84E+02	39.23	4.40E+02	6.08E+01
1005.272	10.20668	3.10E+03	58.74	3.04E+02	5.76E+00
1112.069	1.727243	5.54E+02	28.31	3.21E+02	1.64E+01
1212.948	13.64371	4.03E+03	74.07	2.95E+02	5.43E+00
1249.938	1.421922	3.85E+02	31.45	2.71E+02	2.21E+01
1292.778	1.62302	4.14E+02	27.26	2.55E+02	1.68E+01
1408.006	21.00494	5.01E+03	72.16	2.39E+02	3.44E+00

APPENDIX D

TMI TRANSLAT SIMULATIONS

TMI Cycle 9 measured boron concentrations

Cycle 9: Measured Boron Concentration	
EFPD	**Soluble Boron [ppmB]**
0	1670
74.2	1481
141.1	1342
214	1175
283.9	990
349.7	772
425	545
483.9	352
549.2	134
608	13
639.4	2

TMI Cycle 10 measured boron concentrations

Cycle 10: Measured Boron Concentration	
EFPD	**Soluble Boron [ppmB]**
0	1800
68	1649
131.8	1521
209	1322
272	1140
347.4	918
416.4	718
486.4	506
556.3	298
626.1	103
660.3	1.8

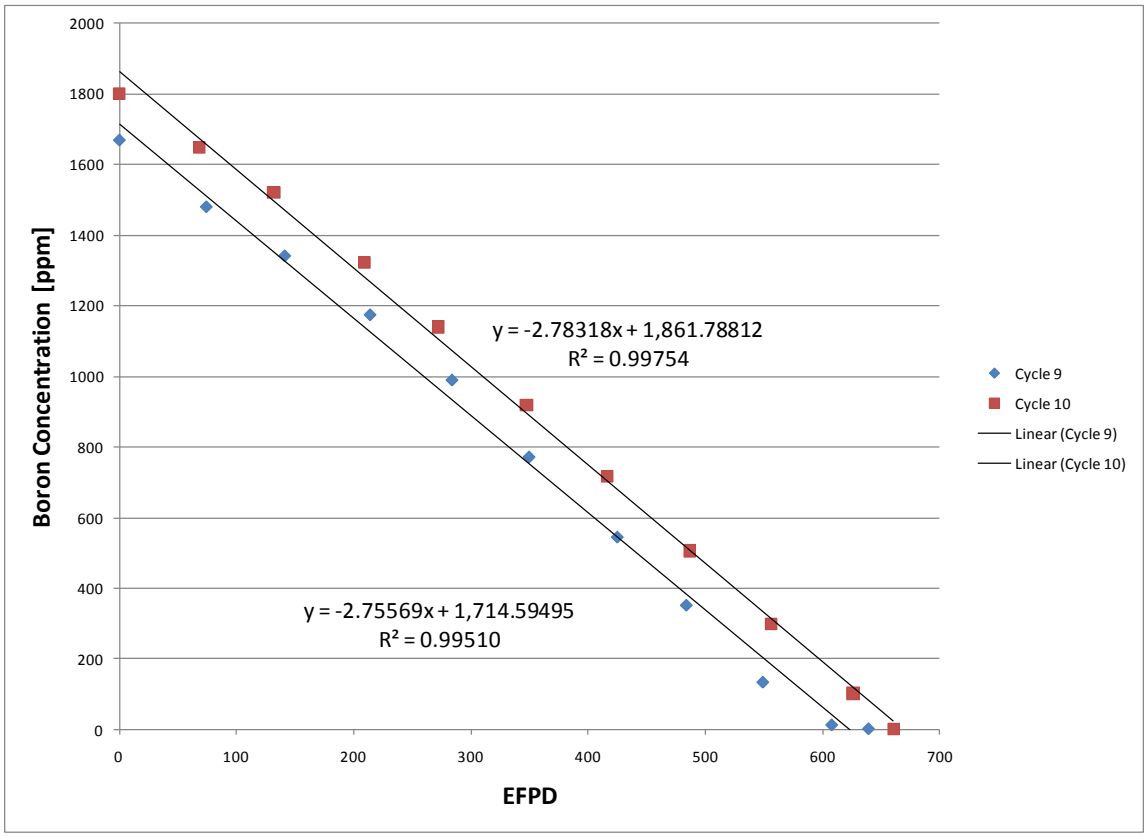

Figure 63. Boron let down curve using measured values

TransLAT TMI fuel radii

I	r(i)
1	0.198033
2	0.312288
3	0.378208
4	0.41624
5	0.438183
6	0.450843
7	0.458147
8	0.462361
9	0.464792

10	0.466195
11	0.467004
12	0.467471
13	0.46774
14	0.467896
15	0.467986
16	0.468037
17	0.468067
18	0.468084
19	0.468094
20	0.4681

Rod H6 corresponding cycle burn-up and specific power

XRF Label	XRF POS	H6 Sample POS	H6 Sample ID	H6 Cycle 9 BU (MWd/MTU)	H6 Cycle 10 BU (MWd/MTU)	H6 Cycle 9 Specific Power (W/g)	H6 Cycle 10 Specific Power (W/g)
550	330	387.35	TMI A1B	24767	45687	38.7	31.7
530	532	387.35	TMI A1B	24767	45687	38.7	31.7
586	605	746.76	TMI A2	28338	51861	44.3	35.6
661	680	746.76	TMI A2	28338	51861	44.3	35.6
730	732	770.13	TMI B3J	28338	51861	44.3	35.6
1984	2000	1946.15	TMI C2B	28155	51563	44.0	35.5
261	280	387.35	TMI A1B	24767	45687	38.7	31.7
411	430	387.35	TMI A1B	24767	45687	38.7	31.7

TMI calculated specific power and cycle burn-up

	261 mm	411 mm	530 mm	550 mm	586 mm	661 mm	730 mm	1984 mm
Scaling Factor	0.584391	0.934045	1.105273	0.731973	0.923716	1.067668	1.096337	1.148288
Cycle 1 Scaled Specific Power (W/g)	22.636	36.180	42.812	28.353	40.939	47.319	48.589	50.563
Cycle 2 Scaled Specific Power (W/g)	18.515	29.593	35.018	23.191	32.907	38.035	39.057	40.707
Cycle 1 Scaled Cycle Burn-up (MWd/MTU)	14473.62	23133.49	27374.30	18128.78	26176.27	30255.57	31067.99	32330.05
Cycle 2 Scaled Cycle Burn-up (MWd/MTU)	12225.46	19540.22	23122.32	15312.88	21728.58	25114.75	25789.13	26879.13
Cycle 1 Scaled Cumulative Burn-up (MWd/MTU)	14473.62	23133.49	27374.30	18128.78	26176.27	30255.57	31067.99	32330.05
Cycle 2 Scaled Cumulative Burn-up (MWd/MTU)	26699.08	42673.72	50496.62	33441.66	47904.84	55370.32	56857.12	59209.18

Average temperatures for TMI TransLAT simulations

XRF Label	XRF POS	H6 Sample POS	H6 Sample ID	Average Operating Temperature (K) Cycle 9	Average Operating Temperature (K) Cycle 10
550	330	387.35	TMI A1B	930.4	794.6
530	532	387.35	TMI A1B	930.4	794.6
586	605	746.76	TMI A2	970.9	818.5
661	680	746.76	TMI A2	970.9	818.5
730	732	770.13	TMI B3J	970.9	818.5
1984	2000	1946.15	TMI C2B	976.7	826.8
261	280	387.35	TMI A1B	930.4	794.6
411	430	387.35	TMI A1B	930.4	794.6

VITA

Name:	Alissa Sarah Stafford
Address:	c/o Dr. William Charlton 129 Zachry Building TAMU Department of Nuclear Engineering Texas A&M University College Station, TX 77843-3133
Email Address:	alissass@neo.tamu.edu
Education:	B.S., Nuclear Engineering, Texas A&M University, 2007 M.S., Nuclear Engineering, Texas A&M University, 2010